Transient kinetics for methane production pathways identification over Fischer-Tropsch catalysts

Davide Lorito

N°d'ordre NNT : 2017LYSE1305

THESE de DOCTORAT DE L'UNIVERSITE DE LYON
opérée au sein de
l'Université Claude Bernard Lyon 1

Ecole Doctorale N° 206
Ecole Doctorale de Chimie de Lyon

Spécialité de doctorat :
Discipline : Chimie

Soutenue publiquement le 14/12/2017, par :
Davide LORITO

Cinétique transitoire pour l'identification des voies de production de méthane sur des catalyseurs Fischer-Tropsch

---

Devant le jury composé de :

Julcour, Carine	Directrice de recherche CNRS, INP Toulouse	Examinateur
Beretta, Alessandra	Professeure, Politecnico di Milano	Rapporteur
Bion, Nicolas	Chargé de Recherche CNRS, Université de Poitiers	Rapporteur
Fecant, Antoine	Ingénieur de Recherche, IFPEN-Solaize	Examinateur
Schuurman, Yves	Directeur de recherche CNRS, IRCELYON	Directeur de thèse
Fongarland, Pascal	Professeur, Université Lyon 1, LGPC	Co-directeur de thèse

UNIVERSITE CLAUDE BERNARD - LYON 1

Président de l'Université	**M. le Professeur Frédéric FLEURY**
Président du Conseil Académique	M. le Professeur Hamda BEN HADID
Vice-président du Conseil d'Administration	M. le Professeur Didier REVEL
Vice-président du Conseil Formation et Vie Universitaire	M. le Professeur Philippe CHEVALIER
Vice-président de la Commission Recherche	M. Fabrice VALLÉE
Directrice Générale des Services	Mme Dominique MARCHAND

COMPOSANTES SANTE

Faculté de Médecine Lyon Est – Claude Bernard	Directeur : M. le Professeur G.RODE
Faculté de Médecine et de Maïeutique Lyon Sud – Charles Mérieux	Directeur : Mme la Professeure C. BURILLON
Faculté d'Odontologie	Directeur : M. le Professeur D. BOURGEOIS
Institut des Sciences Pharmaceutiques et Biologiques	Directeur : Mme la Professeure C. VINCIGUERRA
Institut des Sciences et Techniques de la Réadaptation	Directeur : M. X. PERROT
Département de formation et Centre de Recherche en Biologie Humaine	Directeur : Mme la Professeure A-M. SCHOTT

COMPOSANTES ET DEPARTEMENTS DE SCIENCES ET TECHNOLOGIE

Faculté des Sciences et Technologies	Directeur : M. F. DE MARCHI
Département Biologie	Directeur : M. le Professeur F. THEVENARD
Département Chimie Biochimie	Directeur : Mme C. FELIX
Département GEP	Directeur : M. Hassan HAMMOURI
Département Informatique	Directeur : M. le Professeur S. AKKOUCHE
Département Mathématiques	Directeur : M. le Professeur G. TOMANOV
Département Mécanique	Directeur : M. le Professeur H. BEN HADID
Département Physique	Directeur : M. le Professeur J-C PLENET
UFR Sciences et Techniques des Activités Physiques et Sportives	Directeur : M. Y.VANPOULLE
Observatoire des Sciences de l'Univers de Lyon	Directeur : M. B. GUIDERDONI
Polytech Lyon	Directeur : M. le Professeur E.PERRIN
Ecole Supérieure de Chimie Physique Electronique	Directeur : M. G. PIGNAULT
Institut Universitaire de Technologie de Lyon 1	Directeur : M. le Professeur C. VITON
Ecole Supérieure du Professorat et de l'Education	Directeur : M. le Professeur A. MOUGNIOTTE
Institut de Science Financière et d'Assurances	Directeur : M. N. LEBOISNE

RÉSUMÉ

Cinétique transitoire pour l'identification des voies de production de méthane sur des catalyseurs Fischer-Tropsch23

La synthèse Fischer-Tropsch (FT) permet de convertir un mélange d'hydrogène et de monoxyde de carbone (gaz de synthèse) en hydrocarbures avec une distribution large de longueur de chaine. Le gaz de synthèse peut être produit à partir de différentes ressources comme le gaz naturel, le charbon et la biomasse. Afin de diversifier les sources d'énergie, la synthèse FT peut apporter une contribution pour la production de carburants liquides. Néanmoins, la formation de méthane pendant la réaction affecte la faisabilité économique du procédé. Cette étude a pour but de comprendre le mécanisme de formation du méthane sur des catalyseurs de FT. Pour atteindre cet objectif, une étude cinétique en régime transitoire couplée à la technique « SSITKA » a été mise en œuvre sur différents catalyseurs nickel et cobalt. Les données expérimentales sont ensuite utilisées pour alimenter un modèle microcinétique. En utilisant cette méthodologie, nous avons montré que deux intermédiaires distincts de surface conduisaient à la production de méthane. Le modèle microcinétique consiste en deux voies de production de méthane, l'une par dissociation directe de CO, l'autre par décomposition de CO assistée par hydrogène. Nous proposons que les proportions relatives de ces deux intermédiaires dépendent de la structure des particules métalliques, notamment la distribution des sites en sur les terrasses et les coins.

ABSTRACT

Transient kinetics for methane production pathways identification over Fischer-Tropsch catalysts

The Fischer-Tropsch synthesis (FTS) converts a mixture of hydrogen and carbon monoxide (syngas) selectively into hydrocarbons with a large chain length distribution. Syngas can be produce from different resources such as natural gas, coal and biomass. In the light of energy resource diversification, FTS can make a contribution to the production of liquid fuels. However, methane formation as byproduct has a large impact on the process economic feasibility. This study aims at the understanding of the methane formation over syngas conversion catalysts, such as nickel and cobalt. To this purpose, Steady-State Isotopic Transient Kinetic Analysis (SSITKA) and step-transient experiments over different nickel and cobalt samples have been carried out and the data have been used to develop a microkinetic model describing methane formation. By using these methodologies, it was found that the CO conversion to methane proceeds through two different surface intermediate species. The microkinetic model is developed on the hypothesis of two reacting paths leading to methane: the unassisted CO dissociation and the H-assisted CO decomposition. It is proposed that these two reacting intermediates are related to the structure of the catalyst particle, specifically to the distribution of the catalyst surface sites on terraces and steps.

Summary

Index of Figures

Index of Tables

Chapter 1

Introduction

This chapter describes the principal use of syngas, in the context of gas to liquid technology.

It will emphasize the necessity to find an alternative energy source for hydrocarbon fuels.

The aim and the outline of this thesis work is presented at the end of the chapter.

The endeavor to find an alternative to crude oil for the production of chemical raw materials and motor fuels syngas chemistry ($CO + H_2$) has been an interesting subject of development and research since the early 30ties. The syngas chemistry offers many routes to fuels and chemicals through (partial) hydrogenation of carbon monoxide to alkanes, alkenes and oxygen containing products [1]. The hydrogenation of carbon monoxide is best known as the FISCHER-TROPSCH Synthesis (FTS), which involves a stepwise hydrocarbon chain growth described by the SCHULZ-FLORY distribution [2, 3]. Even if the direct production of gasoline and diesel oil via FTS is not economic today, because the direct refining of crude oil is much cheaper, there are several FT plants around the world. Much work had been carried out either to increase the amount of C_2-C_4 olefins which are an important feedstock for the chemical industries or the selectivities towards C_{18+} alkanes (high-boiling waxy hydrocarbons) which may be converted by hydrocracking to any desired alkane fraction[4,5].

The largest FTS production facilities are based on natural gas. Table 1 gives an overview of production facilities which were, are or will, in the near future, become operational together with the feedstock used, the location and the operating companies. From 1951 to 1957, a natural gas based production facility was operational in Brownsville (Texas) with an annual production capacity of 360 kt y^{-1}. It was based on the Hydrocol Process[6] developed by Hydrocarbon Research Inc. A Fixed Fluidized Bed Reactor (FFBR) technology, was applied at High Temperature Fischer-Tropsch (HTFT) conditions, employing a Fe catalyst. This production facility ceased operation due to the low crude oil prices caused by the discovery of large oil reserves in the 1950's in the Middle East.

Table 1: Fischer-Tropsch Synthesis (FTS) production facilities [7-9].

Year	Location	Production capacity	company	Catalyst
Gas based FTS production facilities				
1950	Brownsville	360 kt y^{-1}	Carthage Hydrocol Company	Fe
1992	South Africa	1000 kt y^{-1}	PetroSA	Fe
1993	Malaysia	500 kt y^{-1}	Shell	Co
2007	Qatar	1800 kt y^{-1}	Qatar Petroleum and Sasol	Co
2011	Qatar	7000 kt y^{-1}	Shell	Co
2014	Escravos	1800 kt y^{-1}	Chevron Nigeria	Co
Coal based FTS production facilities				
1938	Germany	660 kt y^{-1}	Ruhrchemie AG	Co
1955	South Africa	Combined: 6000 kt y^{-1}	Sasol	Fe
1980	South Africa			Fe
1982	South Africa			Fe

In 1992, a GtL FTS production facility was commissioned by the South African Government at Mossel Bay[9]. By 2002, PetroSA took over the operation of this production facility. It has 16 Circulating Fluidized Bed reactors (CFBRs), a reactor technology licensed by Sasol. The total production capacity amounts to 1000 kt y^{-1}. The natural gas is first reformed into CO, CO_2, H_2 and H_2O and subsequently converted into a synthetic crude. The CFBRs are operated at HTFT conditions.

Shell has two GtL production facilities, i.e., one in Malaysia [10, 11] and one in Qatar [13]. Both facilities are based on the proprietary Shell Middle Distillate Synthesis (SMDS) [12, 13] process filed in over 3500 patents. The syngas is produced by natural gas partial oxidation. Subsequently, impurities are removed from the syngas. The purified syngas is then reacted over Co catalysts in Multi-Tubular Trickle Bed Reactors (MTTBRs), at LTFT conditions. The resulting synthetic crude is further processed into marketable products such as high quality diesel fuel, kerosene and waxes by cracking and isomerization operations. The plant in Malaysia has a production capacity of 500 kt y^{-1} while the production facility in Qatar, Pearl, has an annual production capacity of 7000 kt.

Another large-scale GTL production facility located in Qatar is the Oryx GtL [14] which is a joint venture between Qatar Petroleum and Sasol. The syngas is produced by natural gas reforming based on licensed technology of Haldor Topsøe while the FTS is performed in a slurry phase reactor, for which the technology was licensed by Sasol. The resulting synthetic crude is processed by isocracking operations based on technology of Chevron. The total production capacity amounts to 1800 kt y^{-1}. In Escravos (Nigeria), a FTS production facility is commissioned since 2014 based on the technology of Sasol and Chevron. Other projects based on the Sasol Slurry Phase Distillate (SPD) process are announced in Uzbekistan and North America. In North America, the shale gas revolution has increased the price difference between gas and crude oil opening up new opportunities for GtL production facilities.

Next to large scale production facilities, which aim at producing 7000 kt y^{-1} of FTS liquids, technologies have also been developed recently which aim at the production of FTS liquids with a production capacity below 25 kt y^{-1}, e.g., INERATEC ReThink GtL process [15]. This has become possible by the development of microreactors.

1.1 Gas-to-liquid technology

The Fischer-Tropsch process is a key intermediate step in the process called "Gas-to-liquid technology". The aim of this process is to produce liquid hydrocarbons starting from a gaseous feed. Natural gas is a cleaner feedstock then coal and crude oil. Starting from natural gas, the Fischer-Tropsch synthesis produces a clean hydrocarbon product. It is free of sulphur and nitrogen compounds, aromatics, and heavy metals. Crude oil and coal contain large quantities of sulphur and nitrogen compounds and heavy metals, which are removed by processes such as hydro-desulphurisation and hydro-denitriphication. The sulphur is recovered via the Claus process to meet environmental constraints on emissions. Due to tightening environmental legislation, these processes will become even more important in the near future.

In the gas-to-liquid technology, natural gas is converted into a liquid product containing hydrocarbons and oxygenates.
The gas-to-hydrocarbons technology consists of the following process steps:

- Synthesis gas manufacturing
- Fischer-Tropsch synthesis

• Product upgrading

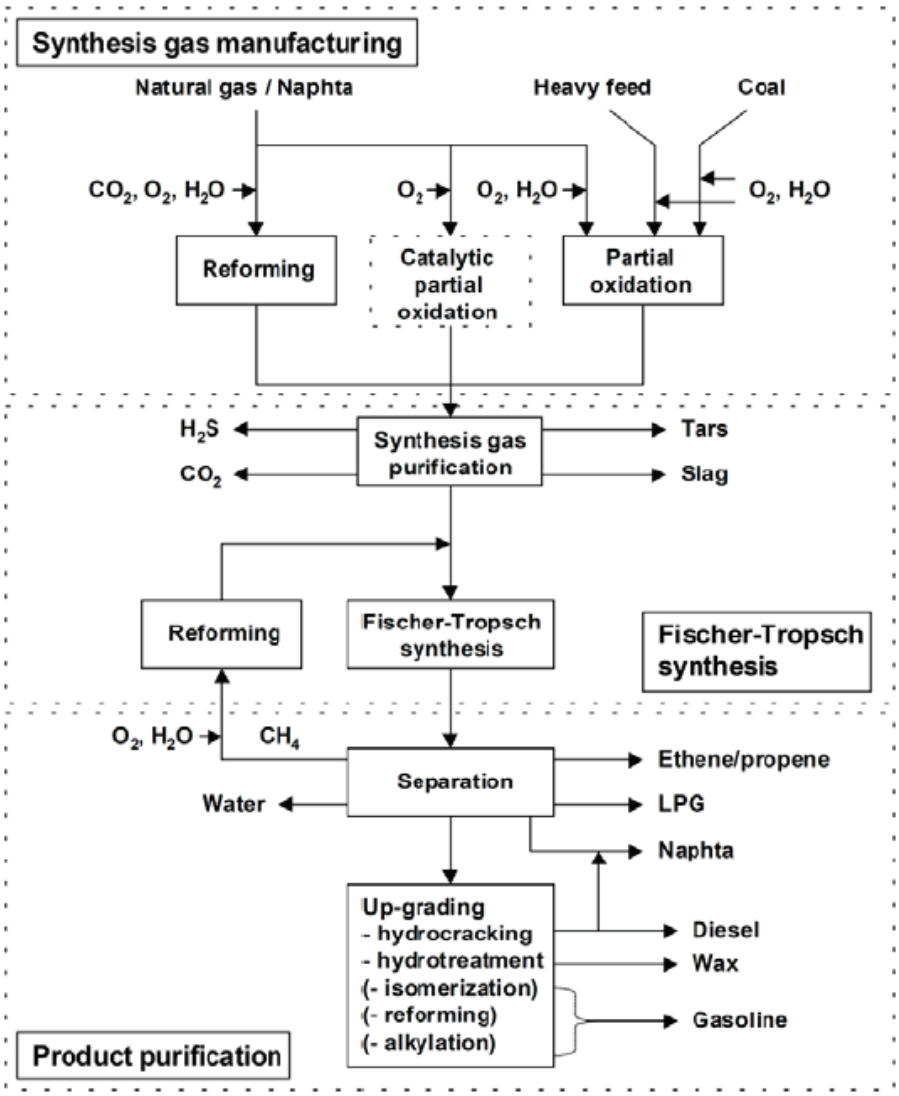

Figure 1: Schematic representation of a gas-to-hydrocarbons technology [8, 16]

1.1.1 Synthesis gas manufacturing

The common feedstocks for this first step are natural gas (80%) on the one hand, and naphtha and coal (20%) on the other hand. There are three basic methods of converting a feed stream into synthesis gas: reforming, partial oxidation, and catalytic partial oxidation. In all cases, a near-to-equilibrium synthesis gas mixture is obtained of which the H_2/CO ratio can be adjusted via the water-gas shift reaction (Eq. 1):

$$CO + H_2O \rightleftarrows CO_2 + H_2 \qquad \Delta H° = -42\ \frac{kj}{mol}$$

Eq. 1

In the reforming process, the feed stream is passed over a Ni-based catalyst together with H_2O and/or CO_2 at high temperatures (800-900°C) and medium pressures (10-30 bar). Steam reforming and oxy-steam reforming (or so-called autothermal reforming) hold the leading positions among the commercial processes of synthesis gas production in the synthesis of methanol and ammonia. Steam reforming of methane is highly endothermic (Eq. 2):

$$CH_4 + H_2O \rightarrow CO + 3\,H_2 \qquad \Delta H° = +226\ \frac{kj}{mol}$$

Eq. 2

Large furnaces are used, inflicting large capital investments. The endothermicity of the steam reforming process is compensated by the addition of oxygen in the autothermal reforming process.

The synthesis gas from industrial steam reformers has a high H_2/CO ratio (H_2/CO=3-7 and CO/CO_2=0.3-1.5).

In partial oxidation, the feed stream is mixed with oxygen and steam then is sent to a high temperature flame (1300-1500°C). The feed is partially combusted followed by endothermic reforming steps and the water-gas shift reaction. This process is particularly suitable for heavy feeds, such as the residues from vacuum distillation and catalyst cracking (FCC). In the partial oxidation of coal, better known as gasification, an oxygen-water mixture is contacted with a fixed, entrained, or fluidized bed of fine coal particles. The synthesis gas from industrial partial oxidation has a low H_2/CO ratio (H_2/CO=0.5-2 and CO/CO_2=5-15).

In the catalytic partial oxidation a catalyst takes over the function of the flame in the partial oxidation. The advantages of the catalytic partial oxidation of methane over steam reforming of methane are the low exothermicity of the process and the high reaction rates, leading to significant smaller reactors (Eq. 3):

$$CH_4 + \frac{1}{2}O_2 \rightarrow CO + 2\,H_2 \qquad \Delta H° = -22\ \frac{kj}{mol}$$

Eq. 3

Usually, a combination of synthesis gas production processes is used to obtain synthesis gas with a stoichiometric ratio of hydrogen and carbon monoxide.

Synthesis gas produced in modern coal gasifiers (Shell/Koppers or Texaco gasifiers) and from heavy oil residues has a high CO content in comparison to synthesis gas from natural gas. If synthesis gas with a H_2/CO ratio below 2 is used, the composition is not stoichiometric for the Fischer-Tropsch reactions. Then the water gas shift reaction is important to change the H_2/CO ratio to 2. Table 2 shows the application ranges for iron (high WGS-activity) and cobalt catalysts (no WGS activity) [17]. Inexpensive iron catalysts in comparison to cobalt can directly convert low H_2/CO ratio synthesis gas without an external shift reaction [17–19].

Table 2: Synthesis gas compositions.

Feedstock	Process	Component (vol%)			
		H_2	CO	CO_2	Other
Natural gas, steam	SR[1]	73.8	15.5	6.6	4.1
Natural gas, steam, CO_2	CO_2 - SR[2]	52.3	26.1	8.5	13.1
Natural gas, O_2, steam, CO_2	ATR[2]	60.2	30.2	7.5	2.0
Coal/heavy oil, steam	Gasification[1]	67.8	28.7	2.9	0.6
Coal, steam, oxygen	Texaco gasifier[1]	35.1	51.8	10.6	2.5
Coal, steam, oxygen	Shell/Koppers gasifier[1]	30.1	66.1	2.5	1.3
Coal, steam, oxygen	Lurgi gasifier[3]	39.1	18.9	29.7	12.3

SR= steam reforming, CPO= catalytic partial oxidation, ATR= autothermal reforming

New ceramic membranes might become interesting for significant cost reduction of synthesis gas production by 30-50 % [20]. Reduction of the synthesis gas costs could also be accomplished by a decrease of steam/carbon and oxygen/carbon ratios in the feedstock. Basini and

Piovesan[21] compared economical evaluations of steam-CO_2 reforming, autothermal reforming, and combined reforming processes.

They concluded that combined reforming has the lowest production and investment costs at a H_2/CO ratio of 2.

Although the capital costs predominate, the cost price of natural gas is also an important factor in the overall process economics of GTL Fischer-Tropsch plants. Remote gas fields or natural gas associated with crude oil production has a low cost or a negative value as an undesired by-product. Reduction of flaring of associated natural gas and the unfavorable economics of gas reinjection make the Fischer-Tropsch process economically viable. FT derived fuels are easily transported in standard vessels or pipelines relative to natural gas and LNG.

1.1.2 Fischer-Tropsch synthesis (FTS)

The Fischer-Tropsch reaction is the chemical heart in the gas-to-liquid technology and this process has a lively history of more than 70 years. The highly exothermic reaction converts synthesis gas into a large range of linear hydrocarbons, schematically represented as (Eq. 4):

$$nCO + 2n\,H_2 \rightarrow -(CH_2)_n - + nH_2O \qquad \Delta H° = -165\ \frac{kj}{mol}$$

Eq. 4

The industrial reaction conditions are 200-300°C and 25-40 bar.

The exothermic FTS is heterogeneously catalyzed by Group VIII metal. Within this group, the specific activity is decreasing in the following order:

Ru > Co > Fe >Ni> Rh > Pd > Pt > Ir

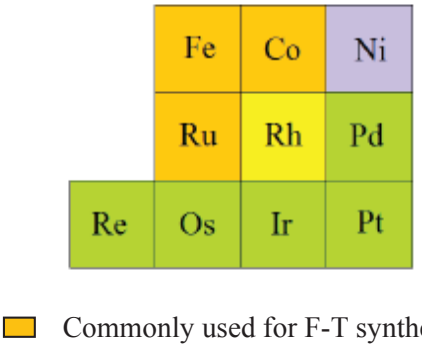

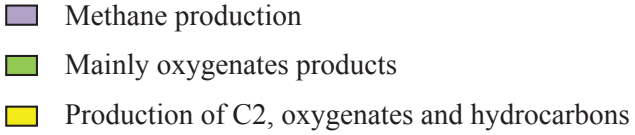

Figure 2: CO hydrogenation over group VIII metals

Although all group VIII metals display some activity in the C-C coupling reaction during the hydrogenation of CO, the most active metals for the Fischer-Tropsch synthesis are ruthenium, iron, cobalt[1]. This is related to the capacity of the metals to dissociate CO. Going to the left and up in the group VIII metals, the CO dissociation intensifies and excessive carbonization of the metal is risked. Going to the right and down, CO dissociation becomes more difficult and the hydrogenation towards alcohols dominates.

Iron, cobalt, and ruthenium display intermediate behavior and are excellent Fischer-Tropsch catalysts. Also the nickel is a Fischer-Tropsch catalyst but the major disadvantage of nickel is that it readily forms volatile metal-carbonyls, limiting the reaction pressure and thus the Fischer-Tropsch productivity. At industrial conditions, nickel has selectivity to methane higher than 80%.

Iron catalysts for the Fischer-Tropsch synthesis generally consist of precipitated iron, which is promoted with potassium and copper to obtain a high activity and selectivity, and with Al_2O_3 and SiO_2 added as structural stabilizers. Typically for these relatively cheap Fe-based catalysts is that the active phase for Fischer-Tropsch appears to be a Fe-carbide. Also, Fe-oxides are formed, which are active for the water-gas shift reaction. This high water-gas shift activity causes these catalysts to be flexible towards the H_2/CO feed ratio of the synthesis gas. This allows the utilization of a large variety of feedstocks, while every syngas manufacturing technology can be applied. However, the water-gas-shift activity of the catalyst also results in a low carbon efficiency of the gas-to-liquid process. At high temperature (340°C), Fe-based catalysts are selective for light olefins with a low selectivity towards methane. The application of Fe-based catalysts in the production of heavy wax is limited. This is mainly due to its tendency to form elemental carbon, causing deactivation of the catalyst. Moreover, water, which is produced in large quantities as side product, has an inhibiting effect on the activity, resulting in low conversions per pass. The latter effect results in large recycle streams after water removal.

Cobalt catalysts are usually supported on metal oxides, due to the higher cobalt price and better catalyst stability. The active phase is metallic cobalt; the tendency of cobalt to form carbides at 200-300°C and 25-40 bar is low. The water-gas shift activity of Co-based catalysts is low and water is the main oxygen containing reaction product. The cobalt is generally poorly dispersed on metal oxide supports and Ru, Re, or Pt promoters are applied to prevent catalyst deactivation by carbon formation or oxidation. Compared to Fe-based catalysts, olefins tend to re-enter the chain growth process by re-adsorption on Co-based catalysts, increasing the selectivity towards heavy hydrocarbons. Co-based catalysts are very suitable for wax formation in slurry bubble columns and can operate at high conversions per pass.

Ruthenium catalysts are the most active Fischer-Tropsch catalysts. A high molecular weight wax is obtained at reaction temperatures as low as 150°C. The catalyst is active in its metallic form and no promoters are required to stabilize its activity. However, the high price of ruthenium excludes its application on industrial scale and the use of Ru-based catalysts for the Fischer-Tropsch synthesis is limited to academic studies.

1.1.3 Product upgrading

The hydrocarbon product mixture leaving the Fischer-Tropsch reactor is frequently referred to as synthetic crude oil. This already illustrates that the standard product upgrading techniques that are used in refineries are also suitable for the upgrading of the Fischer-Tropsch wax. Fischer-Tropsch wax consists mainly of linear hydrocarbon chains over a large boiling range and has a zero-level of sulphur or nitrogen contaminants and aromatics.

The Fischer-Tropsch process directly produces high quality waxes suitable for food applications and cosmetics and medicines. However, this is a limited market, which is easily saturated.

The C_9-C_{15} olefins are very suitable for the production of biodegradable detergents, whereas the paraffins are excellent lubricants. High selectivities towards fuels are obtained by hydrocracking the wax. Hydrocracking is a selective process, which converts heavy hydrocarbons into the C_4-C_{12} range with low selectivities to C_1-C_3. This directly produces a high quality gasoil (high cetane index, low sulfur content, low aromatics) and kerosene (high paraffin content), which are very suitable as blending components to upgrade lower quality stock.

The linearity of the Fischer-Tropsch naphtha is a drawback for gasoline production. Processes such as isomerization, catalytic reforming, alkylation, and oligomerization improve the octane number of the hydrocracked wax. The naphtha is therefore better used as feedstock for the petrochemical industry. Its high paraffin content makes the naphtha an ideal cracker feedstock for ethylene and propylene production.

1.2 Fischer-Tropsch chemistry

1.2.1 General reaction pathways

The Fischer-Tropsch synthesis can be considered as a heterogeneously catalyzed and non-selective polymerization reaction that converts the syngas into a mixture of mostly linear alkanes, alkenes, alcohols, aldehydes, ketones, carboxylic acids and water. The monomeric species contain only one carbon atom and the growing chains are linked on the solid active phase. The catalyst and the operating conditions can orientate the syncrude quality by favoring chain growth and moieties. The overall FTS reactions can be denoted as follows:

Alkanes	$nCO + (2n + 1)H_2 \rightarrow H(CH_2)nH + n\,H_2O$	$\Delta H = -165\ kJ.mol^{-1}$
Methanation	$CO + 3H_2 \rightarrow CH_4 + H_2O$ $2CO + 2H_2 \rightarrow CH_4 + CO_2$	$\Delta H_{600K} = -241.8\ kJ\cdot mol^{-1}$ $\Delta H_{600K} = -254.1\ kJ\cdot mol^{-1}$
Alkenes	$nCO + 2nH_2 \rightarrow (CH_2)n + nH_2O$	$\Delta H = -211\ kJ\cdot mol^{-1}$ (for C_2H_4)
Alcohols	$nCO + 2nH_2 \rightarrow H(CH_2)nOH + (n-1)H_2O$	
Carbonyls	$nCO + (2n-1)H_2 \rightarrow (CH_2)nO + (n-1)H_2O$	
Carboxylic acids	$nCO + (2n-2)H_2 \rightarrow (CH_2)nO_2 + (n-2)H_2O$, $n>1$	
Water gas shift	$CO + H_2O \rightarrow CO_2 + H_2$	$\Delta H_{600k} = -39\ kJ\cdot mol^{-1}$
Boudouard's reaction	$2CO \rightarrow C + CO_2$	$\Delta H_{600k} = -134.0\ kJ\cdot mol^{-1}$

1.2.2 Product Distribution

The FTS is a stepwise polymerization process. Therefore, the product distribution is kinetically controlled by two competitive reactions:

• The propagation allowing the chain growth of $*C_nH_{2n}$ by addition of a monomer $*CH_2$ with the rate r_p.

• The termination reactions leading to the final product with the rate r_t .

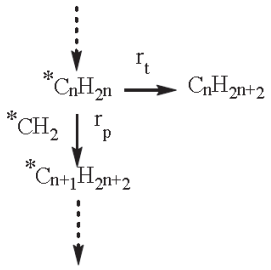

As a consequence, the propagation growth probability for a given chain length n is defined as:

$$\alpha = \frac{r_{p,n}}{r_{p,n} + r_{t,n}}$$

For high chain length (approx. n>10-15), it can be assumed that propagation and termination rate become independent of the length. As a result, the mass fraction of every chain constitutive of distribution is described by the Anderson-Schulz-Flory (ASF) equation:

$$\frac{W}{n} = (ln^2\alpha) \cdot n \cdot \alpha^n$$

This equation is routinely used to determine the experimental growth probability α. The ASF plot of ln(Wn/n) vs. n. is used to determine the slope equal to ln(α) at high n values by least square adjustment.

$$log\frac{W}{n} = log(ln^2\alpha) + n \cdot \log\alpha$$

Note in Figure 3 that for high values of α, the product selectivity is strongly shifted toward the long chain length. More particularly, for α>0.9, a small increase of α will have a deep impact on long chain production and diesel yield. Consequently, α is a key parameter for optimization of the final diesel and jet fuel yield.

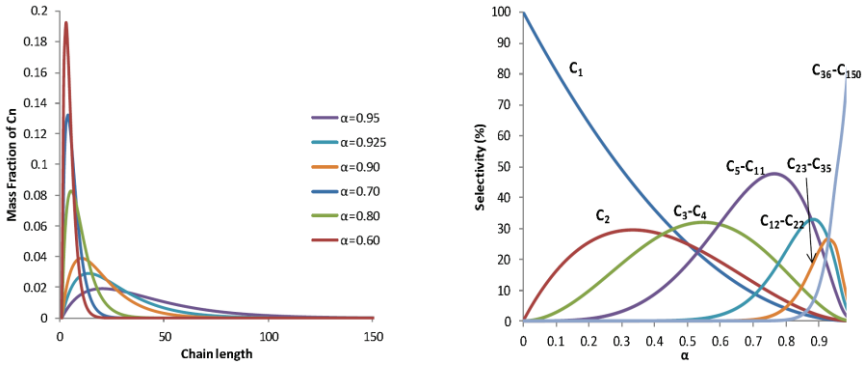

Figure 3: ASF distribution for various α growth probabilities (On the left). Selectivities of various product's cut vs. α (On the right).

1.2.3. Impact of FT Operating Conditions on product selectivity

General trends of the operating conditions that impacts on the selectivity are reported in Figure 4 by De Klerk[22]. An increase in temperature or H_2/CO ratios tend to favor the conversion as well as termination reactions resulting in lower α and higher methane selectivity. Whereas the H_2/CO ratio also impact the alkenes/oxygenate selectivity by increasing the surface hydrogen availability for hydrogenation, the temperature affects all underlying reaction kinetics so that all activation energies should be considered for deep understanding of the detailed moieties selectivity. The α selectivity is known to be strongly dependent from the temperature and the catalyst properties.

Selectivity parameter	Operating parameter being increased			
	Temperature	Pressure	Space velocity	H_2:CO ratio
Carbon number distribution	Lower α-value	Higher α-value	No change[a]	Lower α-value
Methane selectivity	Increases	Decreases	Decreases	Increases
Alkene selectivity	–[b]	–[b]	Increases	Decreases
Oxygenate selectivity	–[b]	Increases	Increases	Decreases
Aromatic selectivity	Increases	–[b]	Decreases	Decreases
Syngas conversion	Increases	Increases	Decreases	–[b]

[a]Some change is possible if secondary reactions like re-incorporation, hydrogenation, or cracking are significant.
[b]The direction of change depends on a more complex relationship.

Figure 4: Influence of Fischer–Tropsch operating conditions on product selectivity [22]

Since space velocity and pressure are not completely independent, their effects on selectivity are more complex to interpret. It is widely reported that the pressure affects the reactant surface coverages, steric hindrance (decreasing of branched compounds with pressure) and readsorption of alkenes. The space velocity mostly affects the conversion and the concentrations (axial gradients in fixed beds or average reactants/products concentration in slurry) within the reactor and as a consequence it also influences the probability of product reinsertion or secondary reactions.

1.3 Reaction mechanism of Fischer-Tropsch synthesis

From literature, the three major reaction mechanisms for the Fischer-Tropsch synthesis are:

1. The carbide mechanism;

2. The hydroxy-carbene mechanism;

3. The CO-insertion mechanism.

For each mechanism, several variants are reported. Because extensive reviews can be found in literature [6], only the most important aspects of the reaction mechanisms are reported here.

1.3.1. Carbide Mechanism

The carbide mechanism was first supposed by Fischer and Tropsch [2,3]. The initial step is the dissociative adsorption of carbon monoxide on the catalyst surface under formation of a carbide that consecutively reacts to a M-CH_x species. The insertion of one of two neighboring CH_x species into the metal-carbon bond of the other species leads to the formation of a higher hydrocarbon. The chain growth is interrupted by the hydrocarbon desorption. However, this reaction pathway does not explain the formation of oxygenated hydrocarbons (alcohols and aldehydes) which are byproducts of the Fisher-Tropsch synthesis. P. Biloen et al.[23] pointed out that the predominant propagation of normal, oxygen-free hydrocarbons can be described by the following reaction step:

$$M - C_m H_y + M - CH_x \rightarrow C_{m+1} H_{x+y} + 2M$$

Where x = 0-3, often x = 2 and y = 2m+1

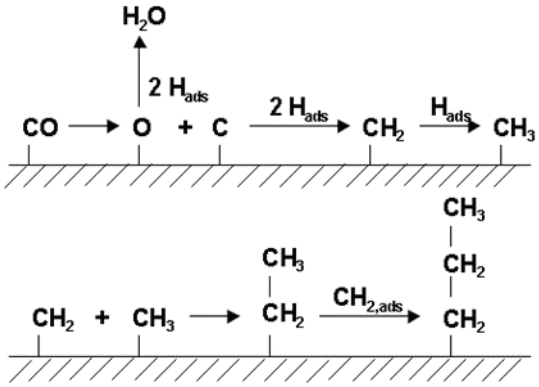

Figure 5: Schematic representation of carbide mechanism

1.3.2. Hydroxy-Carbene Mechanism (Enol mechanism)

In the hydroxycarbene mechanism, chain growth proceeds via condensation reaction of two hydroxycarbene species $CHOH_{ads}$ with the elimination of water. The mechanism is shown in Figure 6 in which the hydroxycarbene species is the key intermediate. They are formed via the partial hydrogenation of adsorbed CO_{ads}. The mechanism readily explains the formation of alcohols via hydrogenation, aldehydes via desorption, and hydrocarbons via the hydrogen assisted elimination of the -OH group.

The basis for the mechanism lies in the observation that co-feeding of alcohols during the Fischer-Tropsch reaction leads to the participation of these alcohols in chain growth. However, adsorption of co-fed alcohols and the participation of the resulting intermediates in chain growth processes do not make evident that the growing chain on the catalyst surface is an O-containing species. Moreover, the C-C bond formation between two electrophilic hydroxycarbene species is not obvious.

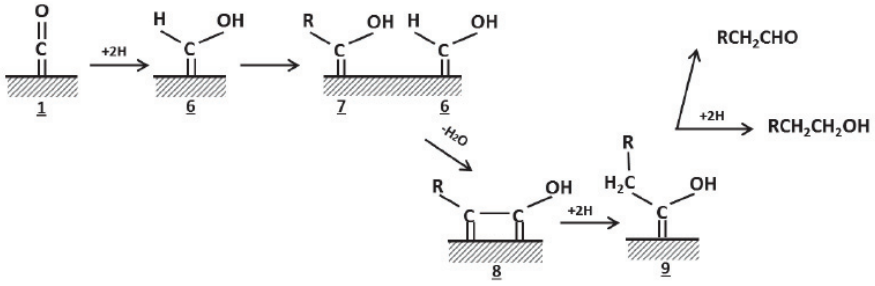

Figure 6: Schematic representation of enol mechanism

1.3.3. CO Insertion Mechanism

In the CO-insertion mechanism, chain growth proceeds via the insertion of a carbonyl intermediate (CO_{ads}) into the metal-alkyl bond. For the C-C coupling reaction to take place, the resulting species is first hydrogenated to an alkyl chain. This mechanism explains the formation of alcohols, aldehydes, and hydrocarbons. It is shown in Figure 7 where the carbonyl species is the key intermediate. Pichler and Schulz first proposed the CO-insertion mechanism in 1970.

It is based on the work on organometallic complexes. Assuming that the active surface during heterogeneous catalysis should be considered to consist of individual active sites possessing a specific coordination, organometallic complexes represent chain growth sites during the Fischer- Tropsch synthesis. Indeed, CO-insertion into a metal-alkyl complex is frequently observed with Fe complexes and Ru-complexes [24]. However, methylene insertion according to the carbene mechanism is also reported for organometallic systems [3]. There is still no exclusive experimental evidence for the CO-insertion as the key mechanism for the hydrocarbon formation during the Fischer-Tropsch synthesis.

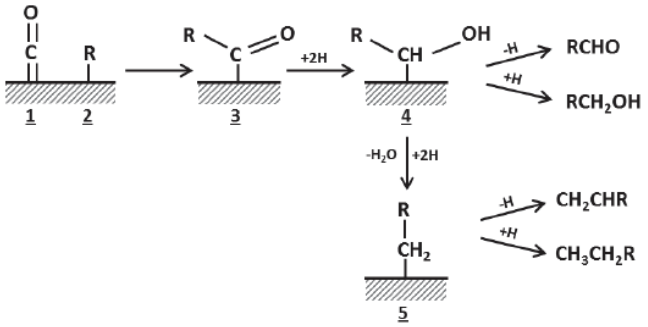

Figure 7: Schematic representation of CO insertion mechanism

1.4 Kinetics of the Fischer-Tropsch reaction over nickel and cobalt catalysts

1.4.1 CO adsorption

The CO adsorption through the carbon atom on Fischer-Tropsch catalysts surface is described by two different adsorbed species:

1. The linearly bounded CO which is linked to one cobalt/nickel atom with a characteristic IR absorption band in the 2025-2054 cm^{-1} region [25,26].
2. The CO bonded to two or more cobalt/nickel atoms which is denoted as the "bridge" adsorbed CO (IR: 1901-1855 cm^{-1}, 1927 cm^{-1} on nickel).

Several techniques have been applied for the estimation of the heat of adsorption of the CO on cobalt. Recently, Patanou and Blekkan [29] performed some calorimetric experiments and compared their results by reviewing the previous work based on calorimetry, TPD (Temperature Programmed Desorption) and ab initio calculation.

The main limitation of calorimetric and TPR measurements is that these techniques do not differentiate the adsorption on different sites (support, cobalt oxide, metal cobalt).

Patanou and Blekkan report that Calorimetry and TPR only assume the bridged adsorption of CO whereas Couble and Bianchi [25] showed with IR experiments that most of the CO are linearly adsorbed at RT with a small part of bridged CO (approx. 5%). Each type of adsorbed CO is distinguishable with its own IR adsorption band (2025-2054; 1885 cm^{-1}). Monitoring of the IR absorption as a function of temperature can be used to estimate quantitatively the heat of adsorption independently from each other for both types of adsorbed CO*. The other strength of this method is that it is operated operando, taking into account the surface reconstruction of the fresh Co catalyst.

Table 3: Heat of adsorption for CO on cobalt based catalysts

	Heat of adsorption for CO (kJ/mol)	
	At low coverage (<5%)	Intermediate coverage > 5%
Couble and Bianchi (AEIR Method)	165	93
Patanou and Blekkan Calorimetry	121-141	105-115

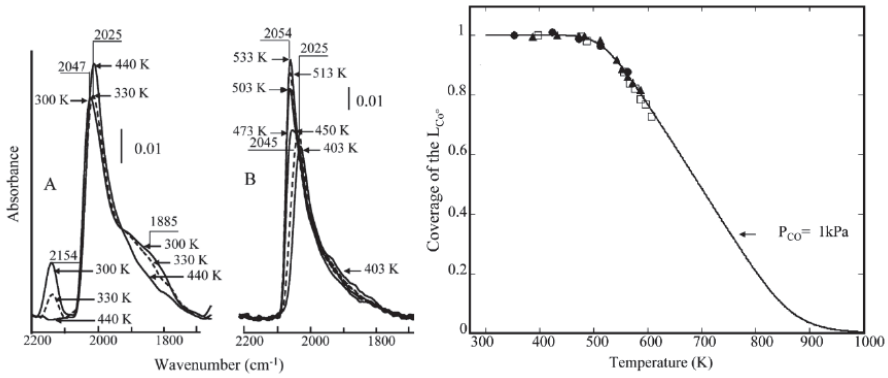

Figure 8: On the left : Evolution of the IR bands of the adsorbed CO species on the aged 10% Co/Al_2O_3 solid during the increase in the adsorption temperature Ta in the range 300–573 K with 1% CO/He (Adapted from 25). On the right: experimental evolutions of the coverage (LCo◦C) of the linear CO species during the cooling stage after a pretreatment followed by the adsorption at 613 K; theoretical curves according to the Temkin adsorption model using E LCo◦C (0)=165 kJ/mol and E LCo◦C (1)=93 kJ/mol and PCO = 1 kPa (see 25 for more details)

Van Helden et al.[28] used CO coverage dependent heat of adsorption over cobalt in the range of 115- 25 kJ/mol, which corresponded well with experimental TPD data.

Finally, it is here emphasized that this analysis only takes into account one type of adsorption site on cobalt.

Recently Weststrate et al.[30] by means of high-resolution photoemission measurements and infrared spectroscopy over Co(0001) single crystal surface showed the presence of several different adsorbed CO related to the adsorption site.

By using measurements of the equilibrium CO concentration as a function of temperature and CO pressure in the 10^{-7}–10^{-3} mbar pressure regime were used to construct a phase diagram for CO on Co(0001),

reproduced as Figure 9. Extrapolation of this low pressure information into the 1–10 bar pressure regime predicts a θ_{CO} of 0.5 ML at typical LT-FTS temperature (470–500 K) and pressures. They further reported heat of adsorption of around 120–130 kJ mol^{-1} for θ_{CO} <0.3 ML and 90 kJ mol^{-1} θ_{CO} >0.3 ML.

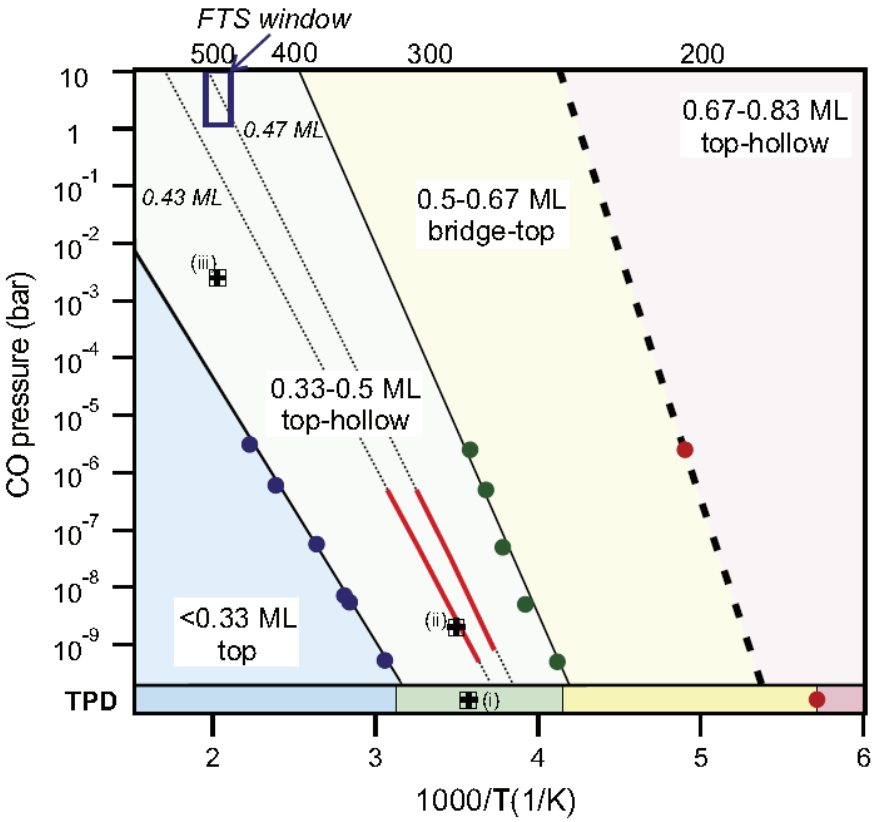

Figure 9: Phase diagram for CO on Co(0001), derived from experimental data with the measured data points indicated with a marker. Top part shows the prediction at equilibrium conditions, whereas the lower part pots the findings from a TPD experiment, that is, for irreversible desorption into a vacuum.[30].

For a 20%Ni/Al_2O_3 catalyst Derrouiche and Bianchi[26], estimate the values of heats of CO adsorption (Table 4) for linear and bridge species at coverage equal to 0 and 1 fitting the IR data as function of temperature with the generalized expression of Temkin's model [27].

Table 4: Heats of adsorption for linear and bridge CO over 20%Ni/Al_2O_3 at $\theta_{CO}(0)$ and $\theta_{CO}(1)$[26]

CO adsorbed species	Heat of adsorption, E(0) kJ/mol	Heat of adsorption, E(1) kJ/mol
Linear	153	100
Bridge	147	106

1.4.2 CO activation: initiation steps

Although great efforts have been devoted in the last 90 years to elucidate the FTS mechanism, some aspects are still debated. In particular, even though there is a general consensus on the polymerization character of the process, and the number of authors describing the polymerization monomer as the methylene species (CH_2*) is constantly increasing, the mechanistic details of CO activation and monomer formation have not been univocally identified.

All the popular pathways proposed for the CO activation can be grouped into those involving direct dissociation of chemisorbed CO, followed by reaction of its C* and O* products (referred to as ''unassisted CO dissociation'')[31-37] and those in which chemisorbed hydrogen atoms add to chemisorbed CO molecules before the C–O bond cleavage (''H-assisted CO dissociation'') [38,39].

Density functional theory (DFT) calculations seem to support the key role of H-assisted CO dissociation on both Fe and Co catalysts [40,41,42].

Ojeda et al. [40] try to elucidate the CH_4 formation focusing on the CO activation path during typical Fischer-Tropsch conditions over a Fe–Zn–Cu–K catalyst providing both experimental (kinetic) and theoretical (DFT) evidence for the role of H-assisted CO activation as the exclusive kinetically relevant pathway on Co catalysts at conditions typical of FTS practice.

Figure 10 shows the double activation path proposed for the CO activation by Ojeda et al. [40]:

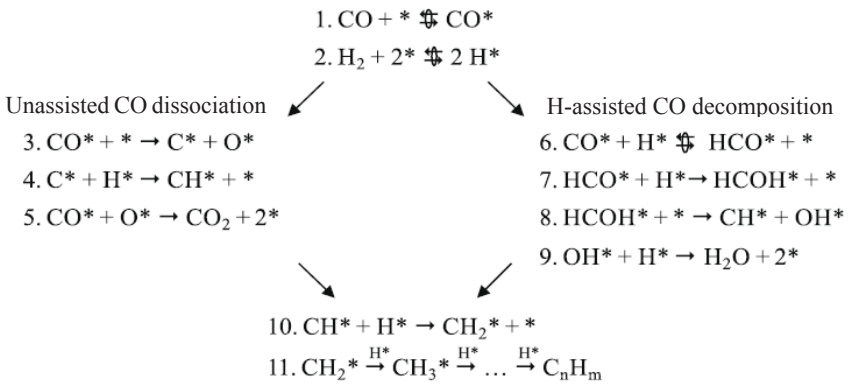

Figure 10: Proposed elementary steps for FTS [40]

In Figure 10 once the CO and H_2 are adsorbed on catalyst surface, the hydrogenation of carbon monoxide proceeds towards two parallel routes. In one the CO* is directly dissociated in C* and O* then the C* is hydrogenated to CH* species, moreover the CO* can react with O* to form the CO_2.

In The second reaction path the CO*, this time is previously hydrogenated to formyl intermediates HCO* and subsequent hydrogenation of the O atom in HCO* species forms hydroxymethylene HCOH* intermediates which dissociation leads to OH* and CH*.

Both reacting path lead to CH* species that are hydrogenated to CH_2* monomer responsible of methane formation and carbon chain growth.

DFT calculations show that on both iron and cobalt catalyst the H-assisted path is the preferred routes due to the less energy required (Figure 11):

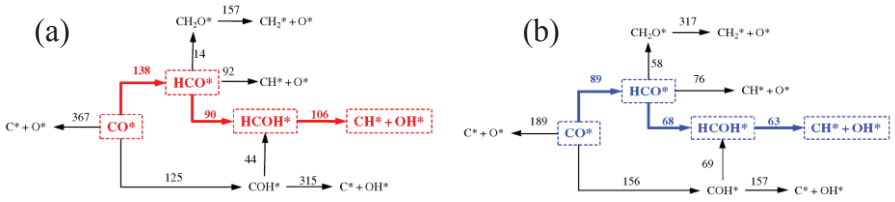

Figure 11: Schematic of the FTS mechanism on (a)Co(0 0 0 1) and (b)Fe(1 1 0) from[40].

Another extensive study, comparing these two CO activation routes, was proposed by Visconti and Tronconi[43,44]. They initially provided a complete kinetic model for the Fischer-Tropsch synthesis over Co/Al_2O_3 in which CO activation path was the unassisted CO* dissociation in C* and O*[44].

A few years later they investigate the possibility to describe the FTS kinetics over Co-based catalysts by replacing the unassisted CO dissociation mechanism with the H-assisted CO dissociation mechanism [43], following the same CO activation path as proposed by Ojeda et al. [40], Figure 12 shows the microkinetic model used by Visconti and Tronconi[43,44].

Step number	Elementary reaction
(1)	$H_2 + 2^* \rightarrow 2H^*$
(2a)	$CO + ^* \rightarrow CO^*$
(2b)	$CO^* + ^* \rightarrow C^* + O^*$
(2c)	$C^* + H^* \rightarrow CH^* + ^*$
(2d)	$CH^* + H^* \rightarrow CH_2^* + ^*$
(2e)	$O^* + H^* \rightarrow OH^* + ^*$
(2f)	$OH^* + H^* \rightarrow H_2O + 2^*$
(3)	$CH_2^* + H^* \rightarrow CH_3^* + ^*$
(4)	$CH_3^* + H^* \rightarrow CH_4 + 2^*$
(5)	$R_n^* + CH_2^* \rightarrow R_{n+1}^* + ^*$
(6)	$R_n^* + H^* \rightarrow P_n + 2^*$
(7)	$R_n^* \leftrightarrow O_n + H^*$
(8)	$R_2^* \leftrightarrow O_2 + H^*$

Step number	Elementary reaction
1.	$H_2 + 2^* \rightleftarrows 2H^*$
2.	$CO + ^* \rightleftarrows CO^*$
3.	$CO^* + H^* \rightleftarrows HCO^* + ^*$
4.	$HCO^* + H^* \rightarrow HCOH^* + ^*$
5.	$HCOH^* + ^* \rightarrow CH^* + OH^*$
6.	$CH^* + H^* \rightarrow CH_2^* + ^*$
7.	$OH^* + H^* \rightarrow H_2O + 2^*$
8.	$CH_2^* + H^* \rightarrow CH_3^* + ^*$
9.	$R_n^* + CH_2^* \rightarrow R_{n+1}^* + ^*$
10a.	$CH_3^* + H^* \rightarrow CH_4^* + ^*$
10b.	$R_n^* + H^* \rightarrow P_n + 2^*$
11a.	$C_2H_5^* \rightleftarrows C_2H_4 + H^*$
11b.	$R_n^* \rightleftarrows O_n + H^*$

Figure 12: Elementary steps involved in the FTS over Co-based catalyst. Left: unassisted CO dissociation [44], right: H assisted CO dissociation [43]

Both microkinetic models were able to describe the linear hydrocarbon product distribution typical of the polymerization reaction like FTS, accounting also for the typical deviations of the FTS products from the ASF model, like the high methane selectivity, the low selectivity to C_2 species and the change of slope with increasing carbon number.

However, they found a better fit, in terms of average relative error, using the H-assisted CO dissociation model and also an increased quality of the fit for the effect of H_2/CO ratio on CO conversion.

So they concluded on the relevance of the H-assisted CO dissociation path, supported also by theoretical calculation from Iglesia[40].

A similar work to that of Tronconi was presented by Azadi[45] and coworkers. They presented a detailed study on the Fischer-Tropsch reaction over $Co/\gamma\text{-}Al_2O_3$ over a full range of syngas conversion.

They fitted the data collected at steady-state, at the operating conditions of H_2/CO=1.8÷2.9 and T=196÷211°C, with a microkinetic model based on the H-assisted CO dissociation path. The model comprises 128 elementary reaction with 85 free parameters.

The model is able to describe the steady-steady state methane formation as well as the paraffins and olefins production (Figure 13).

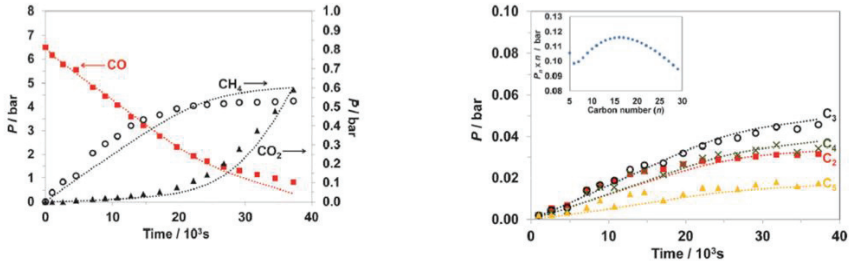

Figure 13: Left: Partial pressures of C_1 species, Right: Partial pressures of paraffins T= 469 K, H_2/CO ratios of 1.8[45]

By coupling transient experiments, microkinetic modeling and theoretical studies, Aparicio[46] proposed the H-assisted CO activation path also for the methanation reaction over Ni catalysts. Aparicio's model has shown a good agreement with experimental data for CH_4 production over Ni catalyst during methanation transient experiment (Figure 14):

1. $H_2 + 2* \leftrightarrow 2*H$
2. $CO + 2* \leftrightarrow **CO$
3. $*H + **CO + 2* \rightarrow **CHO + 3*$
4. $**CHO + 5*H \rightarrow CH_4 + H_2O + 7*$

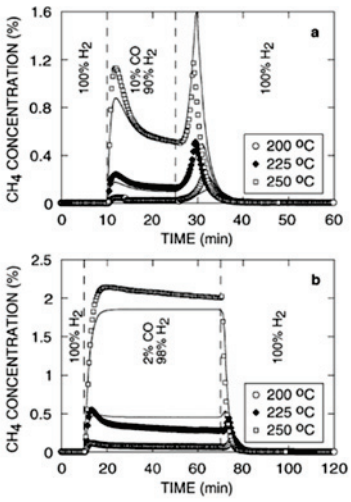

Figure 14: Transient CH_4 responses measured during reaction of CO with H_2. Markers are experimental data, solid lines are microkinetic model.

In this 4-step microkinetic model only two parameters were adjusted to fit the experimental data: the pre-exponential factor and the activation energy of step 3. This step represent the H-assisted CO activation and in this step the adsorbed CO was assumed to occupy two Ni site and to be the rate-determining step.

The CO activation during methantion and Fischer-Tropsch reactions is widely studied through experimental and theoretical work and more and more detailed studies are present in literature that try to explain the products formation as a function of the CO activation path.

1.4.3 Methane formation mechanism

Another subject of debate for the Fischer-Tropsch process is the description of the methane formation mechanism.

Several studies were performed to unravel the methane formation path and different techniques were used.

Van Dijk[47] and coworkers performed an enhanced study on the Fischer –Tropsch and methane formation over Co-based catalysts. They exploited the potential of steady-state isotopic transient kinetic analysis (SSITKA) and based on kinetic modeling they proposed two carbon intermediates that lead to methane C_α and C_β over a $Co/Ru/TiO_2$ catalyst.

They investigated several models that describe the formation of C intermediates leading to CH_4 and the methane formation itself (Figure 15):

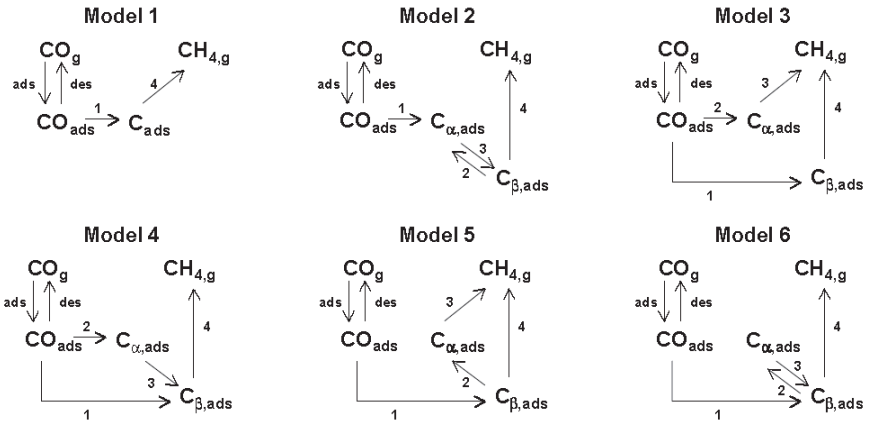

Figure 15: Overview of the potential methanation reaction mechanisms with one or two surface intermediates towards methane[47]

The exact nature of the carbon intermediate pools could not be identified from these experiments. They extended the kinetic study also to the C-C bond formation and the result was that only two models can describe both adequately the methane and the C_2 formation:

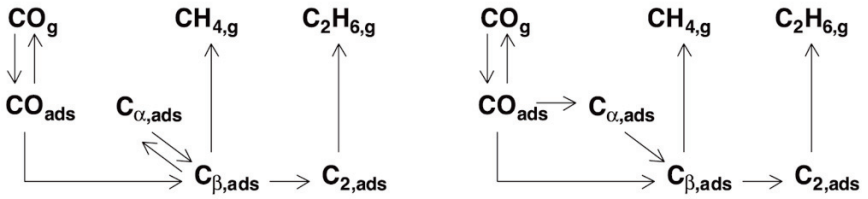

Figure 16: Schematic representation of the most illustrative models for the Fischer–Tropsch reaction [47].

The two pools C_α and C_β are either in parallel or as equilibrated pool, but the surface heterogeneity is shown only for CH_4 and not for the C_2 product, which production is due to the polymerization of C_β intermediates species.

Similar results were obtained in our group by Rebmann[48] and coworkers. They used an extension of the microkinetic model developed by Blanco et al.[49](see section 1.5), and by using the compartment approach, as Van Dijk did, they modeled the isotopic

transient experiment at steady-state. The modeling of ^{12}CO => ^{13}CO showed that the methane and heavier product formation proceeded by a two carbon pool model (Figure 17)

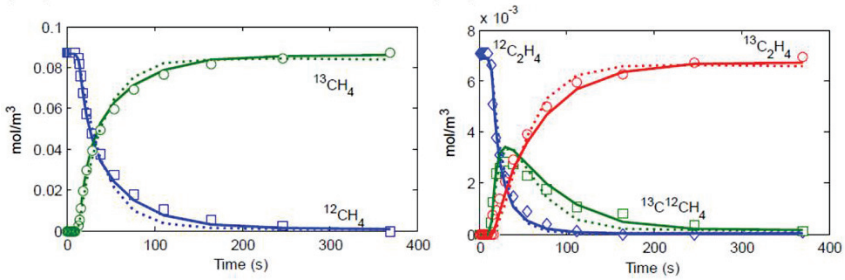

Figure 17: Comparison between experimental and modeled data[48]:one pool carbon (dotted lines) or two pool carbon model (solid lines).

In 2013 Yang et al. [50] coupled isotopic transient modelling and DFT computational chemistry to identify the methane formation path over cobalt based catalyst.

They started from the same hypothesis of Van Dijk, that there are two carbon reacting pools. They further proposed C_α, C_β to correspond to CH_x species and oxygenated complex CH_2O (Figure 18)

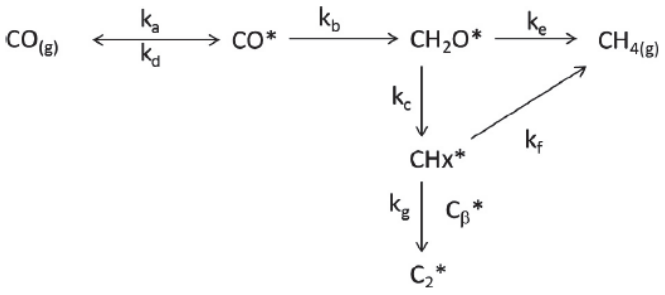

Figure 18: Possible reaction mechanism for methane formation [50]

The results of his studies reveal that a key parameter to determine the pathway for methane formation is the H surface coverage. At low H surface concentrations, high virtual CO partial pressures or low H_2 pressures, the decomposition of CH_2O* was enhanced, while the hydrogenation of CH_2O* was enhanced at high H surface concentrations, namely high virtual H_2 partial pressures or low CO pressures. At relevant industrial F–T conditions, the surface H coverage is expected to be low, and the reaction pathway of methane formation

through decomposition of CHOH* followed by CH* hydrogenation should be dominating.

1.4.4 Water formation mechanism

The aim of a comprehensive kinetic model for methanation or Fischer-Tropsch reaction is to account not only the C-containing products but also the O-containing products. The most abundant O-containing product over a cobalt or nickel catalyst is H_2O.

The kinetic description of water formation is usually performed by 2-3 steps and these depend strongly on the mechanism for the CO activation. Figure 19 shows the water formation steps according the unassisted CO dissociation and the H-assisted CO dissociation paths.

	Reaction Unassisted CO dissociation		Reaction H-assisted CO dissociation
1	$CO+*\rightleftarrows CO*$	1	$CO+**\rightleftarrows CO**$
2	$CO*+*\rightleftarrows C*+O*$	2	$CO**+H*\rightleftarrows HCO*+**$
3	$O*+H*\rightleftarrows OH*+*$	3	$HCO*+H*\rightleftarrows CH*+OH*$
4	$OH*+H*\rightleftarrows H_2O*+*$	4	$OH*+H*\rightleftarrows H_2O*+*$
5	$H_2O*\rightleftarrows H_2O(g)+*$	5	$OH*+OH*\rightleftarrows H_2O*+O*$
		6	$H_2O*\rightleftarrows H_2O(g)+*$

Figure 19: Elementary steps involved in the water formation in FTS reaction

In the direct CO dissociation path the O* produced from the direct dissociation of adsorbed CO* is hydrogenated to OH* and hydrogenated again to H_2O, while in the H-assisted CO dissociation path the OH* species (step 4 and 5) are responsible for water formation.

In general, in microkinetic modeling, the rate of formation of water is assumed faster that methane, but this behavior depends a lot on the operating conditions and the catalyst used.

Yang et al.[51] performed transient experiment tracing the O atom in the CO molecule by means $C^{18}O$ over a $Co/\gamma\text{-}Al_2O_3$.

They exposed a freshly reduced cobalt catalyst with a $C^{18}O$/Kr mixture and then exposed the catalyst to H_2. They followed the production of CH_4 and $H_2{}^{18}O$ during the isothermal hydrogenation (Figure 20).

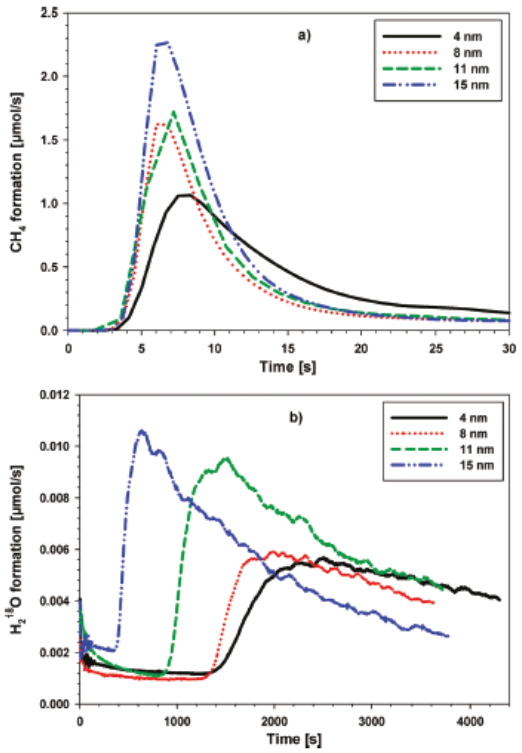

Figure 20: Formation of (a)CH_4 and (b)$H_2{}^{18}O$ during isothermal hydrogenation of surface carbon and oxygen species deposited by the $C^{18}O$ exposure experiment for catalysts with different particle size. The isothermal hydrogenation is carried out in pure H_2 (15 mL/min) at 210°C,1.85 bar.[51]

They found water formation sensibly slower than methane production and this effect was more relevant with decreasing the particle size. Due to the incomplete release of $^{18}O^*$, the total amount of $^{18}O^*$ species derived from isothermal hydrogenation was difficult to determine.

The water formation has been studied more for the its effect on the catalyst, deactivation process and on the selectivity to hydrocarbons produced during Fischer-Tropsch reaction.

Claeys and van Steen[52] found an interesting results by increasing the partial pressure of H_2O during Fischer-Tropsch reaction over a ruthenium supported catalyst.

They found a decreasing of selectivity to CH_4 and an increased selectivity to C_{5+}. They used a macrokinetic expression proposed in previous studies [53] on iron and cobalt based catalysts to fit the data:

$$r_{C,org} = \frac{aP_{CO}P_{H_2}^{1.5}/P_{H_2O}}{\left(1 + bP_{CO}P_{H_2}/P_{H_2O}\right)^2}$$

This equation predicts a positive effect of water at low syngas conversion levels. An increase in water partial pressure would lead to a decrease in the surface concentration of carbon, which is thought to occupy most of the catalyst surface and to inhibit the Fischer–Tropsch reaction. Moreover, water supplies a source of surface hydrogen, which is needed to form CH_2* and CH_3* and alkyl surface species leading to enhanced increase in CO-consumption. This increased availability of monomer species might also explain the experimentally observed increase in primary chain growth probability or C_{5+} selectivity.

The conclusion of Clayes and Van Steen are consistent with the work presented by Storsæter et al.[54]. They studied the water effect during Fischer-Tropsch (T=210°C, H_2/CO=2.1 and P_{tot}= 20 bar) reaction for several promoted and un-promoted catalytic systems with different supports.

By adding external water (≈ 20%) or increasing the conversion Storsæter[54] found for all the studied catalyst again a decrease of methane selectivity and an increase for the selectivity to C_{5+}.

On the other side, increasing the amount of added water lead to a faster deactivation of catalysts due to the re-oxidation of smaller particles [54,55].

1.5 Kinetic investigation of Fischer-Tropsch reaction

As shown in previous sections, the Fischer-Tropsch process is extensively studied by means of modeling experimental data. These data provide kinetic measurements of the reaction mechanism and reaction kinetics.

To develop a model that describe the complexity of surface catalytic reaction basically two main families of experimental techniques are used:

1. Steady-state experiments
2. Transient experiment

1.5.1 Steady-State experiments

The steady–state experiment is the most common reaction technique used in heterogeneous catalysis.

The data are achieved by operation such that temperature, pressure, concentration and flow rate and any point in the reactor is time invariant. They provide experimental measurements that allow to access to catalyst's activity, selectivity, reaction order and activation energy.

The main advantages of steady-state experiments are:

- Setup easy to build and to operate
- The results can be described with relative simple algebraic mathematical model
- Most industrial processes operate under steady-state conditions.

However, they presents some drawbacks like:

- They provide a global kinetic parameters estimation limiting the information on individual reaction steps.
- The interpretations of kinetic data are often based on strong assumptions.

1.5.2 Unsteady-state (Transient) experiments

When the aim of the kinetic investigation is a more detailed analysis of the catalytic surface reaction, transient experiment are a more efficient technique to get access to the surface information.

The transient technique provides information on:

- Reaction intermediates(i.e. pulse experiment, isotopic tracing experiment)
- Reaction sequence in a multi-step reaction (i.e. parallel multi-step, multi-step in series)
- Provide rate constants of elementary steps.

However, for transient experiment the complexity of setup increases a lot compared to the steady-state experiment and also the theory used for the data interpretation is more complex.

The steady-state isotopic transient kinetic analysis (SSITKA) represents a powerful tool used for kinetic investigation of heterogeneous catalyzed reaction because it allows a link to the surface intermediates due to the isotopic transient behavior and at the same time is performed at steady state so the reactant. The SSITKA technique will be presented in chapter 2 with all the associated assumptions and hypotheses.

1.5.3 Macrokinetics and Microkinetics modeling of Fischer-Tropsch process

Two main families of kinetic models are encountered in literature: macrokinetic models, that provide information on global kinetics and often represented by simple rate expressions like Langmuir-Hinshelwood or Eley-Rideal equations and microkinetic models that are based on a detailed mechanistic basis that represent data well over a wide range of conditions. They often cannot be expressed as an explicit rate equation and are solved numerically.
Transient experimental data require in general microkinetic modeling approaches. Microkinetic models, due to the large number of reaction steps that contain, are more difficult to use and a major issue is to obtain a consistent set of rate parameters for all individual steps.
Adsorption and activation energies as well as pre-exponential factors calculated from DFT are often used as an input for a microkinetic model

and thus make the link to compare the DFT study to experimental results.

Table 5 and Table 6 show some macrokinetic rate equations reported in literature for the CO consumption and the methane formation during FTS over Co-based catalysts.

Table 5: Representative Simple Reaction Rate Equations for CO Consumption in FTS on Co, adapted from [56]

Kinetic expression	**Mechanistic Implications**	**References**
$-r_{CO} = aP_{CO}^{-0.2}P_{H_2}^{0.7}$	CO inhibits reaction; CO*;* strongly adsorbed; high θco	[57,58]
$-r_{CO} = \frac{aP_{CO}P_{H_2}}{(1+bP_{CO})^2}$	high θco*;* enolic mechanism; hydrogenation of HCOH (rds)	[59]
$-r_{CO} = \frac{aP_{CO}^{m}P_{H_2}^{n}}{1+bP_{CO}}$ $m = 0.5-0.6$ $n = 0.6-0.9$	moderate θco*;* Eley-Rideal; stepwise hydrogenation of C*	[60,61]
$-r_{CO} = \frac{aP_{CO}^{0.5}P_{H_2}^{0.5}}{(1+bP_{CO}^{0.5})^2}$	high θco*;* C* + H* and O* + H* are rds's	[62]

Table 6: Summary of CH_4 Kinetic Models in FTS on Co, adapted from [63]

Kinetic expression	References
$r_{CH_4} = kP_{CO}^{n_1} P_{H_2}^{n_2}$	[64]
$r_{CH_4} = \frac{kP_{CO}^{0.5} P_{H_2}^{0.5}}{\left(1 + K_1 P_{CO}^{0.5} + K_2 P_{H_2}^{0.5}\right)^2}$	[62]
$r_{CH_4} = \frac{kP_{CO} P_{H_2}^{0.5}}{\left(1 + K_1 P_{CO} + K_2 P_{H_2}^{0.5}\right)^2}$	[62]
$r_{CH_4} = \frac{kP_{H_2}}{(1 + K_1 P_{CO}^{0.5})^2}$	[65]
$r_{CH_4} = \frac{kP_{H_2}}{(1 + K_1 P_{CO})^2}$	[65]

Table 5 and Table 6 reveal a variety of rate expressions that describe for both CO and CH_4 the global kinetic behavior at steady-state, but with these macrokinetic rate expressions it is not possible to access to the detailed mechanistic information related to the catalyst's surface under reaction conditions.

In summary, significant progress has been made in the last two decades in the development of microkinetic models for methanation and

Fischer-Tropsch synthesis. SSITKA technique can provide a more comprehensive description of reacting surface, however is based on very elaborate lots of parameters and is clear that to have a mechanistically-meaningful model has to be coupled to other experimental and theoretical techniques.

1.6 Computational and Theoretical Chemistry

The increase of calculation power in the last years lead to an explosion of studies based on computational and theoretical chemistry.

Since the 1990's, theoretical studies based on periodic slab Density Functional Theory (DFT) try to shed light on the possible reaction paths by calculating the energy barriers that link the proposed intermediates[66]. Thermodynamic and kinetic analyses of these results for a given surface then enable discriminating the most probable reaction pathway. However, the surface metal geometry/composition, which is one of the principal assumptions that need to be done to initiate the calculation, is still under debate.

Co(0001) had been used as an ideal surface by Saeys et al.[67], Iglesia et al. [40], King et al. [68], Niemantsverdriet et al. [69]. They all converge to the same conclusion: the CO dissociation proceeds with high energy barriers on flat Co whereas CO hydrogenation barriers are more favorable, see Table 7.

Table 7: Activation Barriers calculated on Co(0001) by Saeys et al.[67]

Mechanism	Reaction Path	Activation Barrier (kJ/mol)
CO Dissociation	CO→C+O	220
CO Hydrogenation	CO→HCO	146
	HCO→H_2CO	60
	HCO→ HC+ O	90
	H_2CO→H_2C + O	68
	RCH_2CHO→RCH_2CH + O	50

Cheng et al.[70] performed an extensive DFT study to investigate the mechanism of FTS over cobalt over flat and stepped Co(0001) surface.

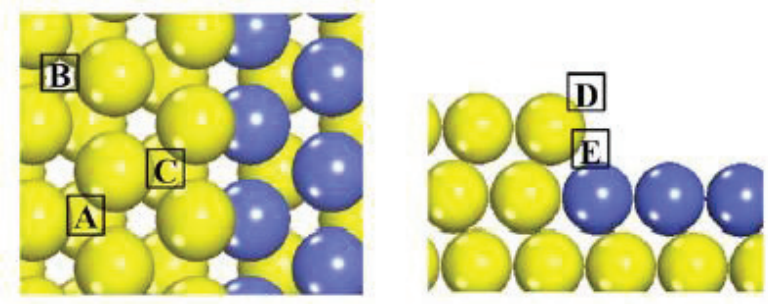

Figure 21: The top view (left), the side view (Right) of the stepped Co(0001). The Co atoms on the top terrace are in yellow, the Co atoms on the terrace below in blue.[70]

They found that the CH_x species formation barriers are lower on step than on terraces and that the steps are the active site for the C-C coupling during FT.

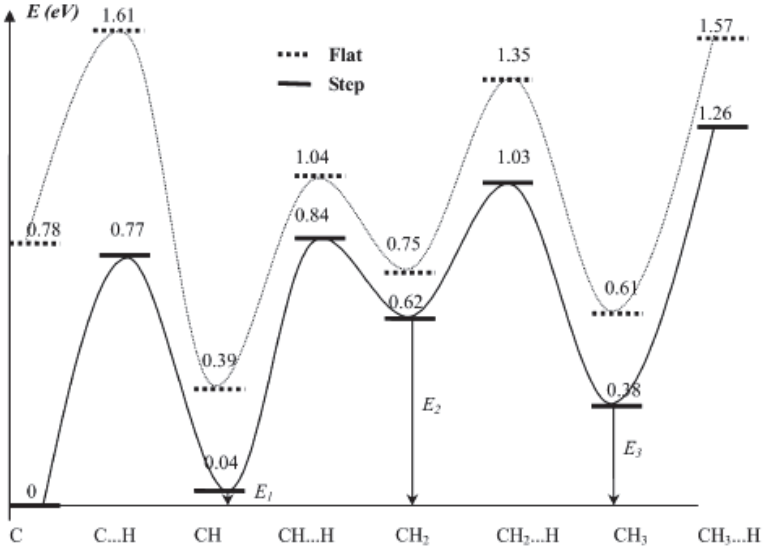

Figure 22: Energy profiles of carbon hydrogenation on the flat and stepped Co(0001). The IS of C* + 4H* on the step sites is chosen as the zero point for both the energy profiles. E_i (i = 1, 2, 3) is the energy difference between adsorbed CH* and C* on the both sites.

Klinke and Broadbelt[71] used a combination of theoretical computational methods to generate a mechanistic model for FTS on Ni(111) and Co(0001).

The method included a linear programming algorithm to generate possible intermediates, products, and reaction pathways with heat of reaction as a reactivity index; calculation of binding energies of key intermediates by ab initio methods; estimation of pre-exponential factors from collision and transition-state theories and of activation energies from linear free energy relationships; and bond-energy, bond-order calculations of heats of adsorption.

Predictions of $C_1 - C_4$ hydrocarbon yields were in good agreement with published experimental data for Co and Ni catalysts. The computer-generated mechanism suggested that for both Co and Ni, CH formation from C and H is the most energetically, favorable hydrogenation step, while the hydrogenation of CH to CH_2 is the slowest step.

Another theoretical method that has been widely applied to the FTS in order to evaluate the activation energies involved in each elementary steps of the reaction network is the Unique Bond Index-Quadratic Energy Potential (UBI-QEP) method. The method is extensively reviewed by Shustorovich and Sellers[72].

This UBI-QEP approach starts from the a priori proposition of the mechanism on the atomic binding energies on the metal (eg. Co-C, Co-O and Co-H) and on a knowledge of the thermochemistry data that link the reactants, the intermediates and the products in the gas phase. Pre-exponential factors cannot be calculated by the UBI-QEB method, but can be evaluated through transition state theory. Finally the rate constant is calculated with the Arrhenius law.

Storsæter et al. [74] propose the comparison between the CO dissociation and the CO insertion mechanism. By using the UBI-QEP values in a microkinetic model and with an adjustment of the atomic binding energies and some selected activation energies on a steady-state dataset at 2 temperatures (483 and 493K), they found the best fit for the CO insertion mechanism. According to UBI-QEP calculations, the activation energies for dissociation of adsorbed CO and hydrogenation of surface carbon are too high for the carbide mechanism to occur.

By adjusting the atomic binding energies and activation energies from UBI-QEP calculations combined with a single-event microkinetic model, Blanco et al.[49] managed to fit their steady-state data over a FT iron catalyst at 493K based on the carbide mechanism at various contact times and partial pressures. The activation energies were strongly altered by this adjustment compared to the initial UBI-QEP estimations with some deviation even higher than 50 kJ/mol for some key steps of the monomer species production.

Van Belleghem et al.[75] extended Blancos' model to cobalt catalysts. They investigated the carbide mechanism and they found an activation energy for the CO dissociation of 52 kJ/mol which they found to be reasonably close to the value of Klinke and Broadbelt of 72 kJ/mol. They found a higher activation energies for the hydrogenation steps of O* and OH* species, that could justify a slower water formation than methane.

1.7 Aim, scope, and outline of this thesis

To rationally design improved FT catalysts, a thorough understanding of the reaction mechanism is required.

The aim of this work is to obtain a better understanding of the Fischer-Tropsch reaction mechanism over Co and Ni-based catalysts, especially for the methane formation pathway.

In literature, controversy still exists on the reactivity, the abundance, and the chemical identity of the surface species participating to the methane formation pathway. In contrast to steady state kinetic techniques, transient kinetic techniques have a high potential to answer these questions.

Steady State Isotopic Transient Kinetic Analysis is most promising, since it is operated under steady state but providing transient information. During a SSITKA experiment, a reactant is replaced by its labelled counterpart and the evolution of the label in reactant and products is monitored in time. These transient responses contain information about the abundance, reactivity, chemical identity, and surface heterogeneity of the participating species, which renders the SSITKA technique powerful for mechanistic investigations of complex reactions. These experiments are complemented by step-transient under non-steady-state conditions.

The outline of this thesis work is:

- ✓ In chapter 2, the SSITKA and step-transient experimental methodologies are described in detail. The assumptions on the plug-flow reactor (PFR) model used in this study for parameter estimation and data fitting are presented.
- ✓ In chapter 3, the SSITKA and step-transient setup will be presented as well as the tested catalysts, cobalt and nickel supported over silicon carbide (SiC) and alumina (γ-Al_2O_3), and the characterization procedure, moreover all the experiment protocols will be described in the detail.
- ✓ The experimental results are discussed in the first part of chapter 4, focusing on the isotopic composition of methane, water. Cobalt and nickel catalysts were tested in this study to compare the methane formation pathway. The metal phase was supported over two different supports: silicon carbide (SiC) and alumina (γ-Al_2O_3) to understand the role that the support plays during the reaction.
- ✓ Chapter 5 will discuss modeling the SSITKA and step-transient responses. Regression analysis for parameter optimization will be presented.
- ✓ Finally, Chapter 6 summarizes the main conclusions of this study focusing on the microkinetic modeling of methane formation and will suggest some further perspectives.

Chapter 2

Methodology and model development

This chapter describes the methodology of steady-state isotopic transient kinetic analysis and the assumptions on the plug-flow reactor model for parameter estimation and data fitting

2.1 Experimental methodology

2.1.1 Steady state isotopic transient kinetic analysis (SSITKA)

A steady state kinetic model can be applied if a time-invariant reaction rate is observed for fixed process conditions or if the process conditions are changed on a time scale much larger than the relaxation time of the catalytic reaction[76]. In contrast, a transient kinetic model is needed if the process conditions are changed on a time scale similar to or smaller than the relaxation time of the reaction.

The steady-state isotopic transient kinetic analysis was largely developed by Happel, Biloen and Bennet[77,80,81] and extensively reviewed by Shannon and Goodwin in 1995 [76] and Holmen et al.[50,51].

This technique consists of reaching the steady-state of a given reaction. Then an abrupt perturbation is applied by continuous or temporary isotopic replacement of one of the reactants. The disturbance at the reactor outlet is observed via mass spectroscopic techniques that discriminate the relative isotopic composition and allow to get a time-resolved analysis. The obtained transient signals results of the system relaxation that tends to recover its isotopic steady-state.

By choosing labeled reactants, that does not perturb the overall chemical steady-state, like $^{12}CO/^{13}CO$, the chemical surface intermediates composition remains unchanged after the isotopic switch. Consequently, SSITKA enables to observe the system dynamics at isobaric, isotherm and steady-state condition. This is only valid if no kinetic isotope effect occurs.

The kinetic isotopic effect (KIE) is defined as the ratio of the unlabeled and labeled reaction rates (r/r*). If this ratio is greater than unity, the isotope effect is normal. If the ratio is less than unity, it is called an inverse kinetic isotopic effect. A well-known case of inverse isotopic effect is the Fischer-Tropsch or methanation reaction performed with deuterium instead of hydrogen. In this case the ratio r_{H2}/r_{D2} is less than unity as shown from the studies of Yang et al.[50], see Table 8.

Table 8: Kinetic isotope effects (KIE) for the overall reaction and the methane formation. r_H is the rate with CO/H_2 and r_D is the rate with CO/D_2 as reactants[50]. Conditions: 483 K, 1.85 bar and $H_2/CO = D_2/CO = 10$

Reaction rate [μmol/(g_{cat}s)]	r_H	r_D	KIE = r_H/r_D
r_{CO}	3.607	4.604	0.78
r_{CH4}	2.349	2.383	0.99

The integration and the shape of the transient responses contain kinetic information about the underlying surface mechanism or a given reaction which transforms reactant (R) into product (P) via intermediates (I), which concentration of R is imposed at the reactor inlet and concentration of P is typically measured at the outlet. In heterogeneous catalytic systems, the generated intermediates occupy a certain fraction of the catalyst surface and direct quantification under operating condition is usually inaccessible.

$$R \leftrightarrow I_1 \leftrightarrow I_2 \leftrightarrow \cdots \leftrightarrow I_n \leftrightarrow P$$

The power of the SSITKA technique is that whatever the complexity of the underlying mechanism, it enables quantifying the amount N_P moles of surface intermediates leading to the product P ($N_P = \Sigma N_{In}$). It must be noticed that if several products are possible or if labeled reactants are reversibly adsorbed on the surface, N_P only refers to a fraction of the total amount of intermediates I_i from R leading to P.

Experimentally (Figure 23), after introduction of a labeled reactant, the production reaction rate r_P of the unlabelled product P decrease from r_P at t=0s (steady-state) to 0 at $t \rightarrow \infty$

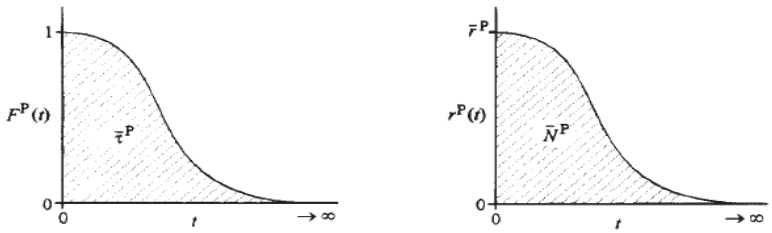

Figure 23: On the right: Typical steady-state isotopic transient rate responses showing the surface-intermediate abundance. On the left: Typical normalized steady-state isotopic transient responses showing the overall mean surface-residence time

N_P is directly obtained by signal integration:

$$N_p = \int_0^\infty r_p(t)\, dt$$

Eq. 5

Hence, it is also possible to obtained the mean surface residence time τ_p, by simple integration of the normalized response $F_P(t)$ (Figure 23):

$$\tau_p = \int_0^\infty F_p(t)\, dt$$

Eq. 6

Finally, rearrangement of these equations gives the general relation:

$$N_p = \tau_p \cdot r_p$$

Eq. 7

It is emphasized that this straightforward data treatment does not need any mechanistic assumption or exhaustive knowledge of the different intermediates pools and their interconnection.

Only for simple systems with a single reaction intermediate that link an irreversibly adsorbed reactant to product which can't readsorb and assuming a pseudo first order reaction rate expression, the TOF, the kinetic constant k and surface coverage θ are directly related by:

$$R \overset{r_R}{\rightarrow} I \underset{F_{P(t)}}{\overset{r_P}{\rightarrow}} P$$

$$TOF_P = \frac{r_P}{N_s} = \tau_P^{-1} \frac{N_P}{N_s} = k\theta_P$$

Where:

TOF_p is the turnover frequency for a product P

r_P is the rate of formation of product P

τ_p is the mean surface residence time of intermediates leading to product P

N_p is the amount of intermediates leading to product P

N_s is the total abundance of catalyst-surface active site

θ_p is the surface coverage of intermediates leading to product P

Within the above mentioned assumptions the latter equation shows the power of the SSITKA technique. That is, direct data analysis decouples the surface coverage and the kinetic constant to reach the intrinsic activity of the catalyst at steady-state but it is emphasized that the associated assumptions must be carefully checked for valid results.

However, for mechanistic investigation involving a large system with adsorption/desorption equilibria and or reversible reactions, direct data treatment is no longer relevant. Indeed, no easy analytic solutions are available for the underlying differential equations. Data analysis requires micro-kinetic modeling.

Note that a good fit afforded through the exploration and the adjustment of the different reaction mechanisms is not an evidence of the uniqueness of the "solution" [82,83-85]. The mechanisms with a unique surface intermediates or a limited number of intermediates in series (Figure 24, I and II respectively) produce distinguishable responses (Figure 24, A, I&II). The presence of successive intermediates tends to delay the response and to induce an upward convexity of the response compared to the mono-intermediate route. However, for more complex networks such as III, IV and V, with parallel pathways and/or buffer steps, different systems can produce the same temporal response. For example, Figure 24 B shows that the same response can be produced by the couple III/IV and V/VI. It can be expected that several mechanisms would produce a good fit with close satisfactory statistics so that several potential mechanisms could be proposed as a solution. Other mechanisms can be discarded due to a significantly higher lack of fit.

Figure 24 B-C shows the impact of the reactor design on the responses (C: continuously stirred tank reactor and D: Plug flow reactor) and

that both CSTR and PFR tends to the same response at differential conditions (small reactor volume and small conversion).

The SSITKA technique has already been applied to numerous catalyzed reactions. These include the ammonia synthesis, CO oxidation, ethylene hydroformylation, methanol synthesis, methanol reforming, NOx reduction, propene epoxidation and most relevant to this study, methanation and the Fischer-Tropsch synthesis[47,77,80,81,85].

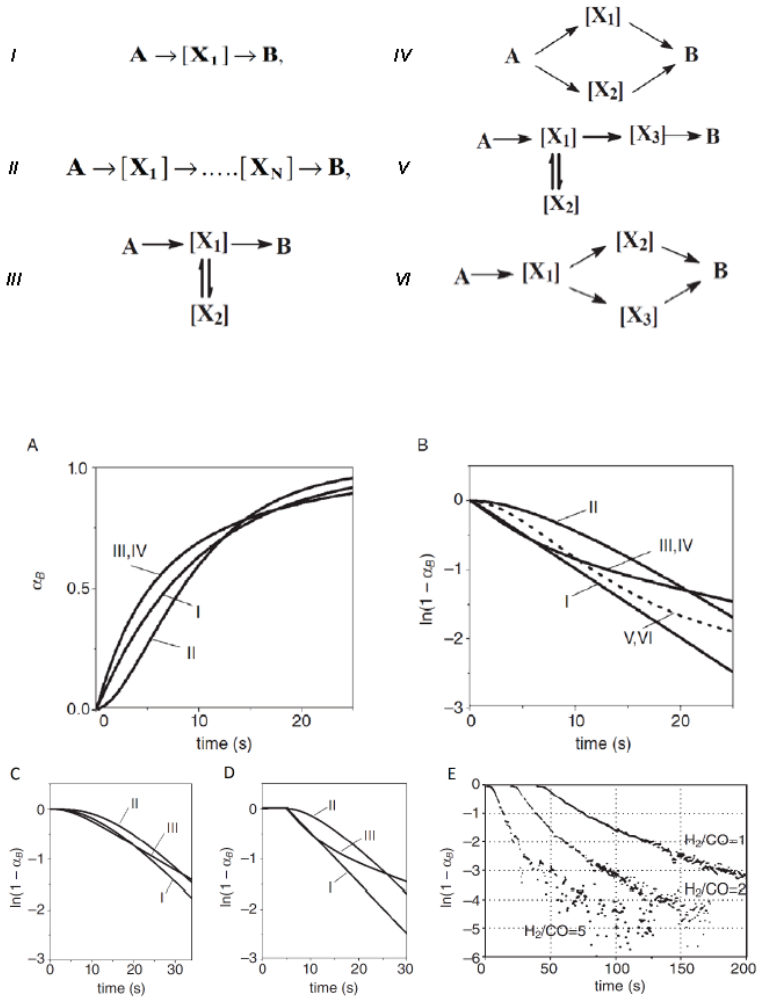

Figure 24: Time dependences of the linear (A) and the logarithmic isotope fraction in the reaction product for different types of reaction mechanisms in a CSTR (C) and plug-flow reactor (D) in comparison with a differential reactor (B), (E) Decay of ^{12}C in Methane monitored by MS(Adapted from [47,86,87]).

2.1.2 Step-transient technique

To get further mechanistic information SSITKA switches are combined with step-transient experiment.

During this technique, the chemical composition of the gas phase is changed abruptly from inert to reaction conditions to allow studying the build-up of steady-state reaction conditions with time. Once these conditions are reached, switching back to inert mixture allows scavenging the reactive surface states (Figure 25):

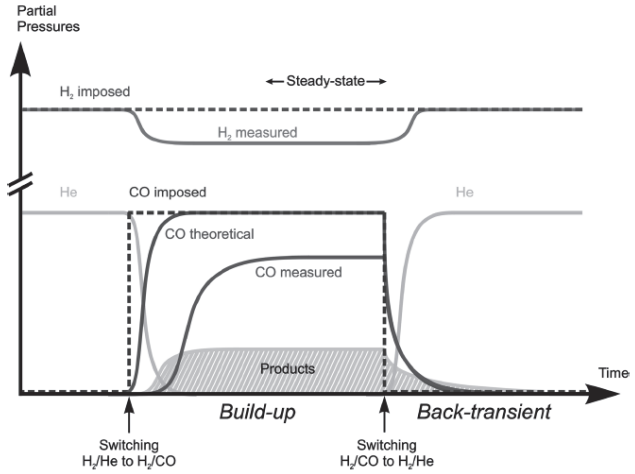

Figure 25: Principle of chemical transient kinetics applied to the CO + H_2 reaction[88].

With this technique it is possible to get information about the most abundant species during the reaction in the first seconds and at steady-state.

In case of Fischer-Tropsch and methanation reactions it is possible to estimate the amounts of C, O and H from the following surface balance[88]:

$$C_{ads} = \int_0^t \left(F_{CO}^{theor} - F_{CO} - F_{CH_4}\right)dt$$

$$O_{ads} = \int_0^t \left(F_{CO}^{theor} - F_{CO} - F_{H_2O}\right)dt$$

$$H_{ads} = 2\int_0^t \left(F_{H_2}^{theor} - F_{H_2} - F_{H_2O} - 2F_{CH_4}\right)dt$$

Where the molar flowrate F_i for each gaseous species, monitored with the mass spectrometer, is integrated over time and F^{theor} is known from the molar flow at the reactor inlet.

2.2 Model Assumptions

For an unambiguous interpretation of the transient responses obtained with SSITKA and Step-Transient experiments, the kinetic observation has to obey several restrictions:

- absence of internal and external temperature and mass gradients on catalyst pellet scale;
- absence of kinetic isotope effects;
- isothermal and isobaric operation of the reactor;
- constant total molar flow rate;
- time constants of the kinetic processes sufficiently larger than those of the mixing curve.

In this work axial dispersion model for a fixed bed reactor is used to model the hydrodynamics. The following section will describe the equations on which the model is based.

2.3 Fixed bed reactor model

The experimental data are obtained in an integral operated fixed bed reactor.

The reactor model is represented by partial differential equations in time and in space for all the components that participate in the reaction mechanism.

The transient model is based on a one-dimensional pseudo-homogeneous fixed bed reactor, thus assuming no radial and no external and internal mass and heat transfer limitations. The gas velocity is assumed to be constant. The continuity equations are then given for the gas phase and adsorbed phase respectively as Eq. 8-Eq. 10:

$$\varepsilon_b \frac{\partial C_i}{\partial t} = -\frac{\partial (uC_i)}{\partial z} + \varepsilon_b D_{ax,i} \frac{\partial^2 C_i}{\partial z^2} - (1-\varepsilon_b) L_t \left(k_{ads,i} C_i RT\theta_* - k_{des,i}\theta_i \right)$$

Eq. 8

$$\sum_{i=1}^{k} C_i = \frac{P}{RT}$$

Eq. 9

$$\frac{\partial \theta_i}{\partial t} = \sum_{j=1}^{n} \nu_{ij} k_j \prod_k (c_i RT)^{n_k} \prod_m \theta^{n_m}$$

Eq. 10

where, ε_b is the bed porosity (m^3_{void}/m^3_r), C_i the molar gas concentration (mol/m^3), t the time (s), z the axial coordinate (m_r), L_t is the number of active sites per catalyst volume (mol/m^3_{cat}), u the superficial gas velocity ($m^3_g/m^2_r/s$) and D_{ax} the axial diffusion coefficient ($m^3_g/m_r/s$). Together with the following initial and boundary conditions:

$$t = 0 \wedge 0 \le z \le L: \; C_i = 0 \quad \wedge \quad \theta_i(z) = 0$$

$$t \ge 0 \wedge z = 0: \; C_i = C_i^0$$

This set of partial differential equations is transformed into a set of ordinary differential equations by the methods of lines[89] and integrated numerically using the ODEPACK library[90]. The integration routine is coupled to a non-linear regression analysis routine based on Marquardt's algorithm[91]. After the optimization, the variance/covariance matrix is calculated and a statistical analysis is performed.

The axial diffusion coefficient is calculated by first calculating the molecular diffusion coefficient for each component in the mixture by using the Fuller equation[92] at a fixed composition of the mixture (Eq. 11).

$$D_{AB} = \frac{10^{-3}\, T^{1.75}\left(\frac{1}{M_A}+\frac{1}{M_B}\right)^{0.5}}{P\left[(\sum V_A)^{\frac{1}{3}}+(\sum V_B)^{\frac{1}{3}}\right]^2}$$

Eq. 11

Then the following correlation is used:

$$D_{ax,i} = 0.73\, D_{AB,i} + u * d_p$$

The change of the superficial gas velocity due to reaction is very small, less than 5% and no significant impact on the shape of the step-responses of reactants and products was observed. The superficial gas velocity has been fixed at a constant value to speed up regression analysis.

The function, f(C_A), used to describe the switching of the four-way valve is the Heaviside function (Eq. 12):

$$f(t) = \frac{(1-e^{-at})}{(1+e^{-at})}$$

Eq. 12

This function contains one adjustable parameter, the time constant "a" that is optimized using the inert tracer step-response during a SSITKA experiment, as shown in Figure 26.

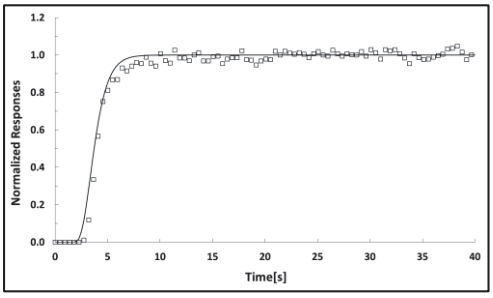

Figure 26: The optimal fit for inert tracer step-response used for SSITKA modeling. The inert tracer is krypton and the value of parameter a=1.2

2.5 Regression analysis

The adjustable model parameters and the activation energies of the forward reactions are estimated by a least squares optimization in which the following objective function is applied:

$$\phi = \left\{ \sum_{i=1}^{n_{exp}} \left[\sum_{j=1}^{n_{resp}} w_j (y_{ij} - \hat{y}_{ij})^2 \right] \right\} \rightarrow min$$

Eq. 13

Where n_{exp} represents the number of experiments, n_{resp} the number of responses in each experiment, w_j the statistical weight corresponding to response j, y_{ij} the experimental response j in experiment i, $\hat{y}_{ij}$ the model simulated value for response j in experiment i. The statistical weight factors, w_j, are calculated from the inverse of the covariance of the experimental errors:

$$w_j = \left[\frac{\sum_{i=1}^{n_{exp}} \left(y_{ij} - \hat{y}_{ij} \right)^2}{n_{exp} n_{resp} - n_{par}} \right]^{-1}$$

Where n_{par} represents the number of adjustable model parameters. The statistical weights, w_j, are determined via an iterative procedure in which updates for w_j are determined from the model responses obtained with values for w_j from the last iteration. This is repeated until convergence, typically requiring only 4 or 5 iterations. Initial estimates for the w_j can be determined from the inverse of the experimental error if repeat experiments are available.

The non-linear least-square regression analysis has been performed by the multirespons Levenberg-Marquardt minimization algorithm[91,94,95 96]. The algorithm allows to find the actual minimum of the objective function.

2.6 Statistical analysis

The regression significance was assessed via statistical tests. The standard F test requires replicate experiments. If no replicates have been performed an alternative, less rigorous test is [97]:

$$F_c = \frac{\sum_{i=1}^{n}(w_j \hat{y}_i^2 / p)}{\sum_{i=1}^{n}\frac{w_j (y_i - \hat{y}_i)^2}{n-p}}$$

Where:

y_i is the experimental value

$\hat{y}_i$ is the calculated value

n is the number of experimental points

p is the number of parameters

If F_c is larger than the tabulated F(p,n-p;0.05) the regression is considered to be meaningful. Statistical testing can also be applied to the parameter estimates. When the model exhibits no lack of fit, an unbiased estimate of the experimental error is given by:

$$s^2 = \frac{\sum_{i=1}^{n}(y_i - \hat{y}_i)^2}{n-p}$$

The statistical significance of each individual parameter estimate is also assessed. This is done by a t test. In this test, it is verified whether the parameter is statistically significantly different from a postulated value, typically zero. The t value of a parameter in this case is calculated as given by:

$$t_c = \frac{|b_i|}{\sqrt{[V(b)]_{ii}}}$$

Where t_c represents the calculated t value, b_i the parameter estimate and $[V(b)]_{ii}$ the ith diagonal element of the variance-covariance matrix.

Now an estimate of the variance-covariance matrix is given by:

$$\overline{V}(b) = (J^T J)^{-1} s^2$$

the individual confidence limits are given by

$$b_i - t(n-p, 1-\alpha/2)\sqrt{V(b)_{ii}} \leq \beta_i \leq b_i + t(n-p, 1-\alpha/2)\sqrt{V(b)_{ii}}$$

These delimit the region of values of b_i that are not significantly different from the optimal estimate b_i at the selected probability level 1-α, which is in the case of non-linear regression only approximate. Note that a high correlation between two parameters invalidates the individual confidence limits.

The binary correlation coefficient between parameter i and parameter j is calculated by means of the variance-covariance matrix of the parameters:

$$\rho_{ij} = \frac{[V(b)]_{ii}}{\sqrt{[V(b)]_{ii}\,[V(b)]_{jj}}}$$

Parameters are considered to be correlated if $|\rho_{ij}| > 0.9$

Chapter 3

Experimental

The next chapter describes the experimental setup for catalytic experiment, the tested catalysts and the characterization techniques.

3.1 Transient Experimental Setup

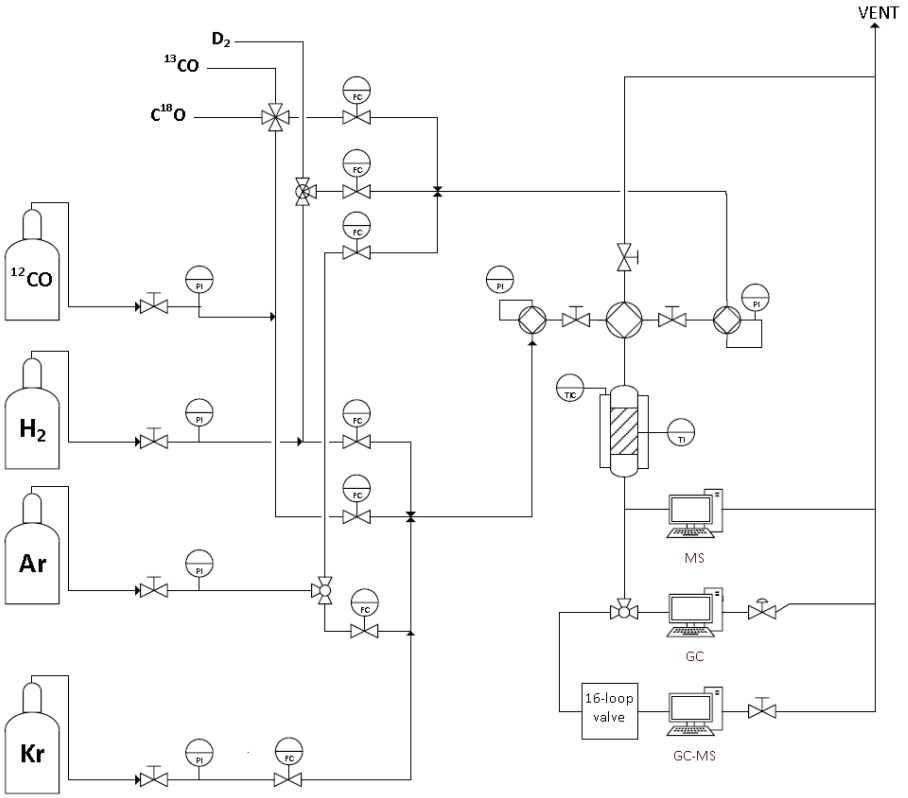

Figure 27: Schematic representation of transient set-up.

The experimental SSITKA set-up consists of a feed, reactor, and analysis section. A schematic representation of the set-up is given in Figure 27 and each section will be discussed in detail below. During the experiment, one reactant is abruptly replaced by its labeled counterpart, while an inert tracer is abruptly removed from the feed. The incorporation of the labeled atom into the reaction products is monitored in time and yields information about the underlying reaction mechanism and the chemical composition of the participating surface species.

For a ^{13}C-labeling experiment, the isotopic step-change is represented by:

$$\mathbf{Ar/^{12}CO/H_2 \rightarrow Ar/Kr/^{13}CO/H_2}$$

During the transient experiment, a fast isotopic step-change is required without pressure effects caused by the actual switching. Pressure effects will change the intensity of the signals measured at the outlet due to a changing total pressure in the analysis chamber of the mass spectrometer.

Obviously, these responses are not related to changes in the composition of the gas phase and are therefore not desired. This is prevented if the following conditions are met:

1) Equal total flows;

2) Equal flow compositions;

3) Equal pressure-drops towards vent and analysis section.

Restrictions 1) and 2) are met in the feed section, while restriction 3) is met in the reactor section.

3.1.1 Feed section

Mass flow controllers (Brooks) for every component in the feed section provide two feed streams with identical composition and total flow. This satisfies the first two restrictions for the generation of an isotopic step-change without pressure effects. One feed stream contains a maximum of 5 vol% Kr as inert tracer to monitor both the quality of the isotopic step and the gas hold-up in the reactor system. In the other feed stream one reactant is replaced by its labeled counterpart, i.e. $^{13}C^{16}O$ or $^{12}C^{18}O$ instead of $^{12}C^{16}O$, or D_2 instead of H_2. The synthesis gas is diluted with Ar in one feed stream or Ar plus Kr in the other feed stream.

3.1.2 Reactor Section

The reactor is a stainless steel tubular fixed bed reactor (I.D.=7.0 mm, bed length=20 mm), see Figure 28. It consists of a main body and two Swangelok fittings.

The catalyst bed typically consists of 0.2 - 0.3 grams of catalyst, diluted with 0.4 - 0.3 grams of SiC, both with a particle size range from 100 to 200 µm. The catalyst bed is held in place by two metal gauzes. Two mass-spectrometric sample lines are present, one upstream and one downstream the of catalyst bed. Sampling from the chambers is performed using stainless steel capillaries. For each sample chamber, two metal gauzes prevent particles from blocking the capillaries.

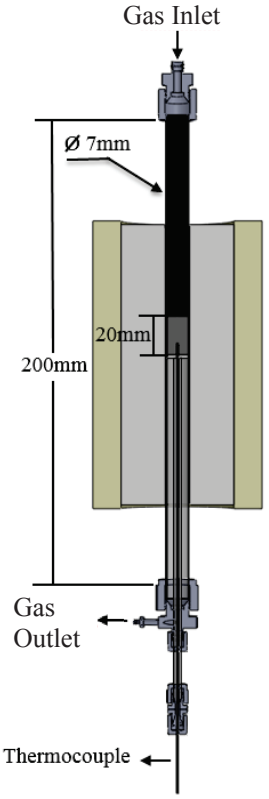

Figure 28: Schematic representation of the SSITKA reactor.

With a 3-way connection one of the two sample lines is linked to the mass-spectrometer. The sample is transferred to the mass-spectrometer. To prevent condensation of water and hydrocarbons, the capillaries are heated to 388 K. The reactor is heated by an electric conductivity oven to a maximum temperature of 773 K.

The axial catalyst bed temperature is monitored with a movable thermocouple, placed in the thermocouple tube (I.D.=1.0 mm) in the center of the reactor. At the applied reaction conditions, the axial temperature profile along the catalyst' bed could be considered isothermal (Figure 29). All product containing lines and valves are heated to 388 K**.**

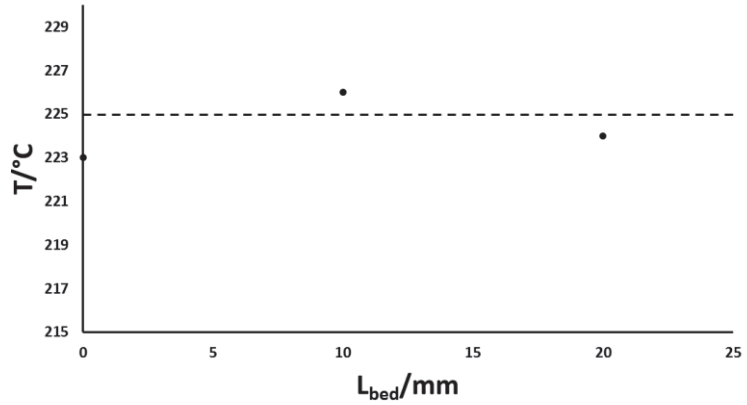

Figure 29: Temperature profile along catalyst's bed (L_{bed}) during reaction at T_{set}=225°C

A 4-way valve (Valco VICI) with a small internal volume (100 µl) realizes the fast switch between the two feed streams. It is electrically triggered and uses N_2 at 6 bar for the pneumatic switch of the valve. Needle valves are installed in the lines upstream of this valve and in the lines downstream of the reactor and towards the vent. The function of these needle valves is twofold:

• by means of the needle valves downstream the reactor and in the vent the reaction pressure of 1.2 bar is fixed;

• by means of the needle valves upstream of the 4-way valve the pressure drops for both feed configurations are equalized:

1. Left through the reactor and right towards the vent

2. Right through the reactor and left towards the vent

In both feed lines, a pressure gauze is installed to monitor any pressure changes due to the switching of the 4-way valve.

A characteristic Kr step change is shown in Figure 30, where the normalized Kr response goes from zero to unity in typically 4 s.

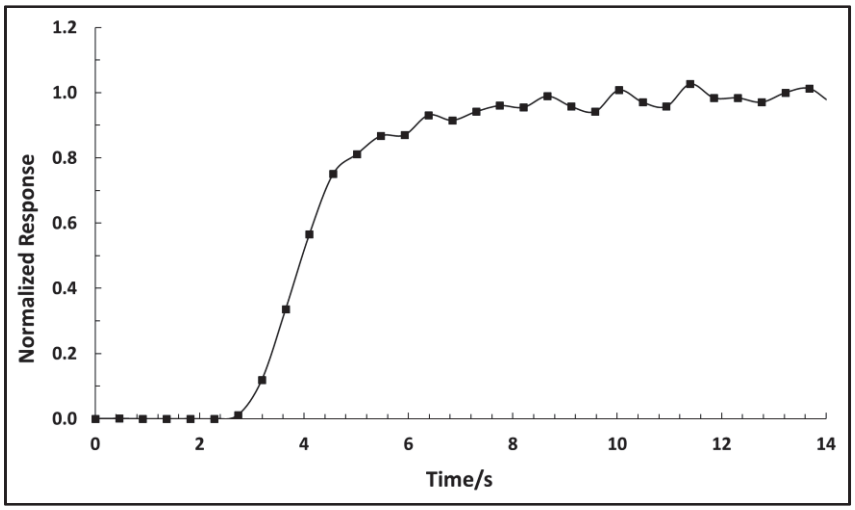

Figure 30: Typical normalized Kr transient response of a step change with a total flow rate of 100 Nml·min^{-1}

Axial temperature gradients in excess of 3 K were not measured. Moreover, the pressure drop over the catalyst bed is negligible. It is verified that all criteria for intrinsic kinetics [95], are met for all applied experimental conditions. Intrinsic kinetic conditions imply the absence of concentration and temperature gradients:

- In the catalyst pellets;
- Between the continuous gas phase and the pellet;
- In radial position in the catalyst bed.

3.2 Evaluation of transport phenomena

The details of the calculations are given in the Appendix 2.

3.2.1 External mass transport limitations

To make sure that the reaction rate is determined by catalytic reactions rather than by the diffusion of the reactants from the bulk to the external surface of the catalyst, Eq. 14 must be satisfied:

$$Ca = \frac{C_{A,bulk} - C_{A,surface}}{C_{A,bulk}} = \frac{R_{app}\, d_p}{6\ k_G\ C_{A,bulk}} < 0.05$$

Eq. 14

Where Ca is the Carberry number (dimensionless)

- C_A bulk is the concentration of reactant A in the bulk (mol m^{-3}_{gas})
- C_A surface is the concentration of A at the external surface of the catalyst (mol m^{-3}_{gas})
- R_{app} is the apparent rate of reaction per volume of catalyst (mol m^{-3}_{cat} s^{-1})
- d_p is the diameter of the spherical pellet (m)
- k_G is the external mass transfer coefficient (m s^{-1}) which can be calculated from the Sherwood number (Sh) in the range $0.1 < Re < 100$:

$$Sh = \frac{k_G\, d_p}{D_{A,mix}} = 2 + 1.8\, Re^{\frac{1}{2}}\, Sc^{\frac{1}{3}}$$

Both Reynolds number (Re) and the Schmidt number (Sc) can be calculated as follows:

$$Re = \frac{u_v\, \rho_G\, d_p}{\mu_G} \qquad Sc = \frac{\mu_G}{\rho_G\, D_{A,mix}}$$

Where

- $D_{A,mix}$ is the molecular diffusivity of A in the gas mixture (m^2 s^{-1})
- u_v is the superficial velocity (m s^{-1})

- ρ_G is the density of the gas mixture (kg m^{-3})
- μ_G is the viscosity of the gas mixture (kg m^{-1} s^{-1})

3.2.2 Internal mass transport limitation

To make sure that the reaction rate is not determined by the diffusion of the reactants from the external surface to the catalytic surface, the Weisz-Prater criterion must be respected (Eq. 15):

$$\omega = \left(\frac{d_p}{6}\right)^2 \frac{R_{app}}{D_{A,eff}\, C_{A,surface}} < 0.08$$

Eq. 15

Where ω is the Weisz modulus (dimensionless) and $D_{A,eff}$ is the effective diffusivity inside the pellet (m^2 s^{-1}) which can be calculated as follows:

$$\frac{1}{D_{A,eff}} = \frac{\tau_p}{\varepsilon_p}\left(\frac{1}{D_{A,mix}} + \frac{1}{D_{A,K}}\right)$$

Where ε_p refers to the pellet porosity (dimensionless) and τ_p to the pellet tortuosity (dimensionless). Knudsen diffusion coefficient ($D_{A,K}$) can be calculated from the following equations:

$$D_{A,K} = \frac{2}{3}\, r \sqrt{\frac{8\ R\ T}{\pi\ m_A}} \qquad r = 2\ \frac{\varepsilon_p}{\rho_p\ S_{int}}$$

Where

- r is the average pore radius of the pellet (m)
- R is the gas constant (J mol^{-1} K^{-1})
- T is the temperature of the gas mixture in the bulk (K)
- m_A is the molecular mass of A (kg mol^{-1})
- ρ_p is the pellet density (kg m^{-3}_{cat})
- S_{int} is the specific internal surface area of the pellet (m^2 g^{-1})

The Weisz modulus was preferred to the Thiele counterpart to estimate internal mass transport limitations. The Thiele modulus (φ) requires the knowledge of the intrinsic reaction rate while the Wiesz criterion is expressed in observable reaction rate term. These two parameters are

linked by the effectiveness factor (η) that relates the diffusive and intrinsic reaction rates (Eq. 16):

$$\omega = \eta * \phi^2$$

Eq. 16

3.2.3 External heat transfer limitation

The effects of heat transfer are analogous to those of mass transfer. Heat transfer limitations throughout the film surrounding the catalyst particle can be evaluated. The criterion for external maximum temperature difference ΔT_{film} over the film surrounding the spherical catalyst particles is expressed as follows:

$$\Delta T_{film} = \frac{R_{app}\,|\Delta H|\,d_p}{6\,\alpha_p} < \frac{0.05\,R\,T_G^2}{E_{app}}$$

Where

- ΔT_{film} is the temperature difference over the film surrounding the pellet (K)
- ΔH is the reaction enthalpy (J mol_A^{-1})
- E_{app} is the apparent activation energy of the reaction (J mol^{-1})
- α_p is the heat transfer coefficient between the pellet and the gas mixture (W m^{-2} K^{-1}):

$$\alpha_p = \frac{Nu\ \lambda_G}{d_p}$$

Where λ_G is the thermal conductivity of the gas mixture (W m^{-1} K^{-1}) and Nu is the Nusselt number which can be calculated in the range $0.1 < Re < 100$ as follows:

$$Nu = 2 + 1.8\,Re^{0.6}\,Pr^{\frac{1}{3}} \qquad Pr = \frac{C_{p,G}\,\mu_G}{\lambda_G}$$

Where Pr is the Prandtl number (dimensionless)

- $C_{p,G}$ is the heat capacity of the gas mixture (J kg^{-1} K^{-1})
- μ_G is the viscosity of the gas mixture (kg m^{-1} s^{-1})

3.2.4 Internal heat transfer limitation

Heat transfer limitations throughout the catalyst particle can also affect the reaction rate. The maximum temperature difference ΔT_{int} between the edge and the center of the particle is expressed as follows:

$$\Delta T_{int} = \frac{R_{app}\ |\Delta H|\ {d_p}^2}{60\ \lambda_p} < \frac{0.05\ R\ T^2}{E_{app}}$$

Where λ_P is the thermal conductivity of the catalyst particle (W m^{-1} K^{-1})

3.2.5 Radial heat transfer limitations

Radial heat transport from the near wall to the centerline of the bed can cause severe deviations from the isothermal operation. This transport is not limiting if the following criterion is valid:

$$\Delta T_{rad} = \frac{R_{app}\ |\Delta H|\ (1-\varepsilon_b)\ (1-b)\ {d_t}^2}{32\ \lambda_{r,eff}} < \frac{0.05\ R\ T_W^2}{E_{app}}$$

Where

ΔT_{rad} is the temperature difference between the bed near the wall and the bed center (K)

b is the volume of inert material as fraction of total solids volume (m^3_{inert} $m^{-3}_{inert+cat}$)

ε_b is the bed porosity (m^3_{void} m^{-3}_{bed})

$\lambda_{r\ eff}$ is the effective radial thermal conductivity in the bed (W m^{-1} K^{-1})

T_w is the temperature of the wall (K)

3.3 Analysis section and data treatment

The steady-state performance of the catalyst is monitored by on-line gas chromatography (GC), quantifying the C_1 to C_{10} product spectrum. On-line quadrupole mass spectrometry (MS) with gas sampling via heated capillaries is used to monitor the transient responses of the reactants and products having characteristic m/e values. All products other than methane do not possess characteristic m/e values and therefore cannot be monitored by on-line MS. The transient responses of the C_2 to C_4 hydrocarbons are therefore obtained on a gas chromatograph mass spectrometer (GCMS) equipped with a 16-loop sample valve. Each analysis is discussed in detail below.

3.3.1 MS Isotopic Composition Analysis

The composition of the light gases (H_2, H_2O, CH_4, CO, Kr, Ar) is directly given by the online INFICON® MS gas analyzer following the m/e value as listed in Table 9:

Table 9: Overview of the m/e values for the on-line MS analysis

Component			m/e value		
H_2	D_2		2	4	
Ar	Kr		40	84	
^{12}CO	^{13}CO	$C^{18}O$	28	29	30
CH_4	$^{13}CH_4$	CD_4	15	17	20
H_2O	$H_2{}^{18}O$	D_2O	18	20	24

The transient responses are normalized between the initial MS intensity before the isotopic step change and the final MS intensity at the moment in time when the unlabeled atom in all surface and gas phase species is replaced by its labeled counterpart.

Moreover all the MS signals are analyzed with respect to the Ar signal as internal reference, to compensate the MS drift.

With the MS is possible to analyze the evolution of relative isotopic composition during transient experiment (Figure 31).

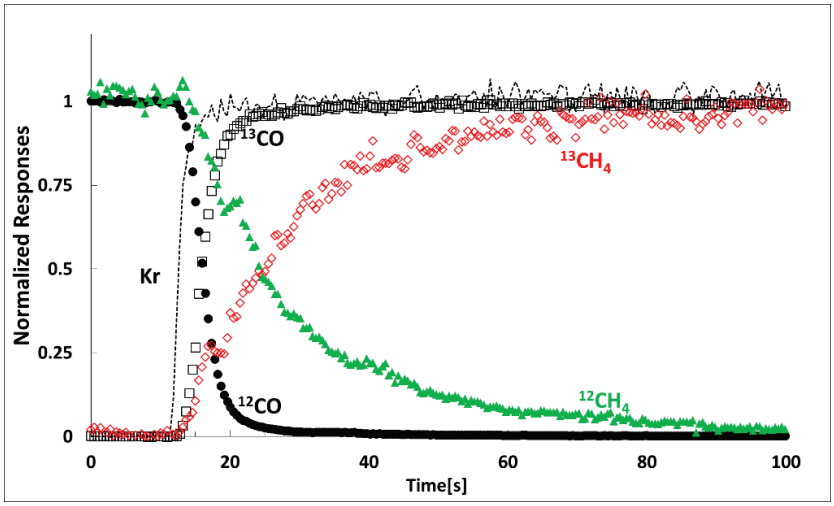

Figure 31: Normalized transient responses during a typical $^{12}CO \rightarrow ^{13}CO$ switch

The transient responses of methane in a D-labeling experiment cannot directly be obtained, because of overlap of the fragmentation patterns of (un)labelled methane and water molecules. For an adequate MS analysis of the methane transient, water needs to be eliminated.

To eliminate the water fragment contribution on all the D-labeled carbon species (CHD_3, CH_2D_2, CH_3D, CD_4) the reactor outlet stream is sent to a low-volume water trap. This trap is cooled to of 4°C by means of a bath of water and ice. The trap consists in a stainless steel tube with a d_i=3.2 cm placed inside a quartz tube with d_i=3.7 cm. This configuration allows to minimize the dead volume to avoid SSITKA signal's stretching.

3.3.2 On-line Gas-Chromatography-Mass-Spectrometry

A 16-loop valve is used for the sampling of the effluent (100 µL per loops) with a satisfying time resolution. The sampling rate at the beginning of the transient is high (≈ 1 Hz) and then decrease to lower values (<0.01 Hz for the last point, more than 500 s after the switch).

The products stored in the 16-loops valve are then injected into the GC/MS where they are separated and analyzed. Since no commercial software was available, special treatment routine using VBA for Excel has been developed. Starting from the GC/MS raw signal, each peak is detected and the MS signal is sampled at the apex.

The data treatment only focuses on the fragmentation pattern near the molecular peak (Mw) so that the local fragmentation is only due to C-H breakage [98]. In that region, all carbon atoms remain and it is assumed that no isotopic effect alters the C-H fragmentation. The observed deviation induced by $^{12}CO/^{13}CO$ replacement shifts the patterns to the right. At steady state (99% ^{12}CO, 1%^{13}CO) the signal of the fragment at m/z= M_{w+1} corresponds to $12C_{n-1}{}^{13}CH_{2n+2}$. Using the binomial law, the relative response of the molecular peaks can be easily calculated. The Table 10 reports these values for the 1-butene. At steady state, the contribution of the M_{w+k} fragments with k>1 can be neglected.

Table 10: Relative contributions of the molecular peak in the fragmentation pattern *Calculation are given for 1-butene (n=4) at steady state (99% ^{12}CO, 1% ^{13}CO)

	$^{12}C_nH_{2n}$	$^{12}C_{n-1}{}^{13}CH_{2n}$	$^{12}C_{n-2}{}^{13}C_2H_{2n}$	$^{12}C_{n-3}{}^{13}C_3H_{2n}$	$^{12}C_{n-k}{}^{13}C_kH_{2n}$	...	$^{13}C_nH_{2n}$
Molecular peak	M_w	M_w+1	M_w+2	M_w+3	M_w+k	...	M_w+n
*Relative contribution**	100	4.0	$6.3.10^{-2}$	3.10^{-6}	-	-	1.10^{-8}

From this, the fragmentation pattern of pure $^{12}C_nH_{2n}$ can be estimated based on simple calculation on steady state patterns with natural ^{13}C abundance:

$$I_{M_w} = {}^{12}I_{M_w} + {}^{13}I_{M_w}$$

$$I_{M_w+1} = {}^{13}I_{M_w+1}$$

$$I_{M_w} \gg I_{M_w+1}$$

$$\frac{{}^{13}I_{M_w+1}}{{}^{12}I_{M_w} + {}^{13}I_{M_w}} \approx \frac{I_{M_w+1}}{I_{M_w}}$$

With I_{Mw} the signal intensity of the molecular peak ($^{12}C_nH_{2n}$). I_{12Mw} and I_{13Mw} are the respective contribution of $^{12}C_nH_{2n}$ and $^{12}C_{n-1}{}^{13}CH_{2n}$ for I_{Mw}. Finally the $^{12}C_nH_{2n}$ can be expressed as a function of the observed pattern at steady state.

$$^{12}I_{M_w} \approx I_{M_w} \cdot \left(1 - \frac{I_{M_w+1}}{I_{M_w}}\right)$$

$$^{12}I_{M_w+1} = 0$$

With the same method, the whole $^{12}C_nH_{2n}$ pattern can be estimated:

$$^{12}I_{M_{w-i}} \approx I_{M_{w-i}} \cdot \left(1 - \frac{I_{M_w+1}}{I_{M_w}}\right)$$

An example of C-H fragmentation pattern near the molecular peak is given in Figure 32[98].

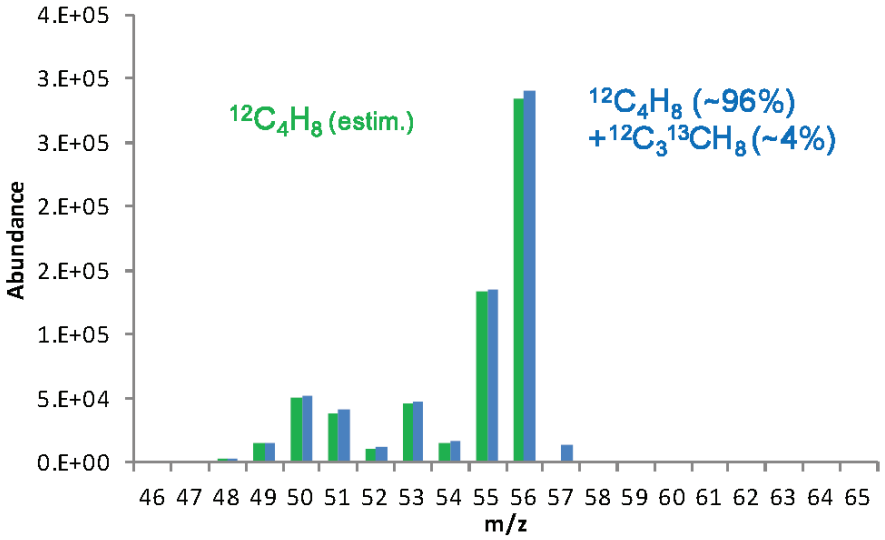

Figure 32: Example 1-butene MS C-H fragmentation pattern near the molecular peaks measured by GC/MS analysis.

For each compound, a MS fragmentation reference spectrum is measured from the analysis of the first loop with the natural $^{12}C/^{13}C$ abundance (approx ~99.0%/1.0%). Linear combination of the possibilities followed by the adjustment of all contributions allows the final relative isotopic composition of the compound for each peak of loop analyzed by GC/MS, of each transient. For a given experiment, the following sequence calls the minimization of the objective function:

$$f_{tr,l,id}(x) = \sum_{j=-7}^{n} \left(\sum_{i=0}^{n} \left(x_i \cdot {}^{12}I_{M_{w-i+j}} - I_{M_{w+j}} \right) \right)^2 \xrightarrow{x} min$$

The final determined isotopic distributions were consistent with the expected values at steady state and during the isotopic transient. Note that this determination does not require the exact knowledge of the $^{13}C/^{12}C$ abundance in the reactants. Some points have been manually discarded because of a high noise/signal ratio that prevent from adjusting the model.

Then, by repeating this treatment for each product of each sample analyzed by GC/MS the exhaustive isotopic composition of the effluent is determined.

Figure 33 reports the first points of the calculated normalized response for butane during an isotopic transient.

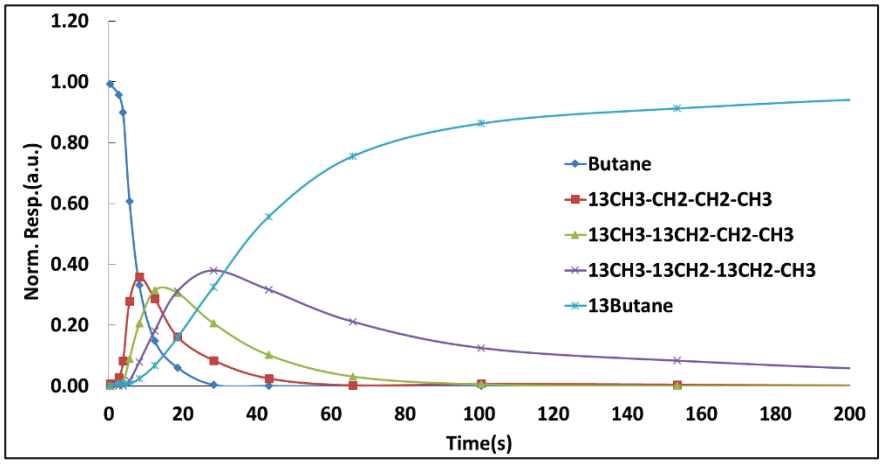

Figure 33: Example of GC-MS normalized response for 1-butene

Combining the GC/MS & MS analysis data with the GC/FID quantitative analysis gives the absolute quantification of the isotopic content.

3.3.3 On-line gas chromatogram

The online analysis system was composed of a cryogenic GC/FID-TCD HP 6890 with following features (Table 11):

Table 11: GC/FID-TCD HP 6890 specifications

Name	Specification
Capillary columns, PONA	100m*250µm*0.5µm
Column Flow	Constant
Carrier Gas	He
Inlet Pressure	37.13 psi
Initial Temperature	-60°C
Temperature Program	3°C/min from -60 to 0°C 4°C/min from 0 to 270°C

The combination of GC, GC-MS and MS techniques allowed monitoring the product distribution (paraffins, α- and β-olefins and isomers) and determining the isotopic composition of a large range of products during the transient (at least paraffin and α-olefins from C_1 to C_4). Quantitative analysis is made from C_1 to C_{13} with a good resolution for every isomer up to C_6. Because of the relatively low operating pressure (<3 bars) and low alpha values (<0.7) no heavy product was accumulated and products higher than C_{13} could be detected but hardly quantified. An overview of the GC separation is given in Figure 34 and shows that the peak purity up to C_7 is high enough to use the associated GC/MS fragmentation pattern. Most of the isomers are well separated and differentiate Parafins / Isoparafins, α-Olefins/Iso-α-Olefins, and β-Olefins/Iso-β-Olefins. For higher hydrocarbons, the quantifications are lumped.

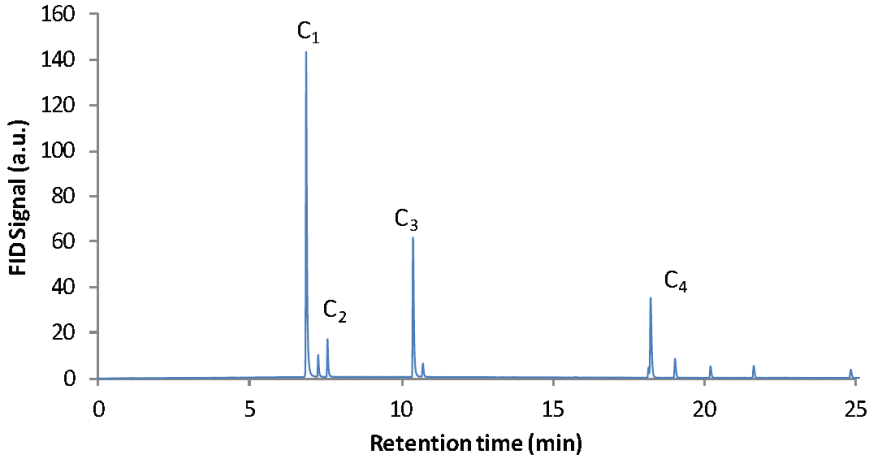

Figure 34: GC/FID separation of light products from methane to C_4

3.3.4 Conversion and selectivity

The standard deviation of the outlet CO concentration based on TCD is approximately 5% and does not accurately monitor the reaction at low CO conversion. The CO conversion was determined by using the method developed by Bell et al.[99] for low conversion (X_{CO}<10%) which considers the summation of all hydrocarbons based on the FID detector and provides the best accuracy for X_{CO}.

$$X_{CO} = \frac{Q_{out} \sum_{i=1}^{n} \nu_i C_i}{Q_{in} C_{CO}^{o}}$$

Eq. 17

Three main selectivities are defined:

$$S_{C_1}(\%) = \frac{C_1}{\sum_{i=1}^{7} \nu_i C_i}$$

Eq. 18

$$S_{C_2-C_4}(\%) = \frac{\sum_{i=2}^{4} \nu_i C_i}{\sum_{i=1}^{7} \nu_i C_i}$$

Eq. 19

$$S_{C_5-C_7}(\%) = \frac{\sum_{i\geq 5}^{7} \nu_i C_i}{\sum_{i=1}^{7} \nu_i C_i}$$

Eq. 20

with ν_i the number of carbon of the ith species with the molar concentration C_i. C_i is determined from the online FID/GC analysis and quantification. These selectivities refer to the global process without differentiating the olefins, paraffins or their isomers

Detailed selectivity can accurately be given up to C_7 for paraffins, olefins and isomers. Only global selectivity can be calculated for longer chain.

3.4 Experimental Procedure

3.4.1 Ni-based catalysts

Two Ni-based catalysts were tested (Table 12):

Table 12: Composition of Ni-based tested catalysts

Metal Load[w%]	Support
20%Ni	γ-Al_2O_3
10%Ni	SiC

The experimental procedure for both Ni-based catalysts is performed as follows:

1. All catalysts are activated in-situ by reduction in diluted H_2 (100 Nml·min^{-1}, 20 vol% H_2 in Ar). A high gas flow and a low heating rate of 1 °C·min^{-1} were chosen to avoid catalyst destruction by the release of excess amounts of H_2O formed during the reduction. The final activation temperature is held for 10 hours and is 500°C for both alumina and silicon carbide supported catalysts.

2. The catalyst is cooled to the reaction temperature under 100 Nml·min^{-1} of Ar.

3. Before starting the methanation synthesis an H_2 chemisorption step is performed with a total flow rate of 100 Nml·min^{-1}(60% H_2 and 40% He) for 20 minutes.

4. After step 3, the system is switched to methanation conditions keeping the same flowrate with the following composition: 60% H_2, 25% Ar and 15% ^{12}CO. The high flowrate helps to keep the CO conversion low, since the methanation reaction is highly exothermic and avoids temperature gradients. After the first 5 minutes during which the step transient responses are monitored, the catalyst is conditioned for at least 24 hours. For both Ni-based catalysts, the catalyst activity was monitored with only the quadrupole mass spectrometer because the CH_4 and H_2O are the most abundant products.

For the 20% Ni / γ-Al_2O_3 a fast deactivation (about 20% of the initial activity) occurs during the first minutes on stream and then a much slower deactivation at longer TOS. The average deactivation rates are ca 4%/h and 0.7%/h during the first 10h and at longer time on stream, respectively (Figure 35).

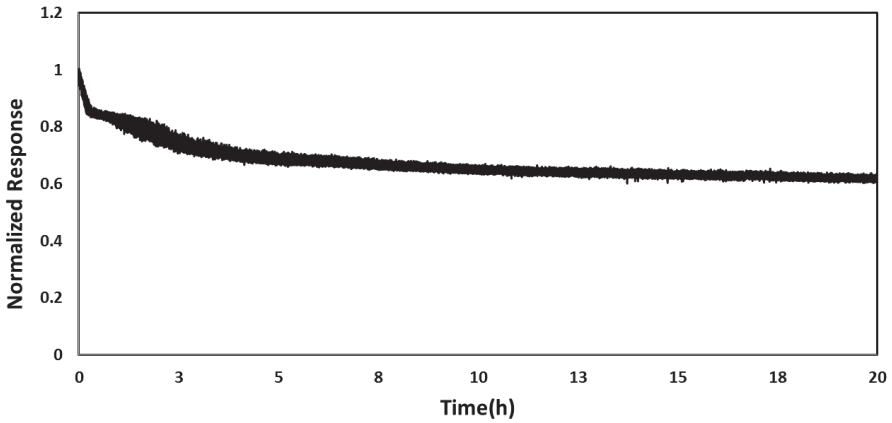

Figure 35: Changes in the methanation conversion with time on stream 20%Ni/γ-Al_2O_3 over 20 h of methanation reaction at 210 °C and H_2/CO = 4, starting from a freshly reduced catalyst.

From Figure 35 it is possible to notice that after 20 hours the catalysts is stable.

For the silicon carbide supported nickel catalyst the deactivation was higher, around 40% of initial value, and also in this case the catalyst was stable after 20h.

5. After the catalysts conditioning the SSITKA and step-transient switches were performed, the operating conditions are summarized in Table 13:

Table 13: Ni-based tested catalysts

$20\%Ni/Al_2O_3$										
Experiment	Operating conditions									
	T(°C)	P(bar)	Gas switch							
$^{12}CO \rightarrow {}^{13}CO$ SSITKA	210-250	1.2-1.6	Ar	H_2	CO	Ar	H_2	^{13}CO	Kr	
$H_2 \rightarrow D_2$ SSITKA	225	1.2-1.6	N_2	H_2	CO	N_2	D_2	CO	Kr	
$C^{16}O \rightarrow C^{18}O$ SSITKA	225-235	1.2-1.6	He	H_2	CO	He	H_2	$C^{18}O$	Kr	
Step-Transient	210-250	1.2-1.6	He	H_2		Ar	H_2	CO		
10%Ni/SiC										
Step-Transient	225	1.2-1.6	He	H_2		Ar	H_2	CO		

3.4.2 Co-based catalyst

The same protocol was used for the 15%Co/SiC catalyst with only few changes shown in Table 14:

Table 14: Operating condition for 15%Co/SiC

Catalyst	**In situ Reduction** **Total flowrate 20 Nml·min^{-1} (pure H_2)**		**Fischer Tropsch Reaction** **Total flowrate 50 Nml·min^{-1}**	
15%Co/SiC	Time[h]	T[°C]	Ar	40%
			H_2	40%
	16	450	^{12}CO	20%

Figure 36 shows how for the 15%Co/SiC a conditioning of at least 48h was necessary to assure the catalyst stability.

The temperature of 450°C and the dwell of 16h were chosen for the reduction conditions, based on magnetism measurements[100], that these conditions are enough to achieve at least 80% of reduction for a Co/Al_2O_3 catalyst.

For the 15%Co/SiC all the experiments were performed at H_2/CO equal to 2.

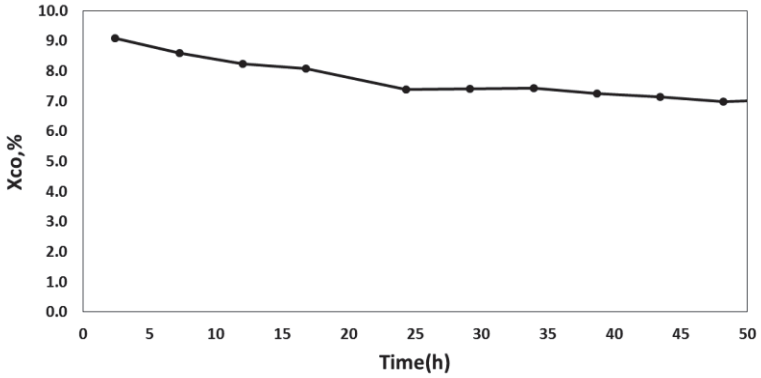

Figure 36: Changes in the CO conversion with time on stream 15%Co/SiC over 50 h of Fischer-Tropsch reaction at 225 °C and $H_2/CO = 2$, starting from a freshly reduced catalyst

3.5 Catalyst characterization

Catalyst characterization was carried out to identify the morphology of the catalyst. The studied samples are:

- 20%Ni/γ -Al_2O_3
- 10%Ni/SiC
- 15%Co/SiC

3.5.1 20%Ni/γ-A_2O_3

The specific surface areas of the 20%Ni/γ-Al_2O_3 was determined by nitrogen physisorption, at a temperature of 77K (-196°C), according to the Braun-Emmett-Teller (BET) method.

The samples were degassed in a pre-weighed sample tube under reduced pressure overnight at 120°C. The sample tube was re-weighed to obtain the mass for the degassed sample. BET surface area (m^2/g)

measurements were collected at 77 K by N_2 on a BELSORP-miniII (Figure 37) made by BEL Japan, Inc instrument (BelJapan).

Figure 37: BELSORP-miniII BET equipment

The value found for the surface area of 20%Ni/γ-Al_2O_3 is 101±5 m^2/g.

The Ni-metal dispersion of the 20%Ni/γ-Al_2O_3 was determined via two techniques: H_2 chemisorption and TEM analysis.

H_2 chemisorption measurements were performed after a reduction step at 500°C for 10h. The chemisorption operating conditions are listed in Table 15:

Table 15: Operating condition for H_2 chemisorption over 20%Ni/γ-Al_2O_3

Process		H_2 Chemisorption		
m_{cat}[mg]		200		
P[bar]		1.2		
T[°C]		200	250	300
Flow[mL/min]	Ar	80		
	N_2	10		
	H_2	10		

The experiments were performed at three different temperatures, the results are shown in Table 16:

Table 16: Results from dynamic hydrogen adsorption experiments over 20%Ni/γ-Al_2O_3

Temperature, °C	Amount of H adsorbed (mol/kg_{cat})
200	0.63
250	0.37
300	0.40

This time nitrogen was used as a tracer and by means of a Langmuir-Hinshelwood model to fit data, it was possible to estimate the number of surface active sites (Figure 38).

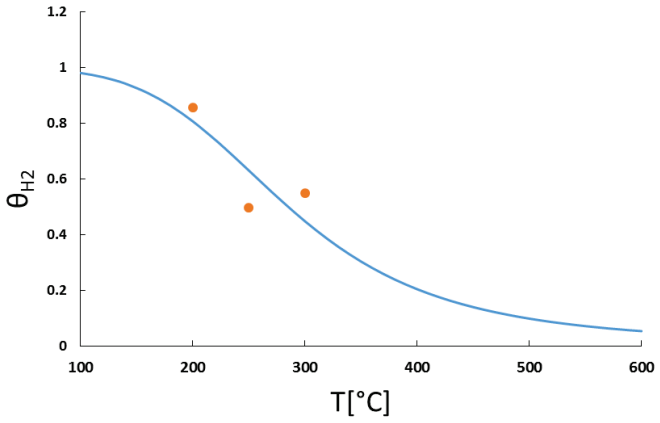

Figure 38: H_2 dynamic adsorption data
Dots: experimental points, Line: Langmuir-Hinshelwood Model fit

As expected, the amount of adsorbed atomic H decreases with the increasing temperature. However, the value of hydrogen coverage θ_{H2} is almost the same at 250°C and 300°C.

Transmission Electron Microscopy (TEM) images were also collected for the 20%Ni/γ-Al_2O_3.

Figure 39 shows the effect of methanation reaction over 20%Ni/γ-Al_2O_3

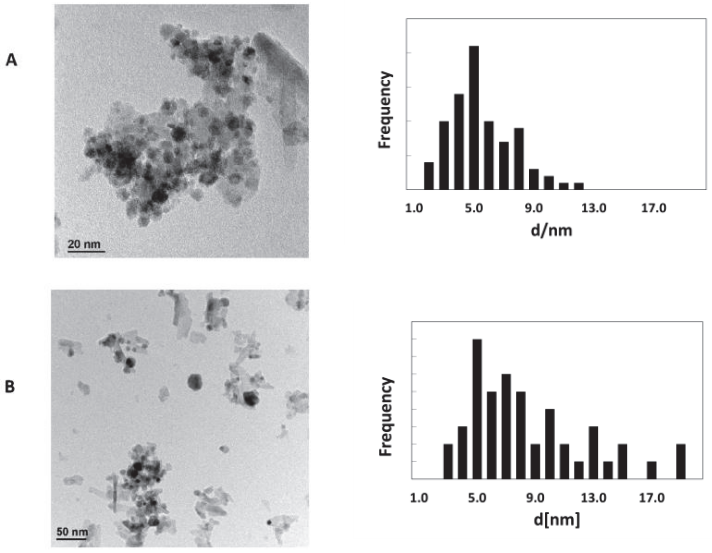

Figure 39: TEM images and particle distribution of A/freshly reduced 20%Ni/γ-Al_2O_3 catalyst and B/used catalyst after about 24 h on stream

Two main ageing phenomena are known to affect Ni based methanation catalysts: Ni particle sintering and carbon deposition [77,103,104]. The changes in nickel dispersion can be assigned to a Ni particle sintering process occurring by means of Ni tetra-carbonyl formation, favored on small particles, transportation through the catalyst bed, then recombination on larger particles [105].

For the 20%Ni/γ-Al_2O_3 such a sintering process can be considered as minor since the metal dispersion decreased only from 18.6% (freshly reduced sample/A) to 16.8% (long term reacted sample/B). The dispersion value determined after long term ageing period will be considered for the intrinsic activity calculation.

The calculation of the dispersion values were performed through the Eq. 21[101]:

$$D = 6\frac{(v_m/a_m)}{d_{VA}}$$

Eq. 21

Where d_{va} is the mean particle size obtained from microscopy images.

v_m[Å^3] and a_m[Å^2] that are respectively the volume occupied by an atom in bulk metal and the area occupied by a surface atom are well known in literature for several metals atoms.

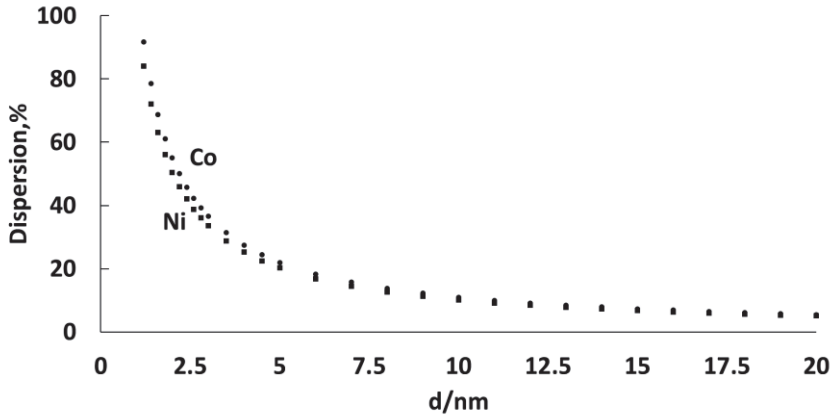

Figure 40: Plot of dispersion D as a function of mean diameter d_{VA} for nickel and cobalt [101]

From the metal dispersion value it is possible to calculate the amount of surface active site for the 20%Ni/γ-Al_2O_3 that results to be 0.68 mol/kg_{cat}.

3.5.2 10%Ni/SiC

The characterization for the 10%Ni/SiC was performed by specific surface area measurements and electron microscopy analysis.

The B.E.T. method lead to specific surface area of 30 m^2/g.

The TEM analysis was performed over a reduced catalyst, again at 500°C for 10h (Figure 41).

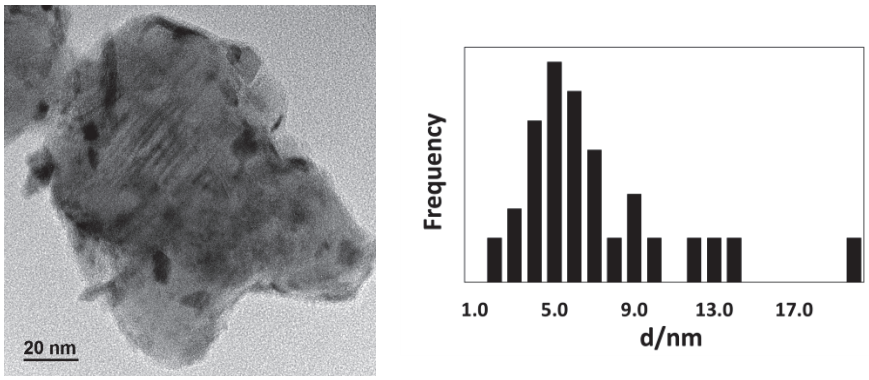

Figure 41: TEM images and particle distribution of a reduced 10%Ni/SiC

From TEM analysis an average particle diameter of 5.7±0.3 nm was estimated. This bring to a dispersion value of 17.7% calculated using Eq. 21.

3.5.3 15%Co/SiC

Over 15%Co/SiC, carbon monoxide chemisorption experiments were carried out with an in-house setup following a similar protocol as described by Couble and Bianchi[25,102]. After the direct reduction of 300 mg of catalyst at 450°C for 16 h and the cooling to 150°C under H_2, the reactor is flushed with an inert gas (Ar). Then the feed is abruptly switched to a mixture of argon, carbon monoxide and krypton as tracer (Table 17).

Table 17: Operating condition for Co chemisorption over 15%Co/SiC

Process		CO Chemisorption
m_{cat}[mg]		300
P[bar]		1.2
T[°C]		150
Flow[mL/min]	Ar	15
	Kr	5
	CO	5

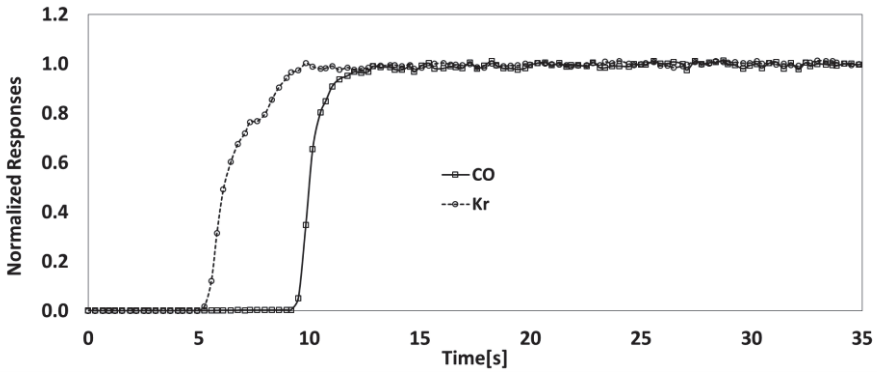

Figure 42: Breakthrough curves observed during dynamic adsorption of CO

As expected Kr comes out first followed by the CO delayed by approximately 5 seconds. As the krypton does not adsorb on the catalysts and the partial pressure of krypton is the same as the partial pressure of CO, the difference between the krypton and carbon monoxide response corresponds to the amount of adsorbed CO as a

function of time. It is assumed that one CO molecule adsorbs on one cobalt atom.

For the 15%Co/SiC the Co adsorption measurements have been performed over the reduced sample and after several hours of reaction.

B.E.T. specific surface measurement was also performed over the 15%Co/SiC and the value found is 17 m²/g.

3.6 Conclusions

The results of the characterizations for the three catalysts are shown in Table 18:

Table 18: Characterization results over tested catalysts.
+ Estimated by H_2 chemisorption, *Estimated by CO chemisorption

Catalyst	Specific Surface Area (m^2/g)	Average diameter (nm)	Dispersion, %		Surface active site ($mol_{Me}/kgcat$)	
			Chem.	TEM	Chem.	TEM
20%Ni/γ-Al_2O_3	101±0.5	5.4±0.5	**20**$^+$	18.6	**0.68**$^+$	0.63
10%Ni/SiC	30±0.5	5.7±0.5	-	**17.7**	-	**0.3**
15%Co/SiC	17±0.5	10	**7***	-	**0.18***	-

The values in bold represent the calculated and used values of the surface active site for each catalysts. In chapter 4 these value are used to normalize the experimental amount of surface species and the steady-state reaction rate to calculate the coverage of surface species and TOF for each tested catalyst.

A complete characterization was performed only for the 20%Ni/γ-Al_2O_3.

This catalyst was chosen as reference catalysts so a complete lot of experiments were performed with the 20%Ni/Al_2O_3, the results were later used to develop a microkinetic model to elucidate the CH_4 production.

The 10%Ni/SiC was studied moreover to look at the role of support during the methanation reaction, while the 15%Co/SiC was

investigated to extend the analysis of methane production to typical Fischer-Tropsch conditions.

Chapter 4

Results

This chapter reports on the experimental results obtained from SSITKA and step-transient experiment, over both nickel and cobalt based catalysts.

4.1 Introduction

The aim of this chapter is to obtain insight into the CH_4 formation mechanism during methanation and Fischer-Tropsch reaction by the quantification of the conversion and selectivity at steady state and during isotopic and step-transient experiments.

The results will be shown in the following order:

1. 20%Ni/γ-Al_2O_3: as reference catalyst, a complete set of SSITKA experiments were performed involving ^{13}C, D_2 and ^{18}O as labeled atoms. Moreover, step-transient experiments were performed to get further mechanistic information about the CH_4 and H_2O formation step.
2. 10%Ni/SiC: step-transient experiments were performed to study the role that support plays during methanation reaction, underlining especially the interaction between support and reaction products like CH_4 and H_2O.
3. 15%Co/SiC: to compare the CH_4 and H_2O formation mechanisms during Fischer-Tropsch reaction, SSITKA experiments involving ^{13}C and ^{18}O and step-transient were performed and analyzed.

4.2 20%Ni/γ-Al_2O_3

4.2.1 Steady state CO conversion

The steady state performance of 20%Ni/γ-Al_2O_3 was determined at three temperatures: 210, 225 and 250°C after 24 h of catalyst conditioning for 200 mg of sample. The operating condition are summarized in Table 13.

The experimental protocol for the SSITKA and step-transient experiments have been described in detail in section 3.4, chapter 3.

Only traces of ethane, propane and carbon dioxide were analyzed at all temperatures over 20%Ni/γ-Al_2O_3. Thus methane is considered the only carbon containing product of the methanation reaction.

At this operating condition and steady-state X_{CO} value, no heat and mass-transfer limitation were notice (see Appendix 2).

Plotting the CO catalyst activity (the CO conversion was always below 11%) on an Arrhenius plot, it is possible to estimate an apparent activation energy of 75 kJ/mol. This value matches the range of apparent activation energies reported in the literature. Vannice [106] found from experimental tests a value for the apparent activation energy of 105 kJ/mol and reports a wide value range in literature from 65 to 109 kJ/mol[107,108,109,110].

Table 19 shows the rate of CO consumption measured in the temperature range of 210-250°C and the relative turnover frequencies:

Table 19: Rate of CO consumption and TOF_{co} at 210, 225 and 250°C with H_2/CO=4, Total flow=100 mL/min (25 Ar/60 H_2/15 CO)

T (°C)	r_{co} (μmol/s)	TOF_{co} (mol_{co} mol_{Ni}^{-1} s^{-1}) x 10^{-3}
210	0.28	1.9
225	0.49	3.4
250	1.1	7.8

The TOF_{co} increases with temperature from 1.9 ·10^{-3} s^{-1} to 7.8 ·10^{-3} s^{-1}. Vannice[106] has reported for different Ni/Al_2O_3 catalyst values for the TOF_{co} between 0.67·10^{-3} and 3.8·10^{-3} at 205°C.

Figure 43 shows a comparison of methanation activity results between this study and the study of Sehested and coworkers[111].

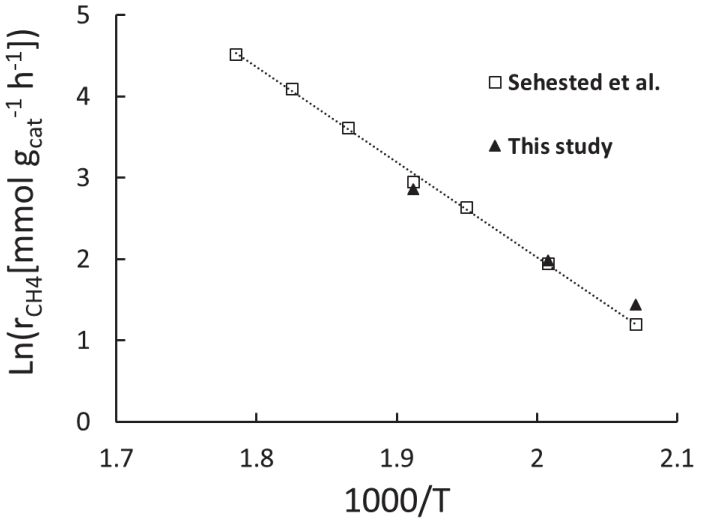

Figure 43: Comparison between Sehested [111] and the present work

Fitting the activity points with an Arrhenius model, Sehested found a value for the activation energy of 96.7 kJ/mol, reasonably close to our value of 75 kJ/mol.

4.2.2 ^{13}C-labeling of CO and CH_4

Figure 44 and Figure 45 show the responses of CO and CH_4 during a ^{13}C-labeling experiment.

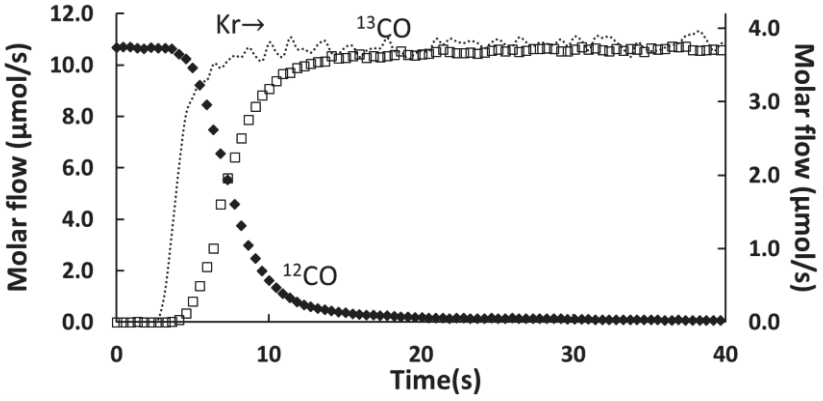

Figure 44: Molar flows of Kr, ^{13}CO, and ^{12}CO on the 20%Ni/γ-Al_2O_3 catalyst at H_2/CO=4 and T=225°C,
Total flow=100 mL/min (25 Ar/60 H_2/15 CO→20 Ar/5 Kr/60 H_2/15 CO)

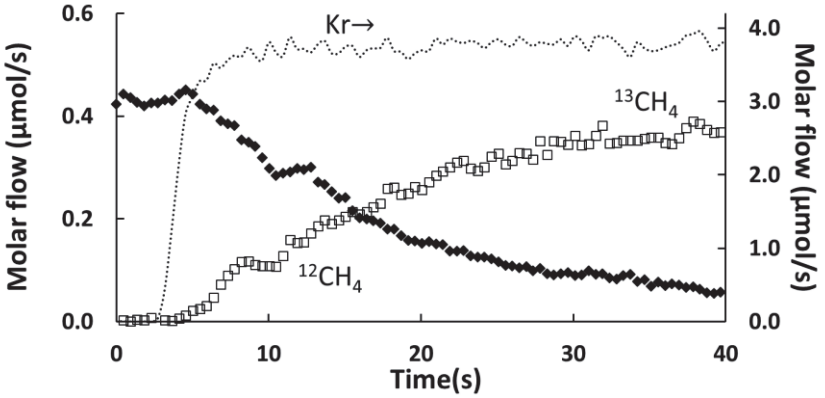

Figure 45: Molar flows of Kr, $^{13}CH_4$, and $^{12}CH_4$ on the 20%Ni/γ-Al_2O_3 catalyst at H_2/CO=4 and T=225°C,
Total flow=100 mL/min (25 Ar/60 H_2/15 CO→20 Ar/5 Kr/60 H_2/15 CO)

The following observations are made:

I. The Kr transient increase from zero to the unity in about 8 seconds.

II. The ^{13}CO response is fast. It is delayed in time with respect to the Kr transient. This implies the presence of a time period in which no breakthrough of ^{13}CO is observed, this is due to a strong adsorption of CO on the nickel. Moreover, the ^{12}CO transient is the inverse of the ^{13}CO response, as observed in Figure 44. The ^{12}CO and the ^{13}CO are symmetric during the labeling, indicating the absence of a kinetic isotopic effect.

III. The $^{13}CH_4$ transient is slower than the ^{13}CO transient and start at same time as the ^{13}CO response.

4.2.3 Estimation of surface intermediates amounts based on mean surface residence times

As mentioned in chapter 2, via the SSITKA transient it is possible to quantify directly the amounts of adsorbed species on catalyst surface.

It must be stressed that these estimates are not related to any assumptions about the reaction mechanism and a ^{13}C-labeling experiment only provides information about the reactivity of C-containing pools.

By applying Eq. 6 to the normalized responses of ^{13}CO and $^{13}CH_4$, is possible to estimate the mean surface residence time for adsorbed CO and C_1 adsorbed intermediates leading to methane.

Once the τ_{CO} and τ_{C1} are estimated, the amounts of the corresponding species adsorbed on surface are calculated according to Eq. 7 [47]:

$$N_{CO} = \frac{\tau_{CO}\, F_{CO}}{W_{cat}} = \frac{F_{CO}}{W_{cat}} \int_{t=0}^{\infty} \left(E_{Kr}(t) - E_{13_{CO}}(t)\right) dt$$

Eq. 22

Where

N_{CO} is the amount of CO_{ads} in $mol \cdot kg_{cat}^{-1}$;

F_{CO} is the molar feed rate of CO in $mol \cdot s^{-1}$;

τ_{CO} is the mean surface residence time of CO_{ads} in s;

E_{13CO} is the normalized transient of ^{13}CO;

E_{Kr} is the normalized transient of Kr, representing the gas-phase holdup in the reactor.

Since the methane is the only carbon containing product for the 20%Ni/γ-Al_2O_3, the methane intermediates are the only carbon species adsorbed on surface and its abundance is calculated by Eq. 23:

$$N_{C_1} = \frac{\tau_{C_1}\, F_{CO}\, X_{CO}}{W_{cat}} = \frac{F_{CO}\ X_{CO}}{W_{cat}} \int_{t=0}^{\infty} \left(E_{Kr}(t) - E_{13_{CH_4}}(t)\right) dt$$

Eq. 23

Where

X_{CO} is the conversion of CO and N_{C1} is the amounts of $C/CH_{x,ads}$ in $mol \cdot kg_{cat}^{-1}$.

Table 20: Surface amounts and coverages of CO_{ads} and $C_{1,ads}$ based on the integration of the transients, N_s=0.68 $mol_{Ni} \cdot kg_{cat}^{-1}$

T(°C)	X_{CO}(%)	$\tau_{CO}(s)$	$\tau_{C_1}(s)$	$N_{CO}\left(\frac{mol}{kg_{cat}}\right)$	$N_{C_1}\left(\frac{mol}{kg_{cat}}\right)$	θ_{CO}	θ_{C_1}
210	3	7.6	94	0.38	0.11	0.56	0.17
225	5	6.5	67	0.26	0.18	0.39	0.26
250	10	4.4	28	0.21	0.16	0.31	0.23

Table 20 shows the result of the calculations from the isotopic transient data. Coverages θ_{CO} and θ_{C1} are calculated considering the number of active sites based on H_2 chemisorption.

This number indicated as N_s and is equal to 0.68 $mol_{Ni} \cdot kg_{cat}^{-1}$.

The values in Table 20 are consistent with the values shown by Khodakov et al.[112] at 250°C. They performed a SSITKA experiment of methanation reaction over a 9.5%Ni/γ-Al_2O_3 at 250°C with a H_2/CO ratio of 3 and a steady-state conversion of 13.8%, slightly higher than our value at 250°C.

Under these condition they found a surface coverage of CO (θ_{CO}) and CH_x intermediates leading to methane (θ_{C1}) respectively of 0.28 and 0.23, in good agreement with our value.

As mentioned in chapter 2, plotting the decay of ^{12}C for the methane on a semi-logarithmic plot can give information on the reactivity of species leading to CH_4. The shape of this decay curve bears information on the mechanism [113].

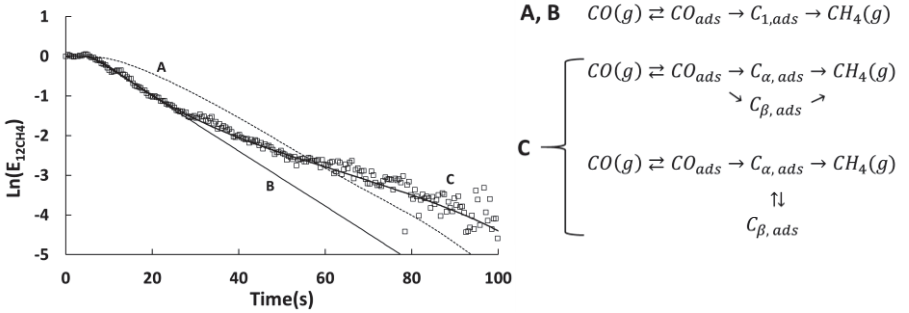

Figure 46: Left: Semi-logarithmic plot of decay of ^{12}C for the methane, T=225°C and $H_2/CO=4$. Right: Different fundamental mechanisms for the methanation reaction

As Figure 46 (Left) shows, the experimental methane production (□) does not follow a single route mechanism, but is characterized by two reacting intermediates in parallel preceded by another surface species represented by the reversibly adsorbed CO*. This behavior has frequently been observed in literature for the CO hydrogenation over different methanation and Fischer-Tropsch catalysts[47,48,114]. The curves A and B could be described with a first pool represented by the reversible adsorption of CO and then a single C_1 adsorbed intermediate leading to methane (Figure 46: Right). A different reaction rate of the C_1 pool justify the different behaviors of curve A and B.

Several reactive intermediate C-species have been identified by different techniques, however, as was discussed in section 1.3.4 and 1.3.5, there is still no consensus about the chemical identity of these reactive intermediate species. Modeling in Chapter 5 allow us to go further in the identification of the nature for the surface intermediates leading to methane.

These results are obtained by ^{13}C-labeling, so only the reactivity of ^{13}C-pools is involved. For this reason also D-labeling and O-labeling experiments were performed over the 20%Ni/γ-Al_2O_3, to try to elucidate the reactivity of all the intermediate species adsorbed on the surface.

4.2.4 D-labeling on methanation reaction

To study hydrogen reactivity during methanation reaction over 20%Ni/γ-Al_2O_3 a $H_2 \rightarrow D_2$ SSITKA experiment was carried out.

The switch consisted of:

$$\mathbf{N_2/CO/H_2 \rightarrow N_2/Kr/CO/D_2}$$

This time nitrogen was used instead of argon as inert diluent, due to the overlap of fragment 20 m/e of argon with the deuteromethane CD_4 (see Table 9).

All the m/e fragments set to follow a D-labeling experiment are summarized in section 3.3.1.

To avoid the overlap of H_2O and D_2O MS signals (Table 9) a water trap was set at the outlet of the reactor to remove water (section 3.3.1). Removing all the produced H_2O and D_2O before the MS means that all the information about the water production is lost during the H_2/D_2 isotopic switch.

Figure 47 and Figure 48 show the typical transient responses using deuterium as isotopic tracer:

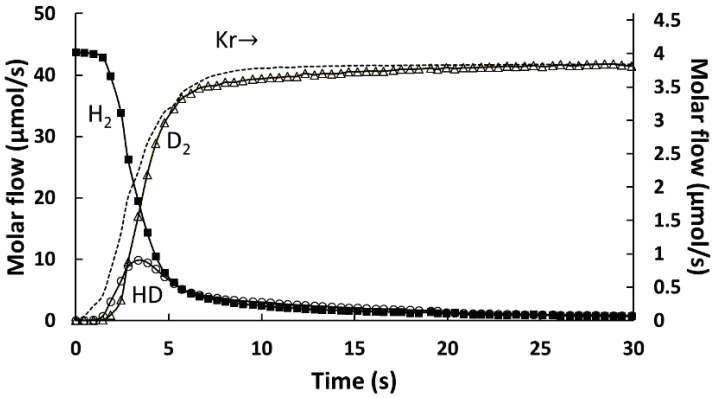

Figure 47: Molar flows of H_2, D_2, HD and Kr, T=225°C, P=1.2bar and H_2/CO=4, Xco=5.8%
Total flow=100 mL/min (25 N_2/60 H_2/15 CO→20 N_2/5 Kr/60 D_2/15 CO)

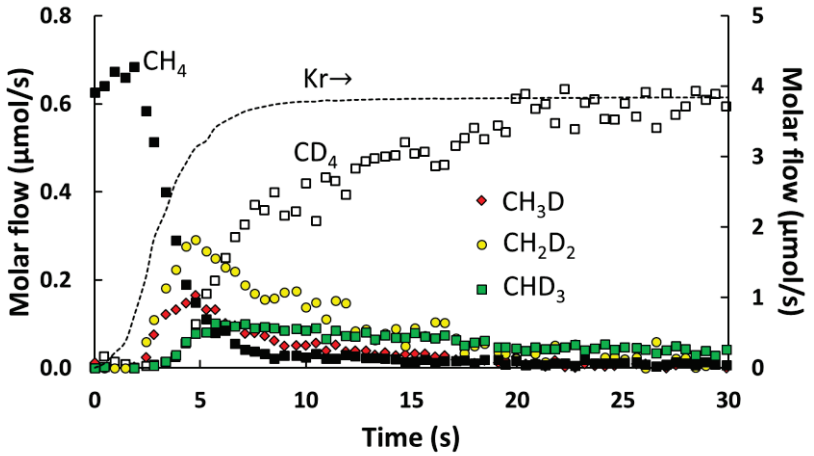

Figure 48: Molar flows of H_2, D_2, HD and Kr, T=225°C, P=1.2bar and H_2/CO=4

The H_2/D_2 SSITKA transient is fast compared to the ^{13}C-labeling. The integration of deuterium curves has to be corrected from the tailing behavior that is also present on the H_2 response.

Table 21: Surface amounts and coverages of $D_{2,ads}$ and $C_{1,ads}$ based on the integration of the transients, N_s=0.68 $mol_{Ni} \cdot kg_{cat}^{-1}$

T(°C)	X_{CO}(%)	$\tau_{D_2}(s)$	$\tau_{CD_4}(s)$	$N_{D_2}\left(\frac{mol}{kg_{cat}}\right)$	$N_{CD_4}\left(\frac{mol}{kg_{cat}}\right)$	θ_{D_2}	θ_{CD_4}
225	r_{H_2}: 5.8 r_{D_2}: 6.9 $r_{H_2}/r_{D_2} = 0.84$	0.44	20	0.092	0.075	0.16	0.11

Table 21 shows the quantification of H_2/D_2 isotopic switch. The experiment was performed only at 225°C and the coverage found for the CD_4 product was lower than the value estimated at same operating condition of ^{13}C-labeling. Due to the different technical limits during a H_2/D_2 (i.e. MS signal tail, inverse kinetic isotopic effect), the value of θ_{D2} shown in Table 21 is not sufficiently accurate, and is only reported to indicate the extent of the H/D surface coverage.

During the H_2/D_2 isotopic switch an inverse kinetic isotopic effect was detected (see 2.1.1). This effect is already reported in literature for several catalyst, Table 22:

Table 22: Comparison of inverse kinetic isotopic effect value present in literature

Catalyst	T(°C)	r_{H_2}/r_{D_2}	Reference
20%Ni/γ-Al_2O_3	225	0.84	This study
Ni/α- Al_2O_3	203	0.77	[115]
Co and Fe-based catalysts	235	0.7-0.82	[116]
20%Co/Al_2O_3	210	0.77-0.78	[50,51]

During the D-labeling experiment it is possible to follow the formation of all the intermediates species leading to methane until they are deuterated to CD_4.

Figure 48 shows the formation of all the deutered species CD_xH_{4-x} where x=0-4. Once the transient is started the first signal observed is that of CH_2D_2, with CH_3D appearing at almost the same time, followed by CHD_3, and finally CD_4.

The CH_2D_2 signal shows the highest intensity, coupled with the species distribution described above, suggesting that the CH_2* species is the most abundant reacting intermediate species leading to methane.

Osawa[117] and coworkers performed H/D exchange of methane on nickel surface by means of CH_4 pulses under a continuous flow of He and D_2 at T=300-400°C. They found the $CH_{4-x}D_x$ product distribution shown in Figure 49 A.

Figure 49 B shows the $CH_{4-x}D_x$ product distribution obtained by Màrquez-Alvarez et al.[118] over Ni/SiO_2 during a H_2/D_2 SSITKA experiment at 250°C.

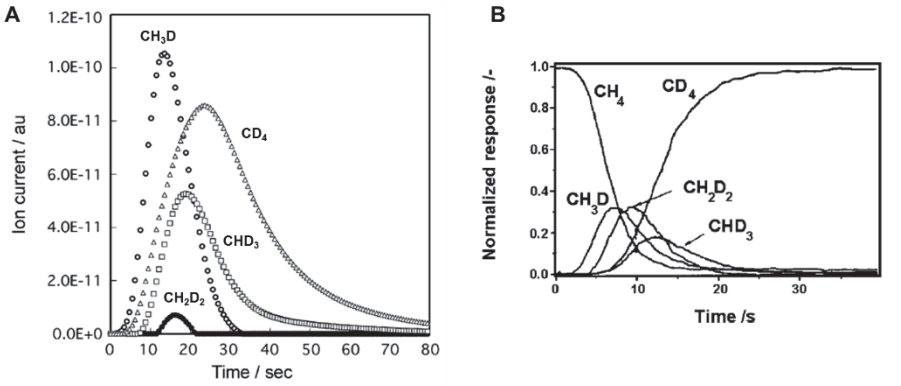

Figure 49: $CH_{4-x}D_x$ product distribution during D-labeling experiments, A)[117], B)[118]

Both studies found similar deuterated product distributions, but the behavior is different than the experimental distribution obtained in this work.

As for the ^{13}C-labeling, plotting on a semi-logarithmic plot the decay of the H content for the methane it is possible to unravel how many H pools participates to the methane formation (Figure 50).

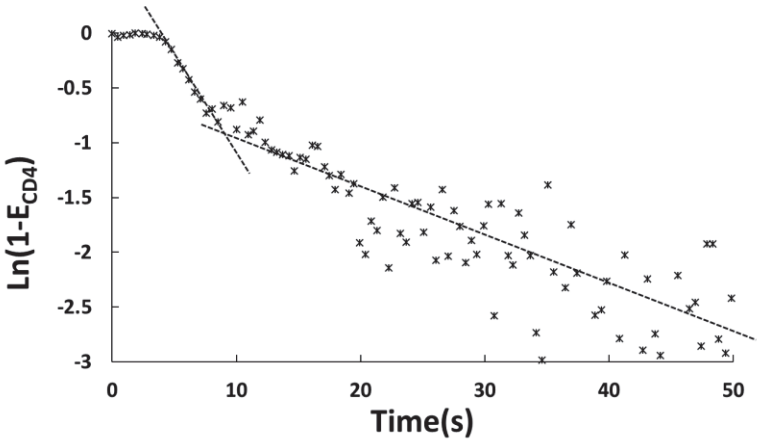

Figure 50: Semi-logarithmic plot of decay of H for the methane, T=225°C Notice that $E_{CH4}=1-E_{CD4}$

Clearly two different H reacting pools participate to the methane production. The first fast pool is dominating in the first 10 seconds while a second slowly reacting pool is responsible for the rest of the CD_4 production.

Again we can interpret the experimental results (H_2/D_2 SSITKA) that there are also in the case of H/D two reacting intermediates pool, in a parallel configuration, responsible for the CH_4 production. A possible schematic representation of the reacting pathway of the H/D pools could be:

$$D_2(g) \rightleftarrows 2\,D^* + CO^* \begin{matrix} \nearrow\ C_{\alpha,\,ads} + D^* \searrow \\ \searrow\ C_{\beta,\,ads} + D^* \nearrow \end{matrix} CH_{4-x}D_x(g)$$

Figure 51: Possible mechanism for the methanation reaction involving H/D reacting species

4.2.5 O-labeling on H_2O production

The kinetics of water formation was also studied by a He/$C^{16}O$/H_2→ He/Kr/$C^{18}O$/H_2 isotopic step change experiment. In the ^{18}O-labeling experiments, only transients for O-containing species are obtained.

Figure 52 shows the transient responses for Kr and CO.

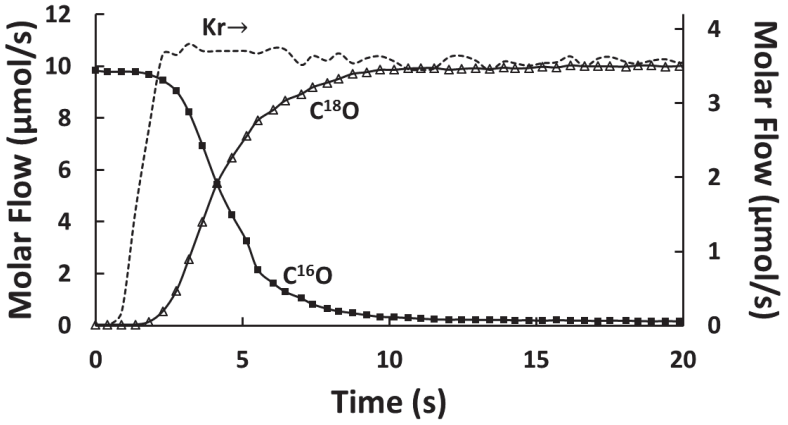

Figure 52: Molar flows of Kr, $C^{16}O$, and $C^{18}O$ on the 20%Ni/γ-Al_2O_3 catalyst at H_2/CO=4 and T=235°C, Xco=8%
Total flow=100 mL/min (25 He/60 H_2/15 $C^{18}O$→20 He/5 Kr/60 H_2/15 $C^{18}O$)

The experiment is performed at 235°C and over m_{cat}=0.100 g to minimize H_2O adsorption. This reaction temperature leads to a slight higher CO conversion of 8%.

As for the ^{13}C-labeling experiment, the ^{18}O-labeling shows a symmetry for the $C^{16}O$ and $C^{18}O$ indicating an absence of a kinetic effect on the reaction rate during the switch.

The transient for $H_2{}^{16}O$ and $H_2{}^{18}O$ shows slow kinetics, a significant amount of $H_2{}^{16}O$ is still present after 200 s. Described similar observation was made by Holmen and Yang[51] over $Co/\gamma\text{-}Al_2O_3$.

It is possible that H_2O formation is slow on nickel, but preliminary step-transient results showed a relevant effect of the support on the H_2O formation.

Therefore it is likely that H_2O interacts with the alumina support.

To further validate this hypothesis, transient experiments over different supports have been carried out and will be presented later in this chapter.

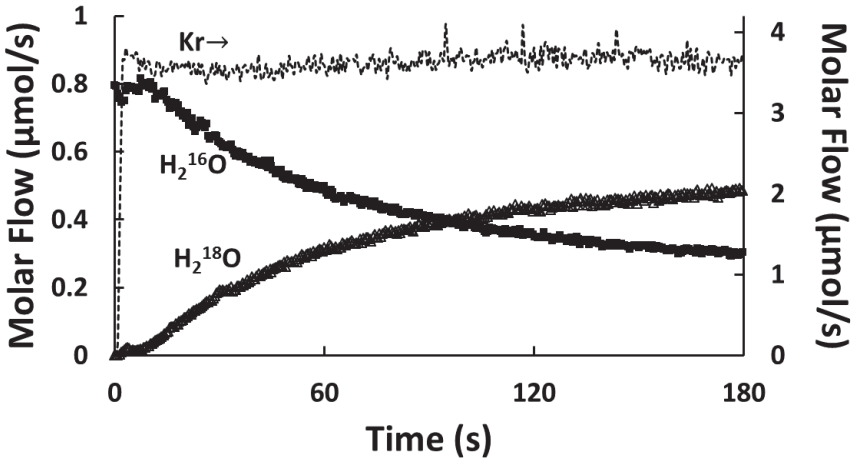

Figure 53: Molar flows of Kr, $H_2{}^{16}O$, and $H_2{}^{18}O$ on the $20\%Ni/\gamma\text{-}Al_2O_3$ catalyst at $H_2/CO=4$ and T=235°C, Xco=8%
Total flow=100 mL/min (25 He/60 H_2/15 $C^{18}O$→20 He/5 Kr/60 H_2/15 $C^{18}O$)

Figure 53 shows how after even 180 s the $H_2{}^{18}O$ does not reach the steady-state value for the water production.

Plotting the decay of ^{16}O content in the water on a semi-logarithmic plot, it is possible to notice that the water production is described by a single type reactivity behavior.

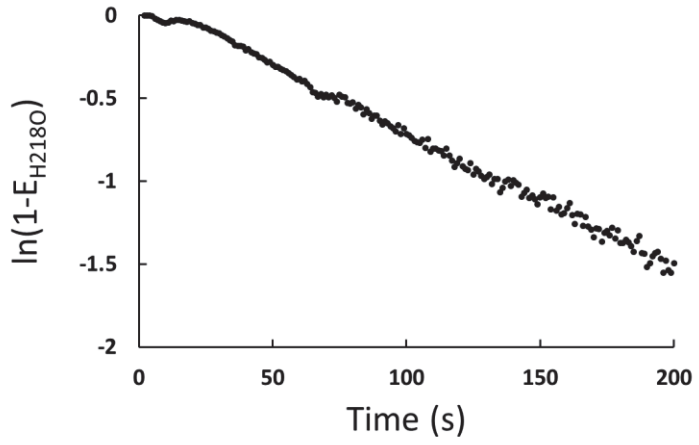

Figure 54: Semi-logarithmic plot of decay of O^{16} for the methane, $H_2/CO=4$ and T=235°C, Xco=8%

The behavior shown in Figure 54 could be assigned to a single reacting pool but it could be that a double type reactivity is masked due to interaction of the alumina support with water.

4.2.6 Step transient experiment over 20%Ni/γ-Al_2O_3

To go further into the mechanistic behavior of the 20%Ni/γ-Al_2O_3 a step-transient switch was performed as follows:

$$\mathbf{He/H_2 \rightarrow Ar/CO/H_2}$$

The behavior is studied at three different temperatures 210, 227, 251°C and keeping the ratio $H_2/CO=4$.

Whereas during SSITKA experiments the catalyst remains under steady-state conditions, during step-transient experiments the steady-state is only attained at the very end of the experiment.

Meanwhile the surface coverages vary over a large range, revealing different mechanistic features. Moreover, transient information on both CH_4 and H_2O are obtained in the same experiment.

Table 23 shows the X_{CO} and the TOF_{co} as function of temperature.

From the Arrhenius plot of TOF_{co} values the apparent activation energy estimated was 78 kJ/mol in agreement with the value calculated from SSITKA experiments.

Table 23: Xco and TOF_{co} at 210, 225 and 250°C with $H_2/CO=4$ during step transient experiment over 20%Ni/γ-Al_2O_3
Total flow=100 mL/min (40 He/60 H_2 →25 Ar/60 H_2/15 CO)

T (°C)	Xco %	TOF_{co} (mol_{co} mol_{Ni}^{-1} s^{-1}) x 10^{-3}
210	2.5	1.9
227	5.0	3.0
251	10.0	8.4

Figure 55 shows the step-response experiments at three different temperatures. At 210°C a small time delay is observed between the Ar step response and the CO and methane step responses. The methane step response shows an overshoot and then slowly decays to the steady-state value. The step response of water is much more delayed than the methane, does not show an overshoot and slowly reaches the steady-state value. Increasing the temperature dramatically reduces the delay of the step response of water. The overshoot on the methane response is no longer present at 227 and 251°C.

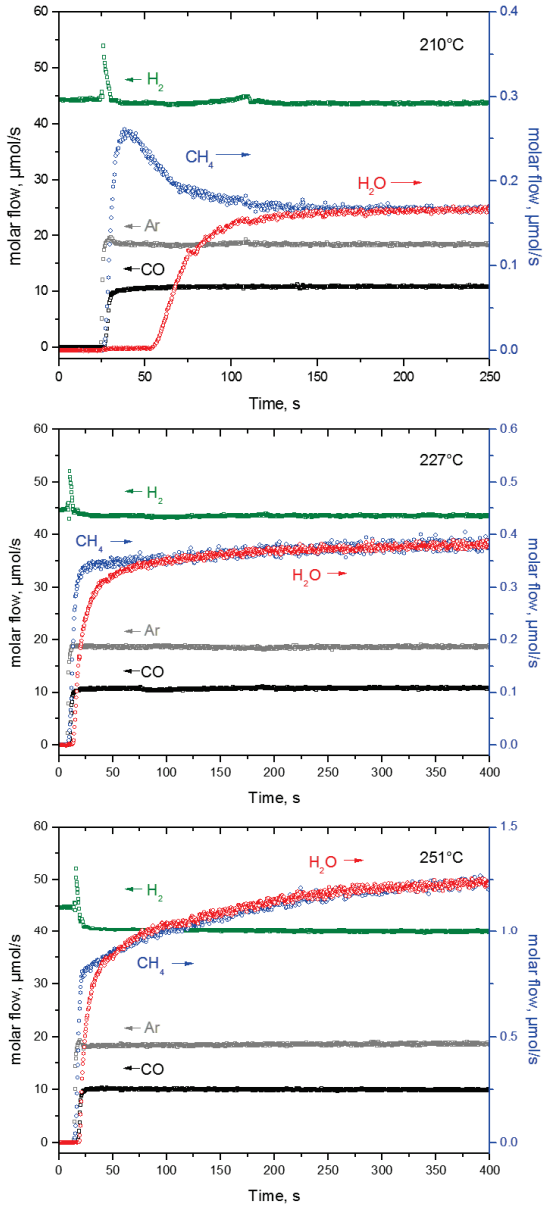

Figure 55: Step response experiment by switching from H_2/He to H_2/CO/Ar at 210, 227, 251°C, P=1.2 bar and H_2/CO=4.
Total flow=100 mL/min (40 He/60 H_2 →25 Ar/60 H_2/15 CO)

Figure 55 shows that at the moment of the switch H_2 always exhibits a peak before reaching the steady state value. A possible explanation for this behavior might be a competition between hydrogen, already on the surface, and carbon monoxide for the same active sites. The stronger

adsorbing CO pushes hydrogen from the surface, in addition to the reaction that is starting.

From the responses in Figure 55 it is possible to compute the integral of atomic surface balances as indicated in section 2.1.2.

By calculating the integral surface species balances, the surface concentration of C_{ads}, H_{ads}, and O_{ads} can be obtained as a function of time.

Figure 56 shows the result at 210°C.At the start of the experiment, the hydrogen surface storage was estimated from the hydrogen adsorption at 210°C. Large fluctuations of the surface concentration of H_{ads} are observed, probably due to small instabilities of the flow and the large ratio of gas phase to surface storage capacity.

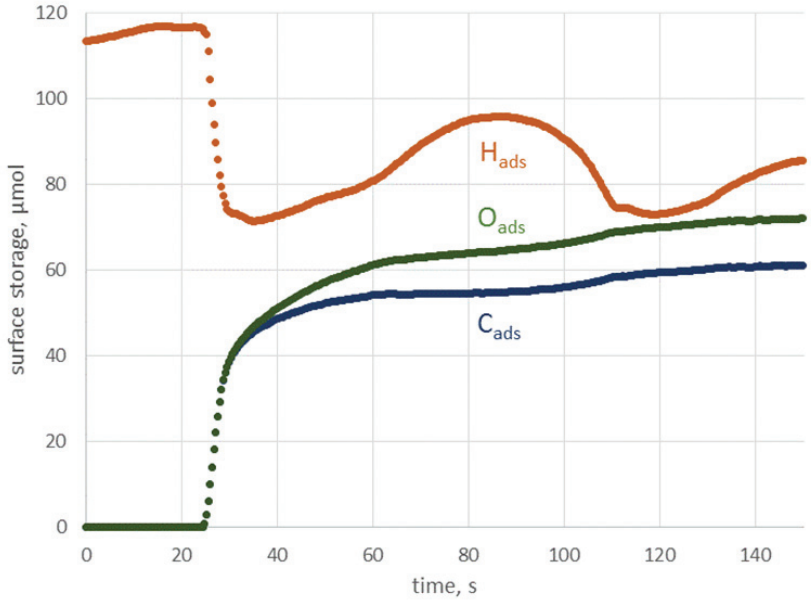

Figure 56: Integral balances of the surface species for pre-adsorption of H2 followed by a switch to CO+H_2 at 210°C.

So using the average values of H_{ads}, O_{ads} and C_{ads} at steady-state and assuming that only CH_x*, CO* OH_y*and H* species are adsorbed in significant amounts, we can define the following equations:

$H_{ads} = H^* + x\ CH_x^* + y\ OH_y^* = 0.4$ mol kg_{cat}^{-1} $\theta_H = 0.58$

$C_{ads} = CH_x^* + CO^* = 0.3$ mol kg_{cat}^{-1} $\theta_C = 0.44$

$O_{ads} = CO^* + OH_y^* = 0.35$ mol kg_{cat}^{-1} $\theta_O = 0.51$

$CH_x^* + CO^* + H^* + OH_y^* + * = 0.680$ mol kg_{cat}^{-1}

The values are those estimated at 210°C. This system has 7 unknowns with only 4 equations, so to get a unique solution the number of unknowns must be reduced on the basis of some additional assumptions. Again the estimation of the total number of active sites is based on the H_2 chemisorption measurements (see 3.5.1, Appendix 1).

4.2.7 Conclusion

To conclude a comparison between SSITKA and step-transient experiment is required.

Table 24 compares the surface coverages estimated with both techniques. It is necessary to recall that while the SSITKA provides information about surface species at steady-state, in the step-transient experiment the steady-state is reached only at the very end of the experiment. However the surface balance provide an estimate of the coverages for H_{ads}, C_{ads} and O_{ads} at steady-state.

Table 24: Comparison of surface coverage estimated from Step-transient and SSITKA experiments at T=210°C, $N_s = 0.68$ $mol_{Ni} \cdot kg_{cat}^{-1}$

T=210°C	θ, Step-Transient	θ, SSITKA
H_{ads}	0.58	>0.16
C_{ads}	0.44	0.73
O_{ads}	0.51	>0.56

The SSITKA gives a higher amount of adsorbed CO and CH_x species than the step-transient. The reason behind this difference is unclear.

Since during the H_2/D_2 SSITKA experiment the water signal was trapped before the MS analysis, the experiment cannot provide any information about the water formation and surface intermediates species like OH. This results in a lower estimation H_{ads} surface coverage

than step-transient experiment. Also for the O_{ads} there is a difference in the values provided by the two techniques. The high coverage value in oxygenates intermediate found at lower temperature is mainly attributed to the hydrophilicity of the γ-Al_2O_3 support. In fact this support effect cause a delay in the water response.

4.3 10%Ni/SiC

4.3.1 Step transient experiment: study of support effect

To study the role that the support plays during methanation reaction, the step transient experiment is also performed over a 10%Ni/SiC.

Silicon Carbide (SiC) is much less hydrophilic than γ-Al_2O_3 expecting less interaction of the support with water.

Again in this case the step change is from an H_2/He mixture to H_2/Ar/CO at a ratio H_2/CO=4 and T= 225°C with a total flowrate of 100 mL/min. Under these conditions the X_{CO} is 6.5%. Figure 57 shows the experimental step responses.

Table 25**:** Xco and TOF_{co} at 225 with H_2/CO=4 during step transient experiment over 10%Ni/SiC
Total flow=100 mL/min (40 He/60 H_2 →25 Ar/60 H_2/15 CO)

T (°C)	Xco %	TOF_{co} (mol_{co} mol_{Ni}^{-1} s^{-1}) x 10^{-3}
225	6.5	12.3

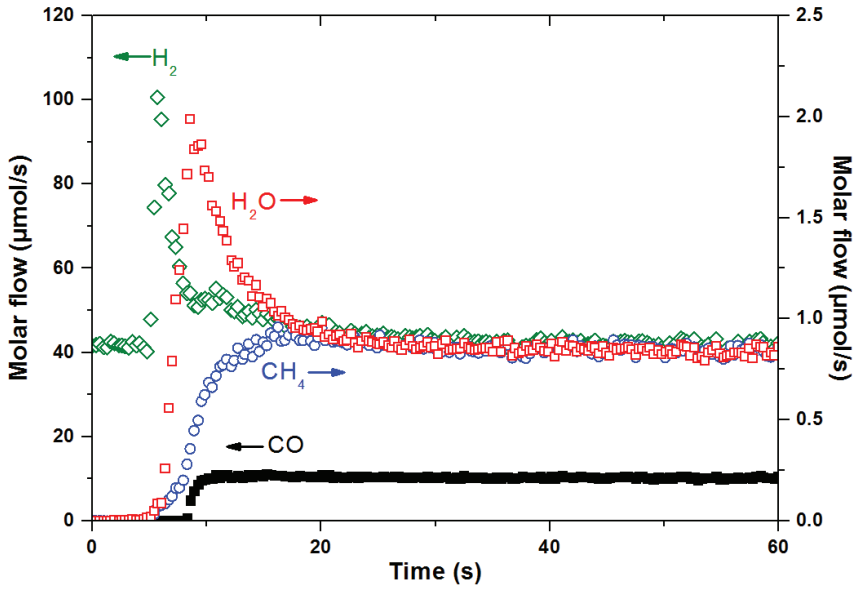

Figure 57: Step response experiment over 10%Ni/SiC, T=225°C and H_2/CO=4, Total flow=100 mL/min (40 He/60 H_2 →25 Ar/60 H_2/15 CO)

Comparing the results on 10%Ni/SiC (Figure 57) and 20%Ni/γ-Al_2O_3 (Figure 55) the main difference is in the H_2O and CH_4 behaviors.

Over a silicon carbide support, the water appears before CH_4 and shows a peak before gradually decaying to the steady-state value. Both CH_4 and H_2O responses appears before the CO response. Also for the 10%Ni/SiC the H_2 exhibits a peak as soon as the system is switched to methanation conditions.

This experiment shows how the kinetics of water formation is much faster than methane over a hydrophilic support.

As for the 20%Ni/γ-Al_2O_3, the surface balance can be written for the 10%Ni/SiC as follows:

$H_{ads} = H^* + x\ CH_x^* + y\ OH_y^* = 0.194$ mol kg_{cat}^{-1} $\theta_H = 0.65$

$C_{ads} = CH_x^* + CO^* = 0.091$ mol kg_{cat}^{-1} $\theta_C = 0.30$

$O_{ads} = CO^* + OH_y^* = 0.055$ mol kg_{cat}^{-1} $\theta_O = 0.20$

$CH_x^* + CO^* + H^* + OH_y^* + * = 0.3$ mol kg_{cat}^{-1}

Due to the fast water production shown in Figure 57, it is reasonable to assume that the coverage of oxygenate intermediates (OH_y) is very low, close to zero, so we can remove this unknown from the surface balances. This than leads to the following equation for the free sites:

$\theta_* = 0.05 + 0.1 * x$

Assuming that at these low temperatures the number of surface free sites is low, leads to x=0.

The surface balances were solved under the assumption of x=0, meaning that the most abundant C-intermediates on surface is atomic carbon. This hypothesis leads to:

$$\theta_H = 0.65$$

$$\theta_{CO} = 0.20$$

$$\theta_C = 0.10$$

4.4 15%Co/SiC

4.4.1 Steady state CO conversion and Selectivity

As already mentioned in the section 3.3 the steady-state performance of 15%Co/SiC are measured by GC/GC-MS analysis using Eq. 17 and Eq. 18-Eq. 20.

Table 26 shows values of CO conversion and selectivity at steady-state for 300 mg of 15%Co/SiC at T=225°C, P=1.6 bar and H_2/CO=2, after 50 h of time on stream with a total flow of 50 mL/min (20 Ar/20 H_2/10 CO)

Table 26: Performances of 15%Co/SiC catalyst: Conversion of CO (%) and lumped selectivities S_{C1}, $S_{C2\text{-}C4}$ and S_{C5} after a 50 h ageing period at 225°C, H_2:CO=2.

T(°C)	X_{CO} (%)	S_{C_1}(%)	$S_{C_2-C_4}$(%)	$S_{C_{5+}}$(%)
225	7	36	40	24

This catalyst at these conditions leads to a rather high methane selectivity and low C_{5+} selectivity compared to the data reported in the literature at typical FT conditions of 20 bar[43].

Table 27: Xco and TOF_{co} at 225 with $H_2/CO=2$ for the 15%Co/SiC after 50 h TOS. Total flow=50 mL/min (20 Ar/20 H_2/10 CO). N_s=0.180 mol kg_{cat}^{-1}

T (°C)	Xco %	r_{CO} (µmol/s)	r_{CH4} (µmol/s)	TOF_{co} (mol_{CO} mol_{Co}^{-1} s^{-1}) x 10^{-3}	TOF_{CH4} (mol_{CH4} mol_{Co}^{-1} s^{-1}) x 10^{-3}
225	7	0.5	0.18	9.3	3.3

4.4.2 ^{13}C-labeling of methane during Fischer-Tropsch reaction

Figure 58 shows the transient responses of Kr, ^{12}CO and ^{13}CO during a SSITKA experiment over 15%Co/SiC.

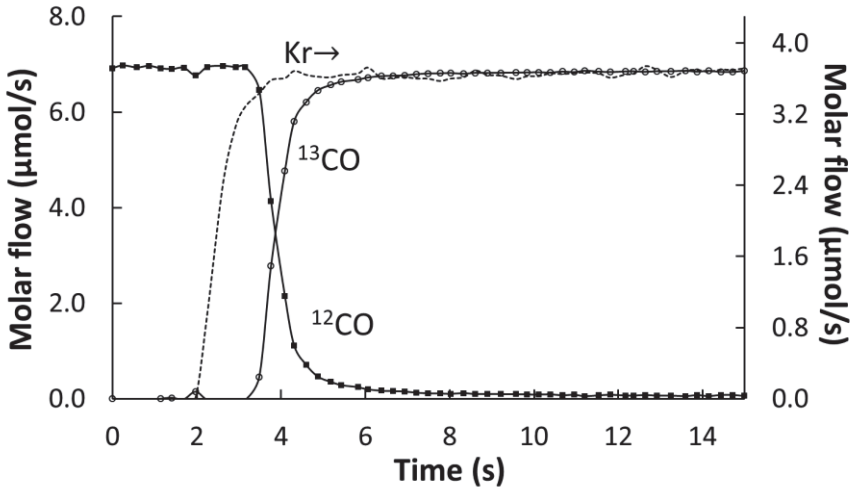

Figure 58: Molar flows of Kr, ^{13}CO, and ^{12}CO on the 15%Co/SiC catalyst at $H_2/CO=2$ and T=225°C
Total flow=50 mL/min (20 Ar/20 H_2/10 ^{12}CO→15 Ar/5 Kr/20 H_2/10 ^{13}CO)

The ^{13}CO is delayed compared to Kr and a surface residence time of ^{13}CO of 3.5 s is found. The responses of ^{13}CO and ^{12}CO crossing each other symmetrically meaning that there is no evidence of a kinetic isotopic effect.

Figure 59 shows the molar flows of $^{12}CH_4$ and $^{13}CH_4$.

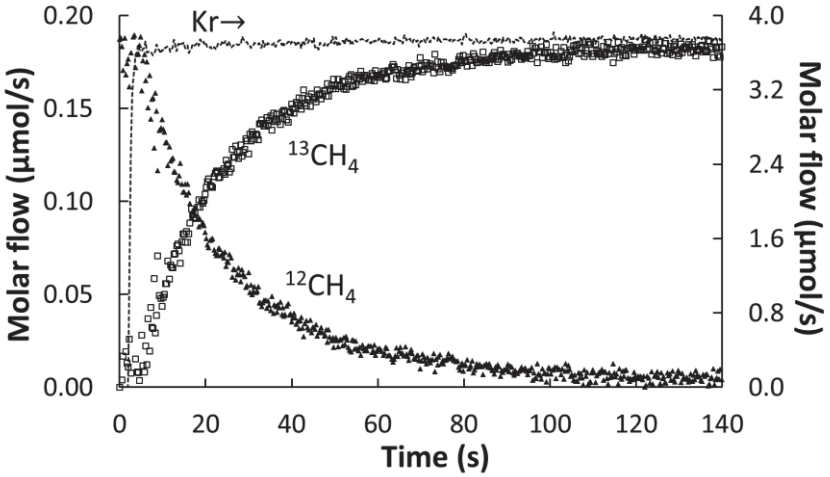

Figure 59: Molar flows of Kr, $^{13}CH_4$, and $^{12}CH_4$ on the 15%Co/SiC catalyst at $H_2/CO=2$ and T=225°C
Total flow=50 mL/min (20 Ar/20 H_2/10 ^{12}CO→15 Ar/5 Kr/20 H_2/10 ^{13}CO)

CH_4 shows a transient much slower than ^{13}CO, the mean surface residence time of methane intermediates is found equal to 31.5 s.

From the SSITKA responses it is possible to perform the estimation of the number of adsorbed CO and intermediate species leading to methane, Table 28 shows the results over 15%Co/SiC:

Table 28: Surface concentrations and coverage of CO_{ads} and $C_{1,ads}$ based on the integration of the MS transients signals. N_s=0.180 mol kg_{cat}^{-1}

T(°C)	X_{CO}(%)	$\tau_{CO}(s)$	$\tau_{C_1}(s)$	$N_{CO}\left(\frac{mol}{kg_{cat}}\right)$	$N_{C_1}\left(\frac{mol}{kg_{cat}}\right)$	θ_{CO}	θ_{C_1}
225	7	3.5	31.5	0.08	0.02	0.45	0.11

Coverages are calculated by taking in to count the number of surface active site, that in case of 15%Co/SiC that were estimated by CO chemisorption.

Table 29 shows the value of TOF, surface coverage of CO and CH_4 intermediates for relevant SSITKA studies present in literature for the Fischer-Tropsch reaction over Co-based catalysts.

Table 29: SSITKA results of relevant literature references over Co-based catalysts. * based on methane production rate i.s.o. of CO consumption

T (°C)	P (bar)	X_{CO} %	H_2/CO	θ_{CO}	θ_{C1}	TOF s^{-1} x 10^3	Ref.
225	1.2	6.5	2	0.63	0.26	14	[119]
210	1.85	22.5	10	0.36	0.08	12.1	[51]
250	1	7	2	0.35	0.20	5*	[120]

Van Dijk[119] found, over a $Co/Ru/TiO_2$, under similar operating condition for the Fischer-Tropsch reaction, a TOF_{co} higher than the one calculated in this study for the 15%Co/SiC. The main discrepancy is in the value of surface coverage of CO and methane that are significantly higher than our values.

Yang and Holmen performed a SSITKA analysis over a 20%Co/γ-Al_2O_3[51], the selected results are for an average particle size of 11 nm.

They used a really high H_2/CO ratio, that leads to a higher X_{CO} compared to our study, but the TOF_{CO} is close to our value and the value reported by Van Dijk[119]. They found values for the coverage of CO and C_1 lower than our values.

Carvalho et al.[120] performed ^{13}C-labeling experiments over a 20%Co/0.1%Pt/SiO_2 and after 146 h of time on stream they found the results shown in Table 29.

The SSITKA analysis results in this study are also in good agreement with the analysis performed by Den Breejen and coworkers[121].

Figure 60 shows the semi-logarithmic plot of the decay of $^{12}CH4$ over 15%Co/SiC:

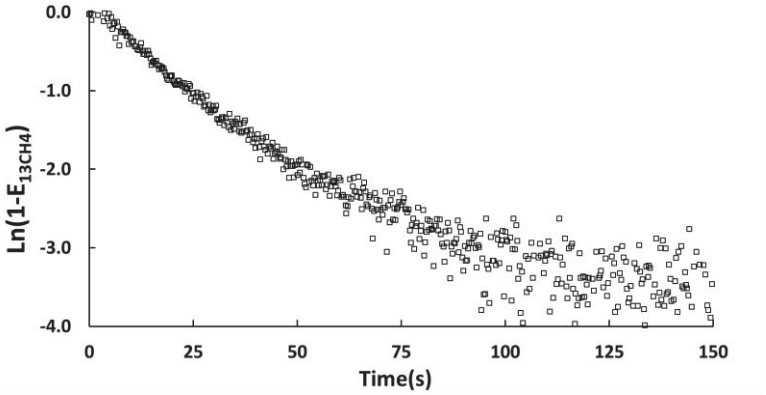

Figure 60: Semi-logarithmic plot of decay of ^{12}C for the methane, T=225°C and $H_2/CO=2$

From Figure 60 no linear decrease was observed, but it rather suggests the presence of more than one reacting C-pools, although it is not a clear cut 2 pool behavior, it looks rather like a continuous distribution of pools.

4.4.3 ^{13}C-labeling of C_2-C_4 products

Over a cobalt based catalyst there is a products distribution that leads to relevant amounts of C_2-C_4 products. Figure 61 gives the (olefin and paraffin) hydrocarbon product distribution at 225°C over Co/SiC.

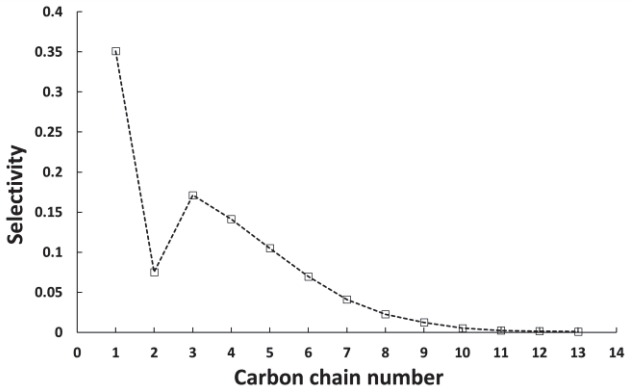

Figure 61: Product selectivity plot for 15%Co/SiC, T=225°C and $H_2/CO=2$

During the ^{13}C-labeling experiment over 15%Co/SiC the products are also analyzed by an online GC-MS that allows to follow the ^{13}C insertion into higher olefin/paraffin products.

Figure 62-Figure 64 show the results of GC-MS analysis:

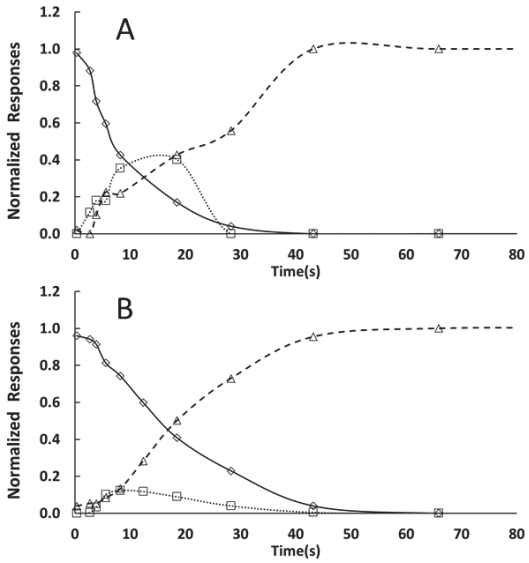

Figure 62: Normalized ^{13}C-labeling responses of ethylene (A) and ethane (B) for the 15%Co/SiC catalyst at 225°C, 1.6 bar, $H_2/CO=2$

◇ $^{12}C_2H_4/^{12}C_2H_6$ □ $^{13}C^{12}CH_4/^{13}C^{12}CH_6$ △ $^{13}C_2H_4/^{13}C_2H_6$

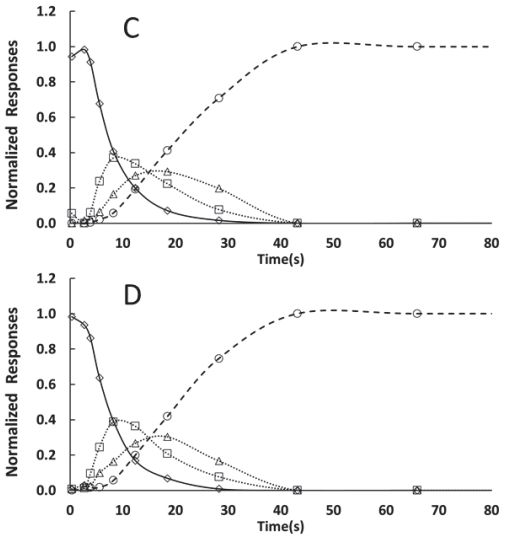

Figure 63: Normalized ^{13}C-labeling responses of propene (C) and propane (D) for the 15%Co/SiC catalyst at 225°C, 1.6 bar, $H_2/CO=2$

◇ $^{12}C_3H_6/^{12}C_3H_8$ □ $^{13}C^{12}C_2H_6/^{13}C^{12}C_2H_8$ △ $^{13}C_2{}^{12}CH_6/^{13}C_2{}^{12}CH_8$ ○ $^{13}C_3H_6/^{13}C_3H_8$

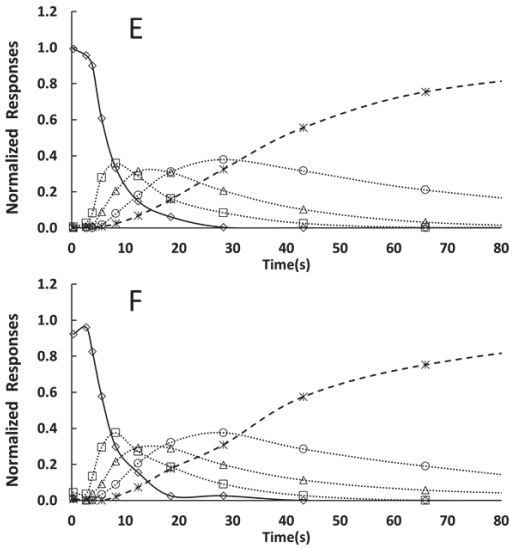

Figure 64: Normalized ^{13}C-labeling responses of 1-butene (E) and butane (F) for the 15%Co/SiC catalyst at 225°C, 1.6 bar, $H_2/CO=2$

◇ $^{12}C_4H_8/^{12}C_4H_{10}$ □ $^{13}C^{12}C_3H_8/^{13}C^{12}C_3H_{10}$ △ $^{13}C_2{}^{12}C_2H_8/^{13}C_2{}^{12}C_2H_{10}$ ○ $^{13}C_3{}^{12}CH_8/^{13}C_3{}^{12}CH_{10}$ ✳ $^{13}C_4H_8/^{13}C_4H_{10}$

In the figures, all responses of the intermediate isotopic product show a maximum, since the experiment starts with zero labeling and ends at full labeling. These maxima shift in time with increasing isotope content of the intermediate isotopic variant for the C_{3+} hydrocarbons (Figure 63).

4.4.4 ^{18}O-labeling on H_2O production during Fischer-Tropsch reaction

As for the 20%Ni/γ-Al_2O_3, the water formation is studied over the 15%Co/SiC by a $C^{16}O/C^{18}O$ SSITKA switch.

The switch is performed as follows:

$$\mathbf{He/C^{16}O/H_2 \rightarrow He/Kr/C^{18}O/H_2}$$

Table 30: Performances of 15%Co/SiC catalyst: Conversion of CO (%) and selectivity to S_{C1} after a 50 h ageing period at 225°C, H_2:CO=2 before performing ^{18}O-labeling experiment.

T(°C)	X_{CO} (%)	S_{C_1} (%)
225	10	52
235	13	57

At 225°C a higher conversion was observed compared to the ^{13}C-labeling experiment at the same temperature. Moreover the selectivity towards CH_4 was higher than 50%.

Figure 65 shows the transient for $C^{16}O/C^{18}O$ at 225°C:

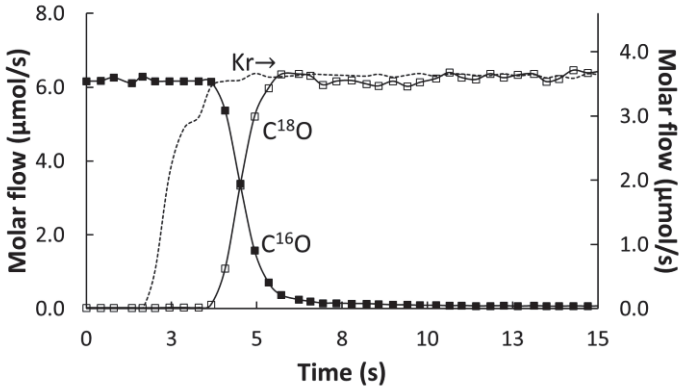

Figure 65: Molar flow of Kr, $C^{16}O$, and $C^{18}O$ on the 15%Co/SiC catalyst at $H_2/CO=2$ and T=225°C after 50 h of TOS
Total flow=50 mL/min (20 He/20 H_2/10 $C^{16}O$→15 He/5 Kr/20 H_2/10 $C^{18}O$)

As for the ^{13}C-labeling experiment, the $C^{18}O$ SSITKA experiment shows symmetry between the responses of regular CO and the isotopic molecule. From Figure 65 it is possible to calculate the mean surface residence time of CO and this leads to a value of 3.2 s close to the 3.5 s found from the ^{13}C-labeling over the same catalyst. Moreover the CO coverage is 0.4, value close to the 0.45 found for the ^{13}C SSITKA experiment, the slight difference in the values could be assigned to the higher X_{CO} in this experiment.

Figure 66 shows the labeling of water molecule during Fischer-Tropsch reaction with ^{18}O-labeled CO molecule:

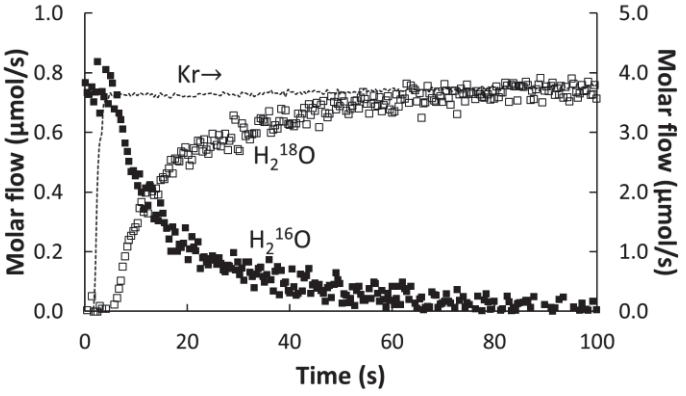

Figure 66: Molar flows of Kr, $H_2{}^{16}O$, and $H_2{}^{18}O$ on the 15%Co/SiC catalyst at $H_2/CO=2$ and T=225°C after 50 h of TOS
Total flow=50 mL/min (20 He/20 H_2/10 $C^{16}O$→15 He/5 Kr/20 H_2/10 $C^{18}O$)

Since the 15%Co/SiC is supported on a less hydrophilic support compared to γ-Al_2O_3, the transient for water is faster at 225°C. Comparing Figure 66 with Figure 59, showing the methane SSITKA response, shows that water has a faster transient than methane. This is also reflected in the difference in the mean surface residence time. At 225°C the τ_{13CH4} is 31.5 s (Table 28) while the $\tau_{H_2^{18}O}$ is 17 s, so almost 2 times faster.

Figure 67 shows the semi-logarithmic plot of the decay of $H_2{}^{16}O$ at 235°C.

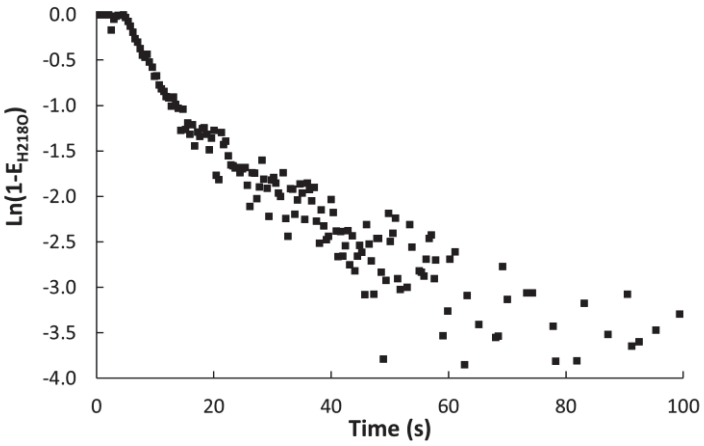

Figure 67: Semi-logarithmic plot of decay of ^{16}O for the water over 15%Co/SiC, T=235°C and H_2CO=2

The water production over the 15%Co/SiC, shows in this case a distribution of several pools, as was the case for the methane formation over 15%Co/SiC.

Table 31 summarizes the results for ^{18}O-labeling experiments performed over 15%Co/SiC.

Table 31: Surface concentrations and coverages of CO_{ads} and $H_2O_{,ads}$ based on the integration of the $C^{16}O/C^{18}O$ transients

T(°C)	X_{CO}(%)	$\tau_{C^{18}O}(s)$	$\tau_{H_2^{18}O}(s)$	$N_{C^{18}O}\left(\frac{mol}{kg_{cat}}\right)$	$N_{H_2^{18}O}\left(\frac{mol}{kg_{cat}}\right)$	θ_{CO}	θ_{H_2O}
225	10	3.2	16	0.07	0.04	0.40	0.23
235	13	2.3	11	0.05	0.035	0.27	0.19

Table 32**:** TOF and reaction rates for the 15%Co/SiC after 50 h TOS with $H_2/CO=2$. $N_s=0.180$ mol kg_{cat}^{-1}

T (°C)	Xco %	r_{CO} (µmol/s)	r_{CH4} (µmol/s)	TOF_{co} (mol_{CO} mol_{Co}^{-1} s^{-1}) x 10^{-3}	TOF_{CH4} (mol_{CH4} mol_{Co}^{-1} s^{-1}) x 10^{-3}
225	10	0.68	0.35	12.6	6.6
235	13	0.92	0.52	17.0	9.7

The value estimated from the results in Table 32 is 62 kJ/mol.

This value is lower than the usual range of 90-120 kJ/mol reported in literature[98,45,122,123]. However Atashi et al.[124] and Mansouri et al.[125] reported for Co-based catalysts a range between 35 and 55 kJ/mol.

4.4.5 Step transient experiment

Step-transient experiments were also performed over 15%Co/SiC. During this experiment the investigation was focused on the H_2O and CH_4 production.

Figure 68 shows the outlet molar flows for H_2, CO, H_2O and CH_4.

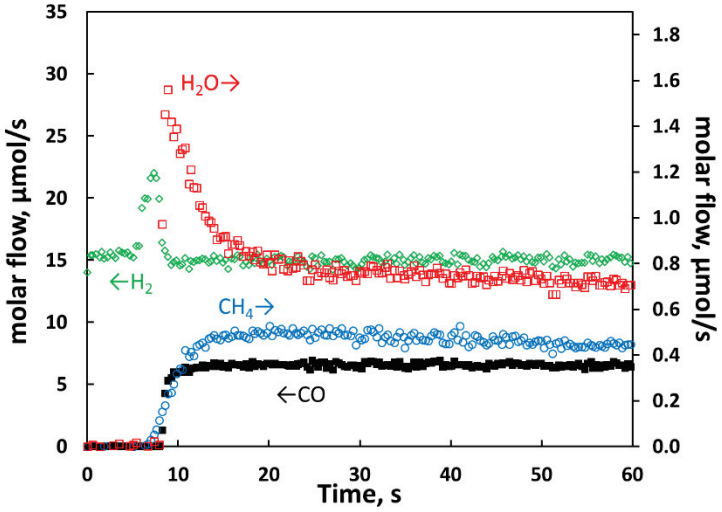

Figure 68: Step response experiment by switching from H_2/Ar to H_2/CO/Ar
T=225°C and H_2/CO=2, X_{CO}=10% and S_{CH4}=52%
Total flow=50 mL/min (30 He/20 H_2 →15 He/5 Kr/20 H_2/10 CO)

Figure 68 and Figure 57 show the same experiment performed over 15%Co/SiC and 10%Ni/SiC at a temperature of 225°C. The two samples exhibit a very similar behavior.

Both catalysts show a water peak in the first 2-3s of reaction while the methane reaches the steady-state value gradually.

Also in the case of 15%Co/SiC the peak in hydrogen is shown, due to the adsorption of CO when switched to Fischer-Tropsch operating conditions.

In case of 15%Co/SiC the amount of methane produced is lower due to the higher carbon number products formed during the Fischer-Tropsch reaction, in that case a selectivity to methane (S_{CH4}) of 0.52 was found.

The same experiment was repeated over 15%Co/SiC, but this time 0.300 g of catalyst were diluted with 0.300 g of alumina powder

(Puralox SCCa, spherical type 80 µm powder; 166 m^2/g; porous volume, 0.44 cc/g; pore diameter, 13.6 nm; density, 0.34) in order to investigate the water adsorption.

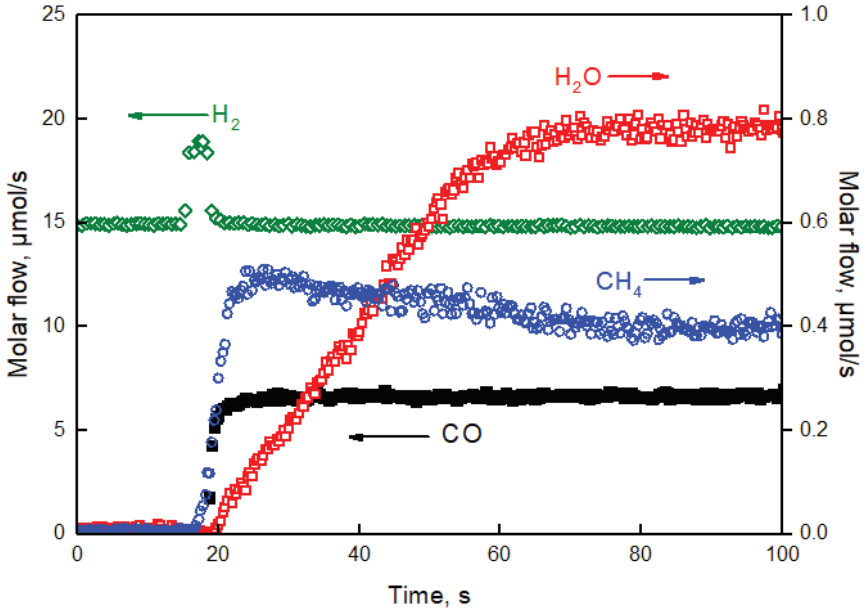

Figure 69: Step response experiment by switching from H_2/Ar to H_2/CO/Ar performed over 0.3 g of 15%Co/SiC diluted with 0.3 g of Puralox SCCa
T=225°C and $H_2/CO=2$, $X_{CO}=10\%$ and $S_{CH4}=52\%$
Total flow=50 mL/min (30 He/20 H_2 →15 He/5 Kr/20 H_2/10 CO)

Figure 69 shows the result. As expected the water response is affected by the presence of the hydrophilic alumina powder, this is clearly shown by the linear behavior of water response between 20 and 60 s.

The delay between water and methane response is about 5 s and the water signal reaches the steady-state value only after 80 s, moreover the methane exhibits a small peak that was not the case for the previous case in which the 15% Co/SiC was diluted with silicon carbide.

The presence of a hydrophilic material, like alumina, affects the water signal, masking information on the water formation.

4.4.6 Effects of co-fed ^{12}ethylene during Fisher-Tropsch synthesis

As shown in Figure 61 not only the methane deviates from the ASF ideal distribution (see 1.2.2) but also the C_2 products. Ethylene and ethane show a lower selectivity than the value predicted by the ASF distribution.

It was proposed that the ethylene formed by CO hydrogenation has a higher tendency to re-adsorb and re-enter the chain growth process[126] via the methylene insertion mechanism[127]. Ethylene has therefore been widely used as a probe molecule (co-fed with syngas) to investigate its influence on the FTS mechanism[128, 126].

All studies have shown that ethylene acts primarily as a chain initiator. In addition, some authors speculated that ethylene can also be dissociated to C_1 intermediate fragments by hydrogenolysis to serve as a source of monomer for chain growth[126,129].

To study the behavior of ethylene during Fischer-Tropsch reaction over 15% Co/SiC, ^{12}ethylene was added during steady-state ^{13}CO Fischer-Tropsch reaction.

A sample of 300 mg of catalyst was exposed for 50 h at 225°C to a flow rate of 50 mL/min of $^{12}CO/H_2/Ar$ (10/20/20 mL/min), then for 30 min the ^{12}CO was replaced by ^{13}CO and at the end 0.5 mL/min of $^{12}C_2H_4$ were added for 10 min (Figure 70).

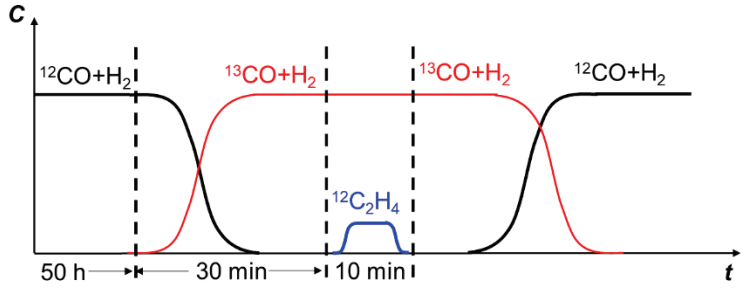

Figure 70: Schematic representation of $^{12}C_2H_4$ co-fed experiment performed in this study

The aim of this study was to follow by MS and GCMS the production of $^{12}CH_4$ and the insertion of ^{12}C atoms into higher paraffins and olefins.

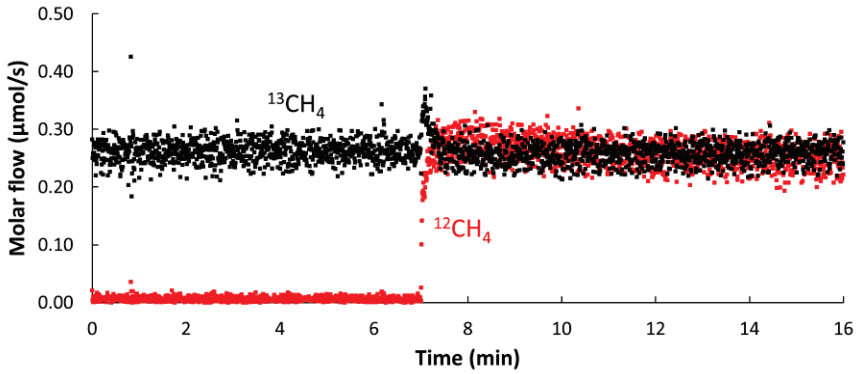

Figure 71: Molar flow of $^{13}CH_4$ and $^{12}CH_4$ during $^{12}C_2H_4$ co-fed experiment over 15%Co/SiC at 225°C and $H_2/CO=2$. $X_{CO}=10\%$ and $S_{CH4}=38\%$

Figure 71 shows the $^{13}CH_4$ and $^{12}CH_4$ responses during $^{12}C_2H_4$ co-fed.

As soon as $^{12}C_2H_4$ is added to the syngas flow, suddenly $^{12}CH_4$ (red dots) starts being produced, and reaches the same value of $^{13}CH_4$ produced from ^{13}CO at steady state. So basically introducing 0.5 mL/min of ethylene doubles the amounts of methane produced by the reaction.

This suggests that the ethylene re-adsorbs on the catalyst surface and via hydrogenolysis is transformed into methane. It can also be a source of CH_x species that leads to monomers for carbon chain growth.

Figure 72 shows the GC-MS data collected for Propene, Propane.

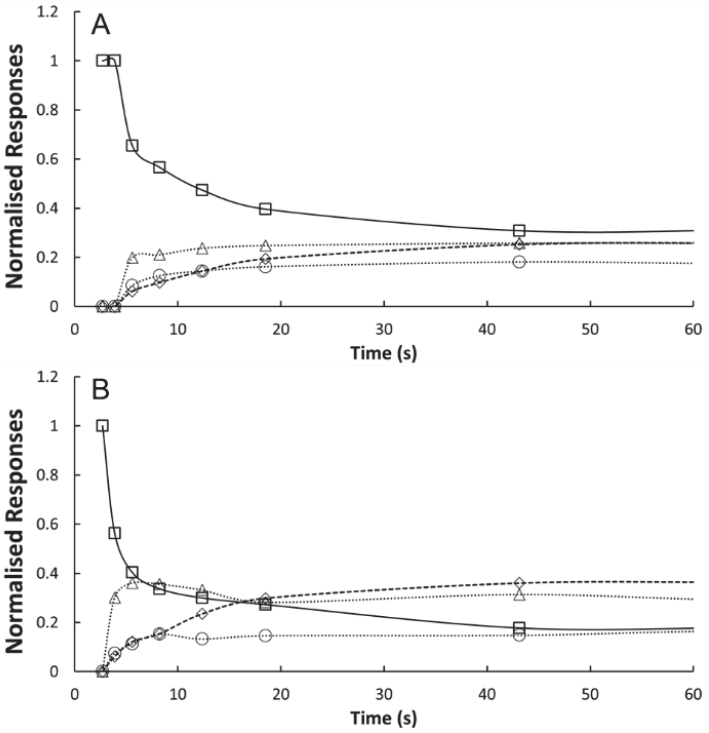

Figure 72: Normalized responses of propene (A) and propane (B) for the 15%Co/SiC catalyst during $^{12}C_2H_4$ co-fed at 225°C, 1.6 bar, $H_2/CO=2$

◇ $^{12}C_3H_6/^{12}C_3H_8$ ○ $^{13}C_2{}^{12}C_1H_6/^{13}C_2{}^{12}C_1H_8$ △ $^{13}C_1{}^{12}C_2H_6/^{13}C_1{}^{12}C_2H_8$ □ $^{13}C_3H_6/^{13}C_3H_8$

Figure 72 shows the ^{12}C distribution in the C_3 products after introduction of $^{12}C_2H_4$. The $^{13}C_3$ products start to decrease reaching gradually the steady-state value. During the first seconds of the switch both propene and propane show a peak for the species that presents two ^{12}C and one ^{13}C. This suggests that the whole ethylene molecule participates directly to the chain growth of higher C-products.

This behavior was observed also in 1-butene and butane responses (Figure 73):

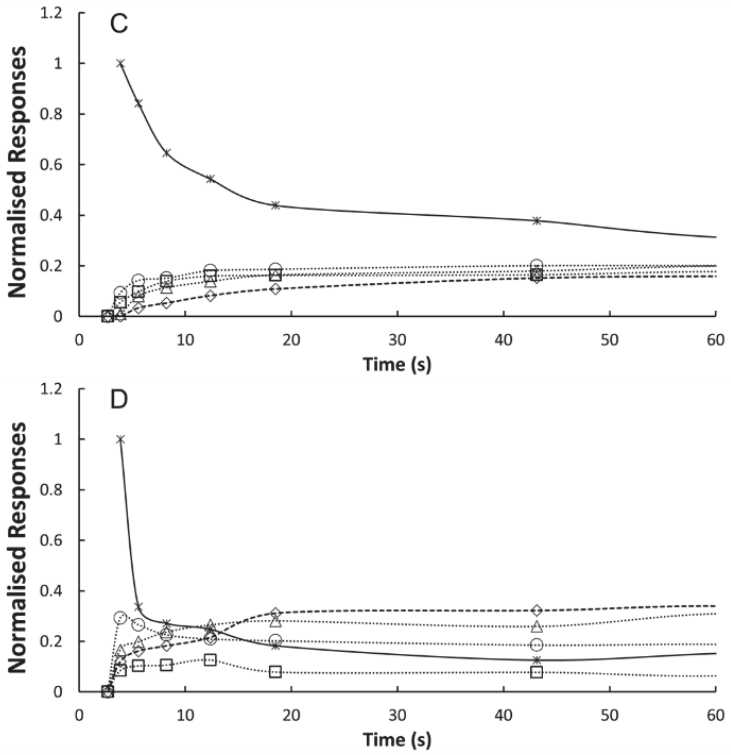

Figure 73: Normalized ^{13}C-labeling responses of 1-butene (C) and butane (D) for the 15%Co/SiC catalyst during $^{12}C_2H_4$ co-fed at 225°C, 1.6 bar, $H_2/CO=2$

◇ $^{12}C_4H_8/^{12}C_4H_{10}$ △ $^{13}C^{12}C_3H_8/^{13}C^{12}C_3H_{10}$ ○ $^{13}C_2{}^{12}C_2H_8/^{13}C_2{}^{12}C_2H_{10}$
□ $^{13}C_3{}^{12}CH_8/^{13}C_3{}^{12}CH_{10}$ ✳ $^{13}C_4H_8/^{13}C_4H_{10}$

The two ^{12}C exchanged C_4-products have, as for the C_3, the highest concentration during the first second of the experiments.

Moreover at the steady-state the C_3 and C_4 alkanes present a significant fraction of completely exchanged product.

These results are in good agreement with the study of Turner and coworkers[130]. They performed the Fischer-Tropsch reaction over a Ru, Fe and Co-based catalyst in the temperature range of 180-220°C adding $^{13}C_2H_4$. Through NMR spectroscopy analysis and GC-MS analysis they found over cobalt and iron that the most abundant isotopomers of propene were $^{13}CH_3{}^{13}CH{=}CH_2$ and $CH_3{}^{13}CH{=}{}^{13}CH_2$, so those with 2 C atoms exchanged. For the 1-Butene they found over cobalt at 180°C

and over iron at 220°C NMR spectra indicating it to be mainly as $^{13}CH_3{}^{13}CH_2CH{=}CH_2$.

4.5 Conclusions

This chapter reported the results for an extensive kinetic investigation over three catalysts samples:

1. 20%Ni/γ-Al_2O_3: ^{13}C-, ^{18}O-, and D-labeling experiments under comparable experimental conditions were performed as well as step-transient experiments.
2. 10%Ni/SiC: the support effect was investigated by performing step-transient experiment and comparing these to those on alumina supported catalyst.
3. 15%Co/SiC: the steady state performances were studied during Fischer-Tropsch conditions at ~1 bar, ^{13}C-, ^{18}O-labeling SSITKA experiments were performed. Also for this catalyst step-transient experiment were performed.

The qualitative interpretation of the transients lead to the following conclusions:

• The surface coverage of CO is decreasing with increasing the temperature from 0.56 at 210°C to 0.31 at 250°C.

• The catalyst surface is heterogeneous with respect to the methane intermediate. Two intermediates are defined, with two clearly different types of reactivity. These two reaction pools are in series with a first pool represented by the reversible adsorption of CO, two possible reaction pathways are:

$$CO(g) \rightleftarrows CO_{ads} \rightarrow \begin{matrix} C_{\alpha,\,ads} \rightarrow CH_4(g) \\ \searrow\ C_{\beta,\,ads}\ \nearrow \end{matrix} \qquad CO(g) \rightleftarrows CO_{ads} \rightarrow \begin{matrix} C_{\alpha,\,ads} \rightarrow CH_4(g) \\ \uparrow\downarrow \\ C_{\beta,\,ads} \end{matrix}$$

• D-labeling SSITKA experiment over 20%Ni/γ-Al_2O_3 has shown a reverse isotopic effect switching from H_2 to D_2.The D-methane transients show the heterogeneity of surface also for the H pools. No information on water could be deduced from this experiment. The experiment shows the distribution of all CD_xH_{4-x} products. The highest intensity was found for the CH_2D_2 that suggest that the CH_2* is the most

abundant carbon intermediate. A possible H reacting path to methane formation could be:

$$D_2(g) \rightleftarrows 2\,D^* + CO^* \begin{matrix} \nearrow\ C_{\alpha,\,ads} + D^* \searrow \\ \searrow\ C_{\beta,\,ads} + D^* \nearrow \end{matrix} CH_{4-x}D_x(g)$$

• The ^{18}O-labeling experiment showed a strong interaction between the $H_2{}^{18}O$ and the Ni/γ-Al_2O_3 catalyst.

• ^{13}C, ^{18}O-labeling and step transient experiment were also performed over 15%Co/SiC to compare the kinetics of methane and water formation during methanation and Fischer-Tropsch reaction. For the 15%Co/SiC a distribution of C-intermediate pools leading to methane is found, and for the $H_2{}^{18}O$ formation the same result has been shown. ^{18}O SSITKA experiments showed a faster transient for water than methane during ^{13}C SSITKA. This was consistent with the faster water formation than methane during step-transient experiments.

From SSITKA experiments the surface consists of the following surface coverage for 20%Ni/γ-Al_2O_3 and 15%Co/SiC:

T=225°C P=1.2 bar	**θ_{CO}**	**θ_{CHx}**	**θ_{OHx}**
20%Ni/γ-AL_2O_3	0.39	0.26	-
15%Co/SiC	0.40-0.45	0.11	0.23

• To study the support effect step-transient experiments were also performed over 10%Ni/SiC. In that case the behavior was exactly the opposite: the water formation was faster than methane.

• Step-transient experiments over 15%Co/SiC showed a similar behavior as 10%Ni/SiC, with a water formation faster than methane. Moreover step-transient experiment over 15%Co/SiC diluted with alumina powder has confirmed the interaction between water and this material.

• Comparing the SSITKA and the step-transient techniques the main discrepancy is noticed on the value of surface coverages estimated from both techniques (Table 24).

• SSITKA and step-transient experiments are complementary, both provide useful information on different side of the same reaction. SSITKA are useful to identify the possible reacting pathways on catalyst surface while the step-transient provide more mechanistically meaningful information in the first minutes of reaction.

Because the experiments are conducted at well-defined experimental conditions in a well-defined reactor environment, the ^{13}C- and ^{18}O-labeling results are suitable for modeling purposes. The mechanistic aspects highlighted in this chapter are combined with the findings based on the steady state behavior of the catalysts and the aspects from the literature review in chapter 1 to yield a mechanistic model for the methanation reaction. The kinetic parameters of this mechanistic model are estimated by regression analysis in chapter 5.

Chapter 5

Microkinetic Modeling

In the following chapter the SSITKA and step-transient experiments are investigated by means of a detailed microkinetic model describing the water and the methane production over Ni-based catalysts.

5.1 SSITKA response modeling

5.1.1 Reaction mechanism of methanation over 20%Ni/γ-Al_2O_3

The experimental evidence of two reactive intermediates towards methane has been observed during the SSITKA experiments in chapter 4. Based on gas phase and surface components several microkinetic models could be defined.

In a microkinetic study the rate of each elementary reaction step is calculated explicitly, thus no a priori assumption on the rate-determining step. The model predicted conversion rates and product distribution are then compared to the experimental results and if necessary some model parameters are adjusted to obtain an adequate fit of the data.

Most modeling studies of SSITKA data consider only the change of the labelled species. In this case not all reactants are taken into account and only apparent rate constants are estimated; for example the SSITKA experiments modeled by Van Dijk et al [47,86,87], lead to rate constants that still depend on the hydrogen coverage. Here a full microkinetic model is developed, including all reactants thus not only the labelled one. Therefore the full model needs to be solved to reach a steady state before the isotopic switch

Table 33 lists the characteristics of the reactor and the operating conditions used for the modeling:

Table 33: Reactor configuration and operating conditions used for SSITKA modeling of 20% Ni /Al_2O_3 responses

Operating variable	**Value**
Amount of catalyst	0.2 g
Catalyst bed length	10.7 mm
Reactor inner diameter	7.73 mm
Bed porosity	0.5 m^3_{void}/m^3_{bed}
Flow rate	100 Nml min^{-1}
P_{tot}	100 kPa
T	210, 225, 251°C
ρ_{cat}	800 kg m^{-3}
Surface active site, N_s	1100 mol m^{-3}

The model contains one or two reaction paths (carbon pools) on the surface that lead to methane.

The kinetics of CO methanation over nickel based catalysts have been studied intensively. Alstrup[131] gave an overview of the kinetic models for CO methanation over nickel and proposed a microkinetic model that gave a good description of a number of different data sets. The model predicts well the often observed hydrogen order around 1 and the CO order around -1 at low temperatures.

The first model (Model 1) was based on this model proposed by Alstrup[131]. It is based on reversible competitive adsorption of hydrogen and carbon monoxide, followed by the direct dissociation of CO* in C* and O* with a consecutive stepwise hydrogenation of C* to CH_4(g) representing the only reaction path to produce methane. All the elementary steps are described in Table 34.

To calculate the rate of each elementary step the law of mass action is applied. Two pre-exponential factors and two activation energies need to be known to describe each step reversibly. However, as shown later in this chapter only the forward rate constants could be estimated, due to the operating conditions far from thermodynamic equilibrium.

The kinetic constant k_i is described by a reparametrized form of the Arrhenius law to minimize correlation between the pre-exponential factor and the activation energy:

$$k_i = k_i^0 \ e^{\left[\frac{-E_i}{R}\left(\frac{1}{T_0}-\frac{1}{T}\right)\right]}$$

Eq. 24

Where:

k_i^0 is the pre-exponential factor of elementary step i

E_i is the activation energy of elementary step i

R is ideal gas constant

T_0 is the reference temperature

T is the operating temperature

The objective function for the regression analysis of the SSITKA responses include the step responses of ^{13}CO and $^{13}CH_4$. All other responses are calculated by the model but not used during the parameter estimation. As the response intensity of $^{13}CH_4$ is much smaller than that of ^{13}CO, a weighting factor of 0.1 was applied to the $^{13}CH_4$ response.

In Table 34 step 1 and step 2 describe the competitive reversible adsorption of CO and H_2 respectively. Once the carbon monoxide is adsorbed on catalyst surface (CO*) undergoes directly to be dissociated (step 3) in C* and O*.

At this point, in step 4, the C* adsorbed on surface reacts with H* to form CH* that are hydrogenated as well to CH_2* and CH_3* (step 5-6).

In step 7 the CH_3* species are hydrogenated to CH_4 that suddenly desorbs from surface with 2 free sites available at the end.

The last two step, step 8-9, describe the water formation. The O* formed by step 3 reacts firstly with H* in step 8 to form OH* and then through step 9 the OH* species are hydrogenated again to H_2O that, like methane, leaves the surface and makes available 2 free sites.

Table 34: Rate expression for the elementary steps considered in the Model 1

Reaction		Rate expression
	Elementary reaction	
	Reactant adsorption	
1) $r_{CO\ chemsorption,desorption}$	$CO(g) + * \leftrightarrows CO^*$	$r_{CO} = k_1 P_{CO} \theta_v - k_{-1} \theta_{CO^*}$
2) $r_{H_2\ chemsorption,desorption}$	$H_2(g) + 2* \leftrightarrows 2H^*$	$r_{H_2} = k_2 P_{H_2} \theta_v^2 - k_{-2} \theta_{H^*}^2$
	Initiation reaction	
3) $r_{CO^*\ diss,ass}$	$CO^* + * \leftrightarrows C^* + O^*$	$r_{CO} = k_3 \theta_{CO^*} \theta_v - k_{-3} \theta_{C^*} \theta_{O^*}$
4) $r_{C\ hydr,dehydr}$	$C^* + H^* \leftrightarrows CH^* + *$	$r_C = k_4 \theta_{C^*} \theta_{H^*} - k_{-4} \theta_{CH^*} \theta_v$
5) $r_{CH\ hydr,dehydr}$	$CH^* + H^* \leftrightarrows CH_2^* + *$	$r_{CH} = k_5 \theta_{CH^*} \theta_{H^*} - k_{-5} \theta_{CH_2^*} \theta_v$
6) $r_{CH_2\ hydr,dehydr}$	$CH_2^* + H^* \leftrightarrows CH_3^* + *$	$r_{CH_2} = k_6 \theta_{CH_2^*} \theta_{H^*} - k_{-5} \theta_{CH_3^*} \theta_v$
	Methane formation	
7) $r_{CH_4\ formation}$	$CH_3^* + H^* \leftrightarrows CH_4(g) + 2*$	$r_{CH_4} = k_7 \theta_{CH_3^*} \theta_{H^*} - k_{-7} P_{CH_4} \theta_v^2$
	Water formation	
8) $r_{O\ hydr,dehydr}$	$O^* + H^* \leftrightarrows OH^* + *$	$r_O = k_8 \theta_{O^*} \theta_{H^*} - k_{-8} \theta_{OH^*} \theta_v$
9) $r_{H_2O\ formation}$	$OH^* + H^* \leftrightarrows H_2O(g) + 2*$	$r_{H_2O} = k_9 \theta_{OH^*} \theta_{H^*} - k_{-7} P_{H_2O} \theta_v^2$

Regression analysis of the SSITKA data at 210°C over Ni/Al_2O_3 was performed with the reaction mechanism shown in Table 34. All forward rate parameters were optimized except those for the hydrogen adsorption equilibrium constant, which was fixed at the value estimated from the dynamic hydrogen adsorption experiments.

Figure 74 shows the model fit of Kr, ^{13}CO, $^{13}CH_4$, H_2 and H_2O during ^{13}C SSITKA experiment:

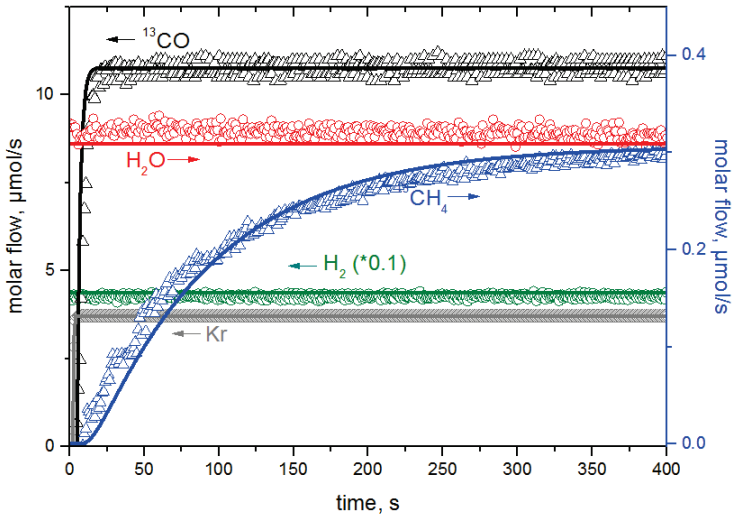

Figure 74: Regression results according to Model 1 at 210°C
Experimental (dots), Model (solid line)

The mechanism of Table 34 based on the study of Alstrup[131] describes the methane and water formation with an overall good agreement. The steady-state levels of H_2 and CO are also well predicted. However, this model does not describe completely the ^{13}CO transient, especially the onset and the top part.

To test the hypothesis proposed by Iglesia et al.[40], Tronconi et al. [43] and Aparicio[46] a second model (Model 2) that takes into count only the H-assisted CO dissociation reacting path, was tested. The description of kinetic elementary steps is shown in Table 35.

Table 35: Rate expression for the elementary steps considered in the Model 2

Reaction		Rate expression
	Elementary reaction	
	Reactant adsorption	
1) $r_{CO\ chemsorption,desorption}$	$CO(g) + * \leftrightarrows CO^*$	$r_{CO} = k_1 P_{CO} \theta_v - k_{-1} \theta_{CO^*}$
2) $r_{H_2\ chemsorption,desorption}$	$H_2(g) + 2* \leftrightarrows 2H^*$	$r_{H_2} = k_2 P_{H_2} \theta_v^2 - k_{-2} \theta_{H^*}^2$
	Initiation reaction	
3) $r_{CO^*hydr,dehydr}$	$CO^* + H^* \leftrightarrows HCO^* + *$	$r_{CO} = k_3 \theta_{CO^*} \theta_{H^*} - k_{-3} \theta_{HCO^*} \theta_v$
4) $r_{HCO^*\ hydr,dehydr}$	$HCO^* + H^* \leftrightarrows CH^* + OH^*$	$r_{HCO} = k_4 \theta_{HCO^*} \theta_{H^*} - k_{-4} \theta_{CH^*} \theta_{OH^*}$
5) $r_{CH\ hydr,dehydr}$	$CH^* + H^* \leftrightarrows CH_2^* + *$	$r_{CH} = k_5 \theta_{CH^*} \theta_{H^*} - k_{-5} \theta_{CH_2^*} \theta_v$
6) $r_{CH_2\ hydr,dehydr}$	$CH_2^* + H^* \leftrightarrows CH_3^* + *$	$r_{CH_2} = k_6 \theta_{CH_2^*} \theta_{H^*} - k_{-5} \theta_{CH_3^*} \theta_v$
	Methane formation	
7) $r_{CH_4\ formation}$	$CH_3^* + H^* \leftrightarrows CH_4(g) + 2*$	$r_{CH_4} = k_7 \theta_{CH_3^*} \theta_{H^*} - k_{-7} P_{CH_4} \theta_v^2$
	Water formation	
8) $r_{O\ hydr,dehydr}$	$O^* + H^* \leftrightarrows OH^* + *$	$r_O = k_8 \theta_{O^*} \theta_{H^*} - k_{-8} \theta_{OH^*} \theta_v$
9) $r_{H_2O\ formation}$	$OH^* + H^* \leftrightarrows H_2O(g) + 2*$	$r_{H_2O} = k_9 \theta_{OH^*} \theta_{H^*} - k_{-7} P_{H_2O} \theta_v^2$

The main difference between the Model 1 and Model 2 is the CO activation step. Both model (Table 34-Table 35) have the same number of elementary step and start with competitive and reversible adsorption of CO and H_2.

The difference is in the step 3 and 4. In the Model 2 (Table 35) the CO* does not dissociate to C* and O* but reacts with H to form HCO* intermediate species (step 3).

Through step 4, the HCO* intermediate reacts with hydrogen and is suddenly decomposed to CH* and OH*. The CH* species follows later the same path towards CH_4 already described for Model 1.

This time the water formation starts from OH* species (step 8-9), these species are directly hydrogenated to water (step 9) or dissociate to O* and H* adsorbed on surface (step 8).

The regression results for the same SSITKA experiment at 210°C over Ni/γ-Al_2O_3 are shown in Figure 75:

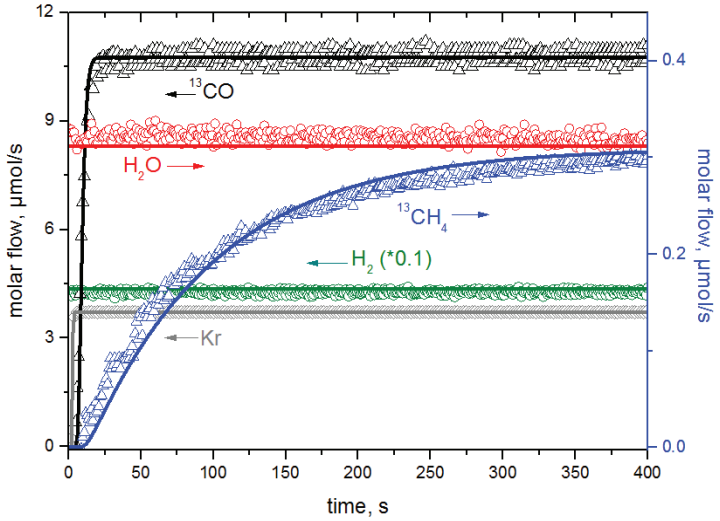

Figure 75: Regression results according to Model 2 at 210°C
Experimental (dots), Model (solid line)

With the H-assisted CO decomposition path model the fit for the ^{13}CO is improved while for the $^{13}CH_4$ SSITKA response the results is similar to the single carbide intermediate pool.

Already shown by Walter et al.[132] as well as by Van Dijk [47] a compartment model with two reacting carbon pools describes the methane formation better. To follow this 2-pools hypothesis we defined a third model that presents both reacting paths: the direct CO dissociation and the H-assisted CO dissociation (Table 36).

Table 36: Rate expression for the elementary steps considered in the Model 3

Reaction		Rate expression
	Elementary reaction	
	Reactant adsorption	
1) $r_{CO\ chemsorption,desorption}$	$CO(g) + * \leftrightarrows CO^*$	$r_{CO} = k_1 P_{CO} \theta_v - k_{-1} \theta_{CO^*}$
2) $r_{CO\ chemsorption,desorption}$	$CO(g) + ** \leftrightarrows CO^{**}$	$r_{CO} = k_2 P_{CO} \theta_v - k_{-2} \theta_{CO^{**}}$
3) $r_{H_2\ chemsorption,desorption}$	$H_2(g) + 2* \leftrightarrows 2H^*$	$r_{H_2} = k_3 P_{H_2} \theta_v^2 - k_{-3} \theta_{H^*}^2$
	Direct CO dissociation	
4) $r_{CO^*\ diss,ass}$	$CO^* + * \leftrightarrows C^* + O^*$	$r_{CO} = k_4 \theta_{CO^*} \theta_v - k_{-4} \theta_{C^*} \theta_{O^*}$
5) $r_{C\ hydr,dehydr}$	$C^* + H^* \leftrightarrows CH^* + *$	$r_C = k_5 \theta_{C^*} \theta_{H^*} - k_{-5} \theta_{CH^*} \theta_v$
6) $r_{CH\ hydr,dehydr}$	$CH^* + H^* \leftrightarrows CH_2^* + *$	$r_{CH} = k_6 \theta_{CH^*} \theta_{H^*} - k_{-6} \theta_{CH_2^*} \theta_v$
7) $r_{CH_2\ hydr,dehydr}$	$CH_2^* + H^* \leftrightarrows CH_3^* + *$	$r_{CH_2} = k_7 \theta_{CH_2^*} \theta_{H^*} - k_{-7} \theta_{CH_3^*} \theta_v$
	Methane formation	
8) $r_{CH_4\ formation}$	$CH_3^* + H^* \leftrightarrows CH_4(g) + 2*$	$r_{CH_4} = k_8 \theta_{CH_3^*} \theta_{H^*} - k_{-8} P_{CH_4} \theta_v^2$
	H-assisted CO decomposition	
9) $r_{CO^{**}hydr,dehydr}$	$CO^{**} + H^* \leftrightarrows HCO^* + **$	$r_{CO} = k_9 \theta_{CO^{**}} \theta_{H^*} - k_{-9} \theta_{HCO^*} \theta_v$
10) $r_{HCO^*\ hydr,dehydr}$	$HCO^* + H^* \leftrightarrows CH^* + OH^*$	$r_{HCO} = k_{10} \theta_{HCO^*} \theta_{H^*} - k_{-10} \theta_{CH^*} \theta_{OH^*}$
	Water formation	
11) $r_{O\ hydr,dehydr}$	$O^* + H^* \leftrightarrows OH^* + *$	$r_O = k_{11} \theta_{O^*} \theta_{H^*} - k_{-11} \theta_{OH^*} \theta_v$
12) $r_{H_2O\ formation}$	$OH^* + H^* \leftrightarrows H_2O(g) + 2*$	$r_{H_2O} = k_{12} \theta_{OH^*} \theta_{H^*} - k_{-12} P_{H_2O} \theta_v^2$

In Model 3, the reaction paths starts from two different carbonyls species CO* and CO**. These two species are related to the presence of linear and bridged adsorbed CO over Ni/Al_2O_3[26] as discussed in chapter 1.

Figure 76 shows the regression results for Model 3:

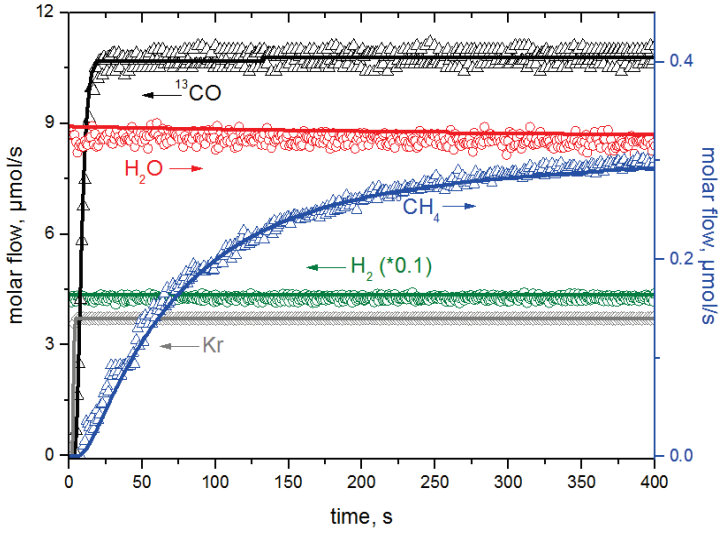

Figure 76: Regression results according to Model 2 at 210°C
Experimental (dots), Model (solid line)

Regression analysis of the SSITKA data at 210°C over Ni/Al_2O_3 with model 3, showed a better fit than either model 1 or 2. The improved fit of the $^{13}CH_4$ response is due to the 2 pathways involved simultaneously.

The better fit of the CO response, on the other hand is due to the appearance of two distinct CO species on the surface, here referred to as linear and bridged. Note that even for the bridged CO species a first order in the fraction of free sites as been adapted in the model (Table 36). Thus mathematically 2 adsorbed CO species are taken into account that not necessarily correspond to the IR-observed species. Moreover, note that model 3 has only one site balance. This is further quantified in Table 37, which shows the residual sum of squares, considered in Eq. 13 for all the experimental data at 210, 225 and 250°C for the three models.

Table 37: Residual sum of square for the studied models

Model	***RSS***
Model 1	$6.925 \cdot 10^3$
Model 2	$1.625 \cdot 10^3$
Model 3	$3.7 \cdot 10^2$

Table 37 shows that Model 3 results in a significant reduction of the sum of squares compared to Model 1 and 2, justifying the use of a more complex model.

As mentioned in the experimental results for the ^{13}C-labeling over $20\%Ni/\gamma\text{-}Al_2O_3$, plotting the decay of carbon ^{12}C content for the methane on a semi-logarithmic plot allows a better visual inspection of the 3 models and the experimental data, as shown in Figure 77.

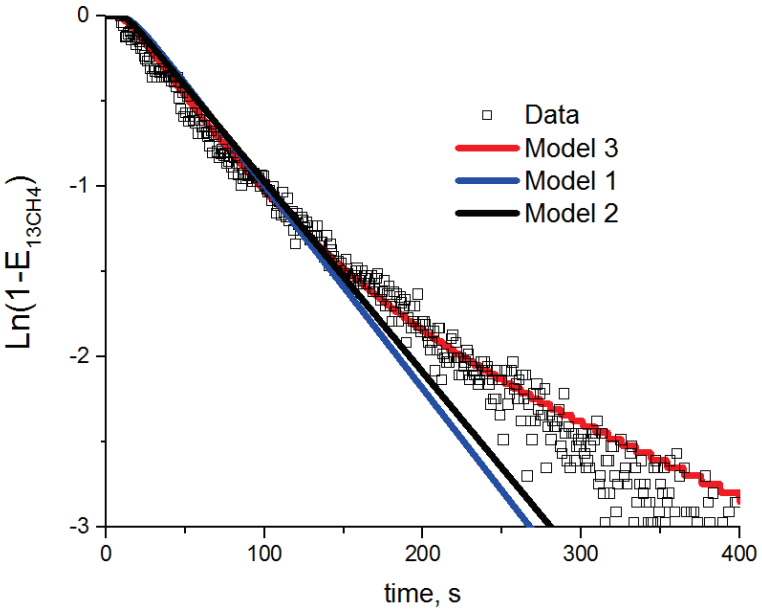

Figure 77: Fitting the decay of ^{12}C for the methane, T=210°C

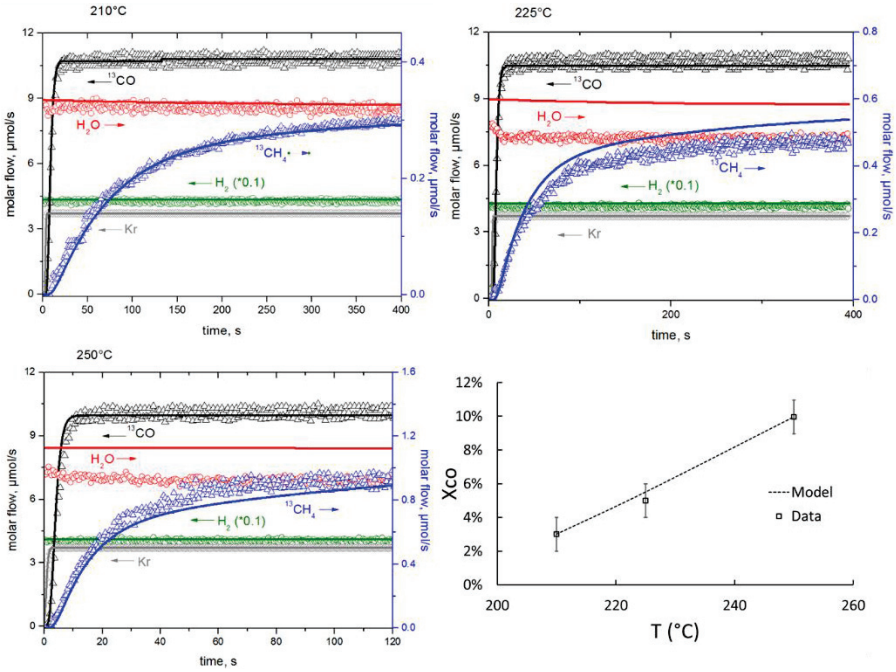

Figure 78: Fit of experimental responses at 210, 225 and 25°C at $H_2/CO=4$ Experimental (dots), Model (solid line)

A regression analysis of the SSITKA data at three temperatures (210, 225 and 250°C) was performed simultaneously based on model 3. Only the activation energies of the forward rates were optimized, keeping the rate at the reference temperature of 210°C constant (see Eq. 24)

Figure 78 shows the comparison between the model and experimental SSITKA responses. An adequate description of all responses is observed, except for the water production, which is overestimated by the model by 20%. This might be due to an error in the water calibration factor.

Table 38 compares the surface coverages calculated by the model and those obtained by integrating the SSITKA responses, as described in chapter 2.

Table 38: Comparison between estimated and calculated coverages of CO* and CH_x* species

	Model		**Experimental**	
T (°C)	θ_{CO}	θ_{CHx}	θ_{CO}	θ_{CHx}
210	0.48	0.22	0.56	0.17
225	0.38	0.21	0.39	0.26
251	0.21	0.18	0.31	0.23

The model shows a fairly good agreement for the estimation of surface coverages. Like the experimental values, the calculated θ_{CO} values decrease with increasing temperature. The calculated θ_{CHx} also slightly decreases with increasing temperature.

The H surface coverage (θ_H) is about 5% for all the three temperatures, this could be explained by the higher molar flow of H_2O calculated by the model, this lead to a higher consumption of hydrogen especially at 225°C and 250°C.

5.1.2 Parameter estimation

Preliminary modeling exercises showed that the CO adsorption, both linear and bridges and the hydrogen adsorption were at pseudo-equilibrium. This was deduced from the fact that the value of the ratio of the forward rate and reverse rate was very close to 1. For these three steps only an equilibrium constant can be estimated, consisting of a pre-exponential factor (entropy contribution) and an adsorption enthalpy. It was also found that the hydrogen and carbon monoxide adsorption were correlated. The hydrogen adsorption equilibrium constant was therefore fixed at the value obtained from the hydrogen adsorption experiments.

Although transient experiments allow estimating the number of active sites involved in the reaction, the value of this parameter was also fixed at the value determined by CO adsorption. For all the other steps in the mechanism of Table 36, only the forward rate constant and activation energy could be estimated, because the reaction conditions are far from thermodynamic equilibrium and thus the backward rates will have little impact on the production rate of methane and water.

As shown in the first part of this chapter the regression analysis of the SSITKA data was performed in two stages. First the rate constants were estimated at 210°C. Then the activation energies and adsorption enthalpies were estimated by a regression analysis of all SSITKA data at three temperatures simultaneously.

Table 39 shows the parameter values and their 95% confidence intervals.

Table 39: Parameter estimates and their 95% confidence interval
*Estimated from H_2 chemisorption measurements

Step #	Reaction	k^0_f (s^{-1}) 210°C / K^0 (bar^{-1}) or (-)	k^0_b (s^{-1}) 210°C	E_f (kJ mol^{-1})	E_b (kJ mol^{-1})
1	CO(g)+*⇄CO*	**4.0 ± 1.6 10^2**		0	**70 ± 38**
2	CO(g)+**⇄ CO**	**1.0 ± 0.5 10^2**		0	**78 ± 48**
3	H_2+2*⇄2H*	2 10^2 , fixed*		0	74, fixed*
4	CO*+*⇄C*+O*	**23 ± 15**	44.8	**97.3 ± 75.2**	33.4
5	C*+H*⇄CH*+*	**1.7 ± 0.9**	1.6 10^{-4}	0	68.3
6	CH*+H*⇄CH_2*+*	**4.4 ± 1.8**	4.1 10^{-5}	**71.4 ± 75.3**	96
7	CH_2*+H*⇄CH_3*+*	**0.2 ± 0.1**	8.8 10^{-4}	**104 ± 34**	54.5
8	CH_3*+H*⇄CH_4(g)+2*	**96 ± 80**	3.0 10^{-3}	**49.4 ± 53.1**	106.0
9	CO**+H* ⇄HCO*+**	**0.1 ± 0.03**	1.0 10^{-9}	**139.3 ± 59.0**	0
10	HCO*+H*⇄CH*+OH*	**0.05 ± 0.02**	2.2 10^{-6}	**36.6 ± 16.4**	104
11	O*+H*⇄OH*+*	**80 ± 4**		**80.6 ± 69.7**	8
12	OH*+H*⇄H_2O(g)+2*	**1.9 ± 0.7 10^3**		**80.6 ± 51.4**	36

Table 39 reports the parameter estimates with their corresponding 95% confidence intervals for the regression analysis at 210°C. All parameters have been estimated at significant statistical level, i.e. with rather narrow confidence intervals. Table 40 gives the binary correlation coefficients for all parameters estimated at 210°C. No strong correlation between the parameters have been observed, the highest value amounts to 0.79.

Table 40: Binary correlation coefficients of the parameter estimates for forward pre-exponential factors, k_f^0 at 210°C

	k_1	k_2	k_4	k_5	k_6	k_7	k_8	k_9	k_{10}	k_{11}	k_{12}
k_1	**1.00**										
k_2	0.02	**1.00**									
k_4	-0.11	0.39	**1.00**								
k_5	0.30	0.45	-0.01	**1.00**							
k_6	-0.72	0.10	0.10	-0.12	**1.00**						
k_7	0.53	0.22	0.32	0.05	-0.38	**1.00**					
k_8	0.20	0.50	-0.04	0.18	-0.13	-0.36	**1.00**				
k_9	0.48	0.44	0.01	-0.04	-0.31	0.55	0.40	**1.00**			
k_{10}	0.67	0.35	-0.32	0.35	-0.45	0.27	0.53	0.75	**1.00**		
k_{11}	0.21	0.69	0.09	0.01	-0.10	0.07	0.71	0.59	0.37	**1.00**	
k_{12}	0.42	0.59	0.12	0.03	-0.20	0.26	0.65	0.79	0.74	0.66	**1.00**

Although in the second stage of the regression analysis only the activation energies and adsorption enthalpies were adjusted, the statistical analysis was performed on both the pre-exponential and energy terms. Moreover, the energy parameters were bounded by thermodynamic constraints, see section 5.1.3.

From the analysis of the binary correlation coefficient matrix (not shown here due to space restrictions) no strong correlation between the optimized parameters was found.

In Table 39 only the activation energies of step 6 and 8 are the parameters that could not be estimated with significant confidence intervals. In the case of the activation energy of step 8 this is due to the fact that this step is after the rate-determining step and should be lumped with the preceding steps. After doing so, the statistical analysis has to rerun.

To provide a thermodynamic consistent model, by applying the principle of microscopic reversibility the backward activation energy was expressed with Eq. 25:

$$\overleftarrow{E}_{b,i} = \vec{E}_{f,i} - \Delta H^{\circ}_{R,surf,i}$$

Eq. 25

Where:

$\vec{E}_{f,i}$ is the forward activation energy in kJ/mol of elementary step i

$\overleftarrow{E}_{b,i}$ is the backward activation energy in kJ/mol of elementary step i

$\Delta H^{\circ}_{R,surf,i}$ is the enthalpy of surface reaction of elementary step i

The enthalpy of surface reaction is calculated following the Born-Haber thermodynamic cycle shown in Figure 79:

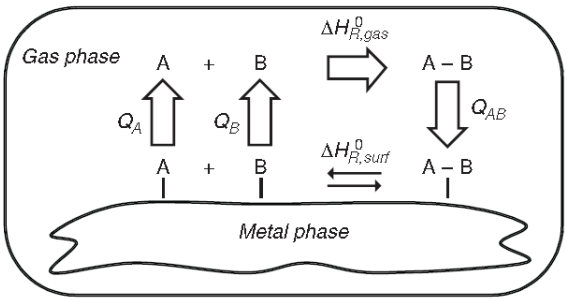

Figure 79: Born-Haber thermodynamic cycle used to estimate the enthalpy of surface reaction $\Delta \boldsymbol{H}^{\circ}_{\boldsymbol{R,surf,i}}$, for an elementary step i

And using Eq. 26 :

$$\Delta H^{\circ}_{R,surf,i} = \Delta H^{\circ}_{R,gas,i} - \sum_{k}^{prod} \vartheta_k Q_k + \sum_{j}^{react} \vartheta_j Q_j$$

Eq. 26

Where:

$\Delta H^{\circ}_{R,surf,i}$ is the enthalpy of surface reaction of elementary step i

$\Delta H^{\circ}_{R,gas,i}$ is the enthalpy of gas phase reaction the elementary step i

Q_k are the adsorption enthalpies of the product of the elementary step i

Q_j are the adsorption enthalpies of reactants in the elementary step i

To apply thermodynamic consistency to our microkinetic model, the heat of adsorption of all surface species involved in the surface mechanism needs to be estimated. In our case we used two methods to calculate the heat of adsorbed intermediates compounds, one is the scaling properties for adsorption energies proposed by Nørskov et al.[133] for hydrogen containing molecules obtained by DFT calculation, and the second was the UBI-QEP method developed by Shustorovich and Sellers[72] and applied to Fischer-Tropsch microkinetic modeling over Co-based catalyst by Blanco et al[49], Storsæter et al. [74] and Van Belleghem et al.[75].

The scaling properties method was used to determine the heat of adsorption of CH_x*, with x=1, 2, 3 and OH* species from the linear relation in Figure 80

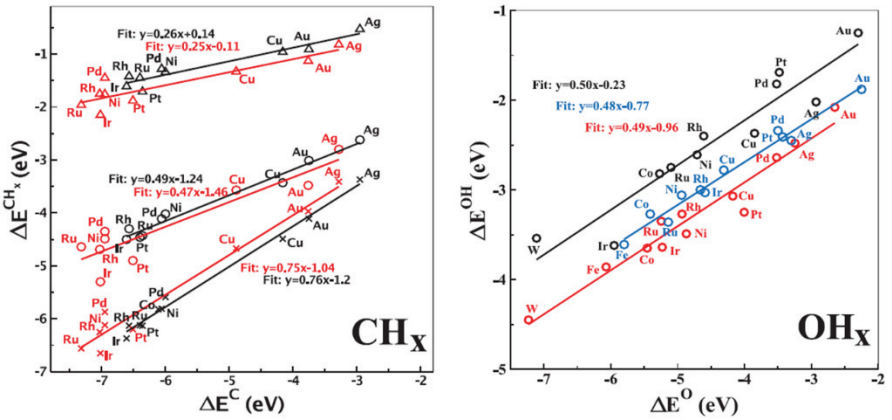

Figure 80: Adsorption energies of CHx intermediates (crosses: x = 1; circles: x = 2; triangles: x = 3) and OH plotted against adsorption energies of C and O respectively. The data points represent results for close-packed (black) and stepped (red) surfaces on various transition-metal surfaces[133].

For less studied compounds, like HCO*, which thermodynamic properties are not often available, the UBI-QEP method was used to calculate the heat of adsorption.

The method relates the chemisorption enthalpy of a gas phase species to a limited set of parameters, i.e., gas phase molecular bond energies, D_{AB}, and atomic chemisorption enthalpies, Q_A. The first set of parameters can be readily obtained from open databases [134] while the second set is estimated from specific formulas (see Appendix 3) that take in to count the strength of the molecule-metal bond[49,72,74]. Moreover in this formula are required the atomic chemisorption enthalpy of reactants that in our case are H, C and O.

In conclusion, the activation energies of the forward elementary steps are considered as adjustable model parameters. The reverse activation energies are obtained by applying the principle of microscopic reversibility.
For this, the chemisorption enthalpy of the surface species is calculated by means of the UBI-QEP and scaling properties methods. The atomic chemisorption enthalpy of H, C and O required in the latter method are considered as adjustable model parameters.

Estimation of activation energies will be shown and discussed in the following section focusing on the comparison of the activation energy values of the direct CO* dissociation and the hydrogenation of CO*, and to relate that to the literature on nickel and cobalt for the methanation and Fischer-Tropsch reactions.

5.1.3 Activation Energies

Table 41 shows the chemisorption enthalpies of H, C and O used in this study as input for the UBI-QEP and scaling properties methods:

Table 41: Chemisorption enthalpies of H, C and O.

	Q_i, kJ/mol
H	255
C	545
O	535

The value for the adsorption enthalpy of atomic H, Q_H was chosen in the center of the range determined by ab initio calculations, i.e., from 221 kJ mol^{-1} to 282 kJ mol^{-1}, depending on the CO coverage [40]. This value is also close to the UBI-QEP value reported by Shustorovich and Bell[73] for Ni(111).

Ojeda et al [40] report that the Q_C, for clean plane Co(0001) surface, could vary from 541 kJ mol^{-1} to 647 kJ mol^{-1} depending the CO coverage. The value of 545 kJ mol^{-1} used in this study was calculated from the linear CO adsorption enthalpy and is close to the value of 541 kJ mol^{-1} reported for θ_{CO}=0.5.

Finally for the enthalpy of oxygen chemisorption was chosen a value close to those estimated by Blanco et al [49] and Van Belleghem et al [75].

Once the chemisorption enthalpies of H, C and O are available it is possible to calculate the enthalpy of surface reaction by using Eq. 25.

This then allows calculating the reverse activation energies, as shown in Table 39. We stress again that the values of these activation energies

have no effect on the model fit of the data at 210,225 and 250°C. This would only be of importance to predict the performance of the model at higher temperatures where the reverse reaction becomes more significant. However, it provides bounds for the activation energies, which lead in the case of step (5) to a value of the forward activation energy of 0 kJ/mol.

As already shown in section 1.4.1 Derrouiche and Bianchi[26] report CO heat of adsorption values for linear and bridged adsorbed CO over Ni/Al_2O_3 catalyst. Through adsorption/desorption IR measurement they estimated a heat of adsorption for linear CO of 153-100 kJ/mol and for the bridged adsorbed CO of 147-106 kJ/mol. Calorimetry experiments on well-defined Ni crystals report value for the CO adsorption between 130-100 kJ/mol[135,136,137].

Bartholomew[138] reviewed hydrogen adsorption on Ni, Co and Fe. Over Ni hydrogen adsorbs dissociatively with a 1:1 Ni:H stoichiometry. Heat of adsorption is in the range of 70 -125 kJ/mol over Ni supported catalysts.

As mentioned in chapter 1, the CO dissociation mechanism is strongly debated. The result of the parameter estimation (Table 39) shows that the activation energy for the unassisted CO dissociation (step 4) is lower than the activation energy for the hydrogenation of adsorbed CO** (step 9). This result does not match the computational results over Co and Ni catalyst which report that the lowest DFT-derived[139] barrier for the direct CO dissociation is typically on the order of 140-150 kJ mol^{-1} over terrace sites. Ge and Neurock[139] on the other hand reported a CO dissociation barrier of 89 kJ/mol over corrugated surfaces involving steps and kinks. H-assisted CO dissociation is often considered as a way to increase the rate of CO bond scission with a reported activation barrier of 123 kJ mol^{-1}[139, 68].

The study of Weststrate et al.[141] supports that experimental temperature programmed photoemission data over a well-defined single Co (0001) crystal show an activation energy for the CO dissociation of 90-105 kJ mol^{-1}, our value of 97.3 kJ mol^{-1} found good agreement in the Weststrate's range.

Klinke and Broadbelt[142] found a value for the CO dissociation of 78 kJ mol^{-1} for Co(0001)and Ni(111).

Once the CO is dissociated in C* and O* the two atoms are hydrogenated to CH_4 and H_2O, the highest activation energy found was

for the hydrogenation step CH_2*+H*⇄CH_3*+* and moreover the activation barrier for the hydrogenation of C* is found to be low and to not be a limiting step in F-T/methanation conditions.

Table 42 shows a comparison of the activation energy of step 5-7:

Table 42: Forward activation energies for hydrogenation of CH_x species, comparison of this study with values from Gong et al.[143] and Van Belleghem et al.[75].

Surface reaction	$E_f, kJ/mol$		
	This study	**Gong et al.[143]**	**Van Belleghem et al.[75]**
C*+H*⇄CH*+*	0	81.6	79.0
CH*+H*⇄CH_2*+*	71.4	63.0	10.4
CH_2*+H*⇄CH_3*+*	104.0	60.0	63.3

Looking at the activation energy of the CO** hydrogenation (step 9, Table 39) the estimated value of 139.3 kJ mol^{-1} is in good agreement with the value reported by Ojeda et al.[40] by means of DFT calculation on Co(0001) and to the value reported by Azady et al. [45] of 128.1 kJ mol^{-1}.

For the last two steps, step 11 and 12, that are responsible of H_2O production, the estimated value of 80.6 kJ mol^{-1} and 82.6 kJ mol^{-1} respectively, are reasonably close to the values respectively of 100 kJ mol^{-1} and 114 kJ mol^{-1} computed by Balakrishnan et al[144] for the same microkinetic steps over Co(0001). Moreover Azadi et al[45] report a forward activation energy for the O*+H*⇄OH*+* step of 86.2 kJ mol^{-1}

5.1.4 Contribution analysis

Figure 81 shows the ^{12}C decay on a semi-logarithmic plot for the methane production at the three investigated temperatures. At all three temperatures a dual path can be distinguished, although due to the faster kinetics at higher temperatures this becomes less visual with increasing temperature.

To further quantify the contribution of each pathway to the overall methane production, a contribution analysis is performed on the data fit for the 3 different temperatures, 210, 225 and 251°C.

Two ratios are defined φ_{CO^*} and $\varphi_{CO^{**}}$:

$$\varphi_{CO^*} = \frac{-r_{CO^*}}{(-r_{CO^*}) + (-r_{CO^{**}})}$$

$$\varphi_{CO^{**}} = \frac{-r_{CO^{**}}}{(-r_{CO^*}) + (-r_{CO^{**}})}$$

These ratio are related to the two carbonyl species present in Model 3 and for example, φ_{CO^*} is computed as the rate of consumption of CO* divided all the rates that reacts with CO at the surface (CO*+CO**).

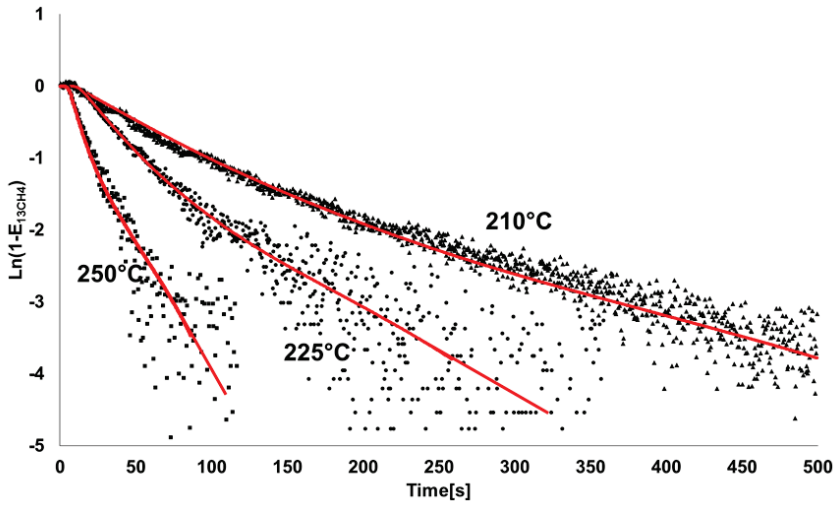

Figure 81: Fitting the decay of ^{12}C for the methane for different temperatures

Table 43: Contribution analysis for Model 3 at 210, 225 and 251°C

T[°C]	φ_{CO^*},Direct CO dissociation	$\varphi_{CO^{**}}$,H-assisted CO decomposition
210°C	79%	21%
225°C	75%	25%
251°C	70%	30%

Table 43 shows how most of methane is produced by the direct CO dissociation while only the 20-30% is produced by the H-assisted decomposition path. An interesting result is that increasing the temperature the route that involves the CO** carbonyl species became more and more relevant. This behavior reflects a slow reactivity of surface species CO** due to a higher activation barrier than the CO* scission in C* and O*.

5.1.5 Degree of rate control analysis and surface species concentration

Campbell's degree of rate control [148,149] (DRC) was applied to the methane and water formation at steady-state according to the third reaction mechanism with the final parameter values in Table 39.

This method is used in microkinetic models to evaluate the degree to which reaction steps are rate-controlling. This is accomplished by increasing both forward and reverse rate constants for the specific step and calculating the resulting fractional increase in the overall rate, as expressed in the following equation (Eq. 27)

$$X_{RC,i} = \frac{k_i}{r}\left(\frac{\partial r}{\partial k_i}\right)_{k_{j\neq i},K_i} = \left(\frac{\partial \ln r}{\partial \ln k_i}\right)_{k_{j\neq i},K_i}$$

Eq. 27

Where the partial derivative is taken holding constant the rate constants, k_j, for all other steps $j \neq i$ and the equilibrium constant, K_i, for step i.

The larger the numeric value of $X_{RC,i}$ is for a given step, the bigger is the influence of its rate constant on the overall reaction rate r. A positive value indicates that increasing k_i will increase the net rate r, and such steps are termed rate-limiting steps (RLS). A negative value indicates the opposite, and such steps are termed inhibition steps.

Table 44 lists the results.

Table 44: Campbell's degree of rate control at 210°C for SSITKA experiment over 20%Ni/γ-Al_2O_3

Step #	Reaction	Degree of rate control	
		CH_4	H_2O
1	CO+*⇄CO*	0	0
2	CO+**⇄CO**	0	0
3	H_2+2*⇄2H*	0.01	0.01
4	CO*+*⇄C*+O*	0.01	0.01
5	C*+H*⇄CH*+*	0.21	0.21
6	CH*+H*⇄CH_2*+*	0.02	0.02
7	CH_2*+H*⇄CH_3*+*	0.39	0.37
8	CH_3*+H*⇄CH_4+*	0	0
9	CO**+H*⇄HCO*+**	-0.30	-0.27
10	HCO*+H*⇄CH*+OH*	0.43	0.38
11	O*+H*⇄OH*+*	0.26	0.25
12	OH*+H*⇄H_2O+2*	0	0

The DRC analysis shows that the methane production could not be reduced to one single rate-limiting step. Table 44 shows that already in the first reacting pool, the stepwise hydrogenation of C*, there are two steps #5 and #7 that govern the methane formation rate, as well as the step #10 that reflects the slower reactivity of HCO* adsorbed species.

The step #11 has a strong influence on both methane and water formation. In fact both OH_y* and CH_x* species both compete for H* and the reactions are strongly coupled.

Our microkinetic model provides also the surface coverages of all the intermediates species.

Figure 82 shows the surface concentration profiles as a function of time:

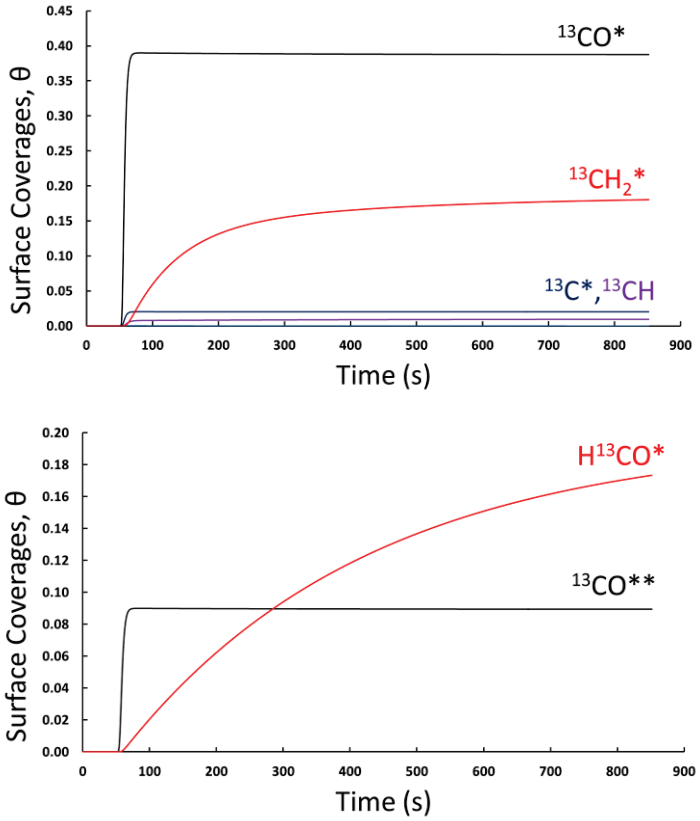

Figure 82: Surface coverages of reacting intermediates for both reacting paths Top: Direct CO dissociation, Bottom: H- assisted CO decomposition T=210°C, $H_2/CO=4$

Figure 82 shows that after the isotopic transient the most abundant CH_x* intermediate species are the CH_2*, the low value of coverages for C* and CH* suggest that the first and second hydrogenation of C* are fast compared to the hydrogenation of CH_2* to CH_3*. This results is in agreement with the work of Visconti et al.[44]. In this work the authors

found a surface coverage for CH_2* species of 30% over a Co/Al_2O_3 at typical Fischer-Tropsch condition.

Figure 82 shows also how the buildup time for the HCO* species is high, this result reflects again the higher energy barrier that the CO** carbonyl specie has to overcame to form CH*.

5.2 Modeling Step transient experiments

5.2.1 Step-transient experiment over 20%Ni/γ-Al_2O_3

The experimental step-response data over 20%Ni/γ-Al_2O_3 were also modeled. Only the data at 210°C were used for the modeling study.

The first model explored was based on the model proposed by Alstrup[131], similar to model 1 in the previous part. Underwood and Bennett[150] also proposed this reaction mechanism based on qualitative analysis of transient experiments. All the steps that were initially considered are given in Table 45.

Table 45: Rate expression for the elementary steps considered for step-transient modeling

Reaction		Rate expression
	Elementary reaction	
	Reactant adsorption	
1) $r_{CO\ chemsorption,desorption}$	$CO(g) + * \leftrightarrows CO^*$	$r_{CO} = k_1 P_{CO} \theta_v - k_{-1} \theta_{CO^*}$
2) $r_{H_2\ chemsorption,desorption}$	$H_2(g) + 2* \leftrightarrows 2H^*$	$r_{H_2} = k_2 P_{H_2} \theta_v^2 - k_{-2} \theta_{H^*}^2$
	Initiation reaction	
3) $r_{CO^*\ diss,ass}$	$CO^* + * \leftrightarrows C^* + O^*$	$r_{CO} = k_3 \theta_{CO^*} \theta_v - k_{-3} \theta_{C^*} \theta_{O^*}$
4) $r_{C\ hydr,dehydr}$	$C^* + H^* \leftrightarrows CH^* + *$	$r_C = k_4 \theta_{C^*} \theta_{H^*} - k_{-4} \theta_{CH^*} \theta_v$
5) $r_{CH\ hydr,dehydr}$	$CH^* + H^* \leftrightarrows CH_2^* + *$	$r_{CH} = k_5 \theta_{CH^*} \theta_{H^*} - k_{-5} \theta_{CH_2^*} \theta_v$
	Methane formation	
6) $r_{CH_4\ formation}$	$CH_2^* + 2H^* \leftrightarrows CH_4(g) + 3*$	$r_{CH_4} = k_6 \theta_{CH_2^*} \theta_{H^*} - k_{-6} P_{CH_4} \theta_v^2$
	Water formation	
7) $r_{O\ hydr,dehydr}$	$O^* + H^* \leftrightarrows OH^* + *$	$r_O = k_7 \theta_{O^*} \theta_{H^*} - k_{-7} \theta_{OH^*} \theta_v$
8) $r_{OH\ hydr,dehydr}$	$OH^* + H^* \leftrightarrows H_2O^* + *$	$r_O = k_8 \theta_{OH^*} \theta_{H^*} - k_{-8} \theta_{H_2O^*} \theta_v$
	Water desorption	
9) $r_{H_2O\ adsorption,desorption}$	$H_2O^* \leftrightarrows H_2O(g) + *$	$r_{H_2O} = k_9 \theta_{H_2O^*} - k_{-9} P_{H_2O} \theta_v$
10) $r_{OH\ on\ alumina}$	$OH^* + \# \leftrightarrows OH^{\#} + *$	$r_{OH^{\#}} = k_{10} \theta_{OH^*} \theta_{v\#} - k_{-10} \theta_{OH^{\#}} \theta_{v*}$

Initial regression analysis showed that the route for the methane formation (steps (1)-(6), Table 45) permitted an adequate model fit of

the methane step-response. Note that step (6) is not an elementary step, but a combination of 2 steps. The underlying assumption is that these steps are fast, taking place after the rate-determining step and that the rate constants cannot be estimated without lumping the steps together. The parameter estimation presented later shows that this is indeed the case. The rates of all the steps, except step (6) were calculated by using the law of mass action, which directly applies to the elementary steps. The rate of step (6) was calculated as:

$$r_{6,CH_4} = k_6 \theta_{CH_2^*} \theta_{H^*} - k_{-6} P_{CH_4} \theta_v^2$$

Thus a first order with respect to the hydrogen coverage, just like the other hydrogenation steps (4) and (5).

The route for the formation of water was modified significantly. In the previous study the formation of water was given by two steps (11-12, Table 36)

The long time delay on the water response at 210°C (Figure 55) suggested that more than one surface species might be involved in the formation of water. Table 45 therefore contains several elementary steps with different surface intermediates (steps 7-10). This path showed that steps involving the support sites were needed for an adequate description of the water production (steps 9-10).

Water can interact with certain oxide based supports, either in the form of physisorbed water or in the form of hydroxyl groups. Under steady-state operating conditions, these interactions do generally have no effect on the overall kinetics, but they need to be taken explicitly into account during step-response experiments, as they will influence the transient response. For example, the larger the sorption capacity of a catalyst the more the water response will be delayed in time. This evidence is clearly shown by comparing the same step–transient experiments on 20%Ni/γ-Al_2O_3 and 10%Ni/SiC.

5.2.2 Methane Formation

Looking to the methane production it shows an overshoot, this is related to the fact that before the switch the surface concentration of adsorbed hydrogen was higher than under methanation conditions, as the catalyst was exposed to hydrogen gas only. Although the partial pressure of hydrogen in the gas mixture remained constant before and after the switch, the CO competes with hydrogen for nickel adsorption sites, leading to a lower hydrogen coverage under steady-state methanation than during hydrogen adsorption. The methanation reaction has a reaction order with respect to hydrogen close to 1. Thus an increased in the hydrogen coverage will lead to an increased methane formation. This will continue until the hydrogen coverage has dropped to the values corresponding to steady-state conditions. Indeed, simulations showed that the model with a slow CO dissociation step was not able to correctly fit the methane step-response, as shown in Figure 83. The rate-determining step must be one of the hydrogenation steps after the CO dissociation.

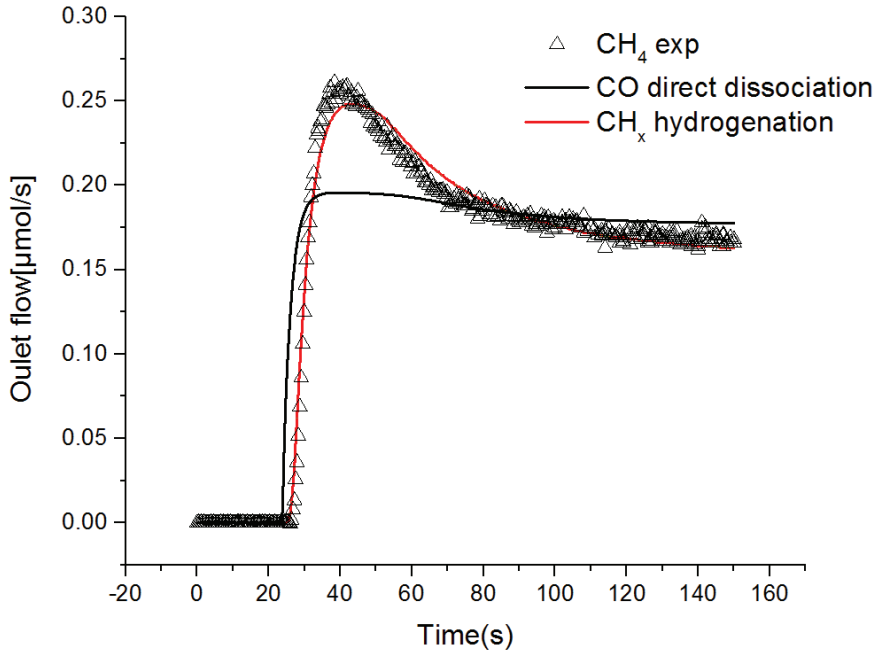

Figure 83: Methane step-response at 210°C (symbols) compared to the model (lines) with CO* dissociation (black) and CH_x hydrogenation (red) as rate-determining step.

5.2.3 Water formation

To model the water step-response a combination of steps (7) – (9) were used. The best fit was the red curve shown in Figure 84.
The model response does not have the same slope as the experimental water response. Using steps (7)-(9) the water response can be further delayed but the slope of the curve cannot be changed.
Comparing the model fit, the red curve in Figure 84 and the experimental response, suggest that a small amount of water at the beginning of the transient has been irreversibly lost. This can be due to the dehydroxylation of the alumina support in the vicinity of the nickel particles during the exposure of the catalyst to hydrogen before the switch to methanation conditions.
During the methanation, the support is hydroxylated by the transfer of hydroxyl groups from the nickel to the vacancies on the alumina support (step (10) in Table 45). Considering this reaction step, leads to the blue model curve in Figure 84. It fits the experimental water response very well.

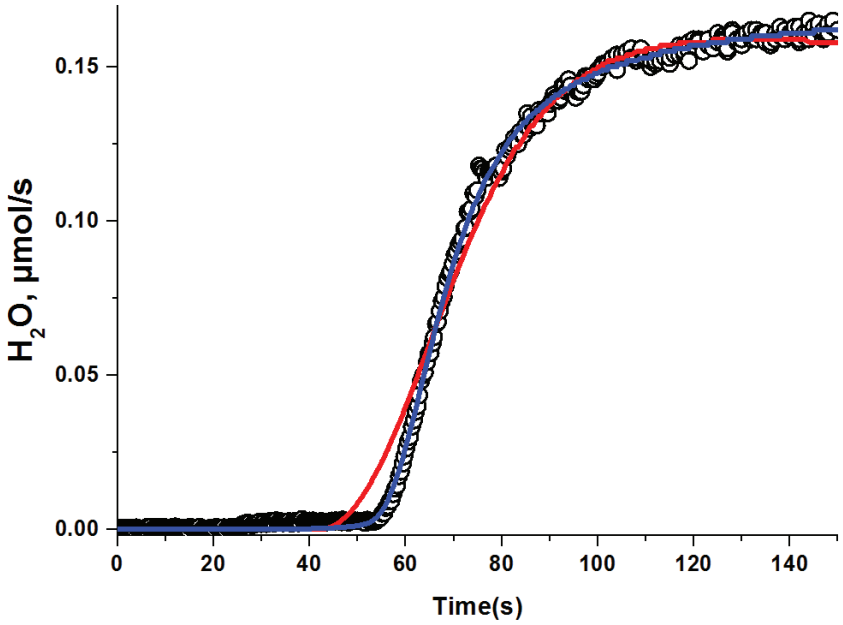

Figure 84: Water step-response at 210°C (symbols) compared to two different models Alumina hydroxylation (Blue), only water adsorption/desorption on Ni (Red)

5.2.4 Regression analysis and parameter estimation

Table 46 shows the results of regression analysis for all the elementary steps used to model the step-transient experiment.

Table 46: Reaction steps used for regression analysis. Values of the parameter estimates with their estimated 95% confidence interval from step response experiments at 210°C.

Step #	Reaction	A^0_f (s^{-1}) / K^0 (bar^{-1}) or (-)	A^0_b (s^{-1})	E_f (kJ mol^{-1})	E_b (kJ mol^{-1})
1	CO+*⇄CO*	**$1.59 \pm 0.07\ 10^{-11}$**		0	112
2	H_2+2*⇄2H*	$2.0\ 10^{-6}$, fixed*		0	74
3	CO*+*⇄C*+O*	**$9.3 \pm 0.7\ 10^{9}$**	$1.0\ 10^{7}$	90	45
4	C*+H*⇄CH*+*	**$5.6 \pm 1.6\ 10^{14}$**	$1.0\ 10^{8}$	110	98
5	CH*+H*⇄CH_2*+*	**$1.40 \pm 0.03\ 10^{10}$**	$1.0\ 10^{5}$	109	49
6	CH_2*+2H*⇄CH_4+3*	$7.5\ 10^{12}$	$1.0\ 10^{4}$	90	60
7	O*+H*⇄OH*+*	**$1.27 \pm 0.08\ 10^{9}$**	$1.0\ 10^{3}$	99	40
8	OH*+H*⇄H_2O*+*	**$8.9 \pm 0.8\ 10^{9}$**	$1.0\ 10^{3}$	99	40
9	H_2O*⇄H_2O+*	**$1.32 \pm 0.3\ 10^{5}$**		70	0
10	OH*+#⇄OH#+*	**$1.6 \pm 1\ 10^{10}$**		70	0

Figure 85 shows the fit of experimental data with the parameter values listed in Table 46.

Only the responses of CO, CH_4 and H_2O were used for parameter estimation. The Ar response was fitted to describe the switching valves dynamics correctly (Heaviside function). The hydrogen response was calculated from the microkinetic model and shown here for comparison. An excellent fit of all step responses is obtained, with only a slight deviation for the model of the methane step-response.

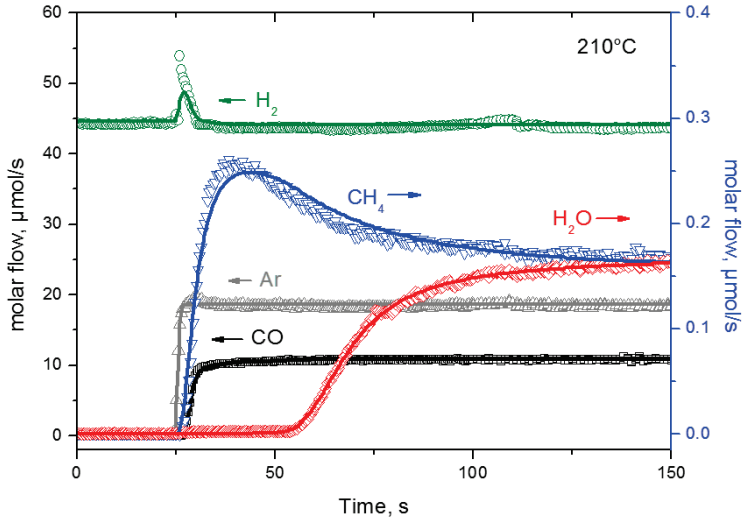

Figure 85: Regression results of step-transient experiments over 20%Ni/γ-Al_2O_3 (open symbols) and model fits (solid lines) at 210 °C.

5.2.5 Degree of rate control analysis

As for the SSITKA experiments to complete the study for the step-transient responses over the 20%Ni/γ-Al_2O_3 a degree of rate control analysis, was applied to the methane and water formation at steady-state according to the above reaction mechanism with the final parameter values.
The results are listed in Table 47:

Table 47: Campbell's degree of rate control at 210°C for step-transient experiment over 20%Ni/γ-Al_2O_3

Step #	Reaction	Degree of rate control	
		CH_4	H_2O
1	CO+*⇄CO*	0.00	0.00
2	H_2+2*⇄2H*	0.00	0.00
3	CO*+*⇄C*+O*	-0.29	-0.34
4	C*+H*⇄CH*+*	-0.11	-0.12
5	CH*+H*⇄CH_2*+*	0.90	0.31
6	CH_2*+2H*⇄CH_4+3*	0.04	0.01
7	O*+H*⇄OH*+*	0.25	0.88
8	OH*+H*⇄H_2O*+*	0.11	0.30
9	H_2O*⇄H_2O+*	0.00	0.00
10	OH*+#⇄OH#+*	0.00	0.00

The rate-controlling step for the methane formation is step (5) although other steps contribute significantly. The rate-controlling step for the water formation is step (7) even if other steps contribute significantly.

5.2.6 Surface coverage

Figure 86 shows the calculated surface coverages on nickel as a function of time. The hydroxyl groups on the support are not shown in Figure 86. CH* and O* are the most abundant surface species, followed by H*, CO* and OH*.
All CHx species with x>1 have negligible coverages in agreement with the fact that these species are formed after the rate-determining step, which is the hydrogenation of CH* species. The concentration of adsorbed water is very low, well below 1%. There is no C* on the surface.
The high values of O* are likely to be due to the "slow" water formation. It is likely that water physisorbs on the alumina support, which is not explicitly taken into account in the above model. Additional step response experiments over Ni/SiC did indeed show a much faster step response of water.

To compare the calculated surface coverages to the experimental data, the overall C*, H* and O* atomic balances were calculated and compared in Figure 87 to the experimental ones. A fairly good comparison was found.

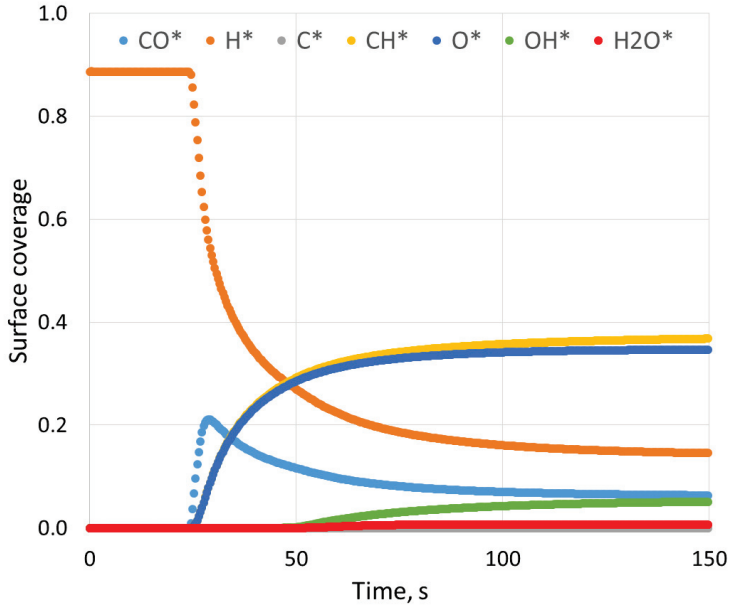

Figure 86: Calculated surface coverages corresponding to the step response experiments at 210 °C.

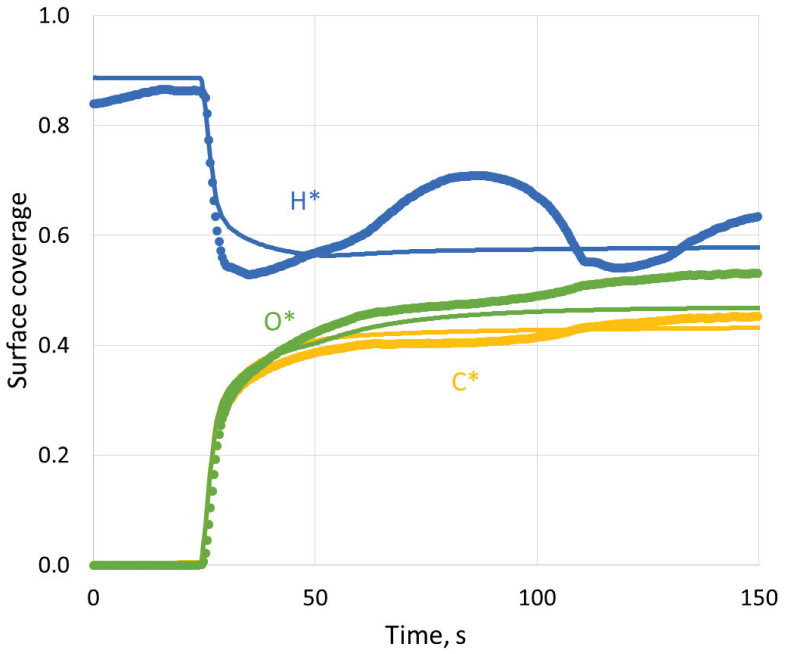

Figure 87: Atomic surface balances (open symbols) and model fits (solid lines) at 210 °C

5.2.7 Step-transient experiment over 10%Ni/SiC

To understand the role of support during methanation reaction the step-transient experiment performed over the 10%Ni/SiC at 225°C was modeled.

The starting model was the same used for the 20%Ni/γ-Al_2O_3 with the only difference that the formation of OH groups on the alumina support (step 10, Table 46) was not take into count for the 10%Ni/SiC.

Performing the analysis of the degree of rate control on the 10%Ni/SiC data, has shown that the hydrogenation of first carbon atoms is the most influencing step, so it was also possible to lump together the stepwise hydrogenation steps in one step C*+4 H* ⇄ CH_4 + 5*. The rate of this lumped step was still considered to be first order in hydrogen

Figure 88 compares the experimental data and the model simulations. A rather good description of the data is observed. Table 48 lists the degree of rate control results.

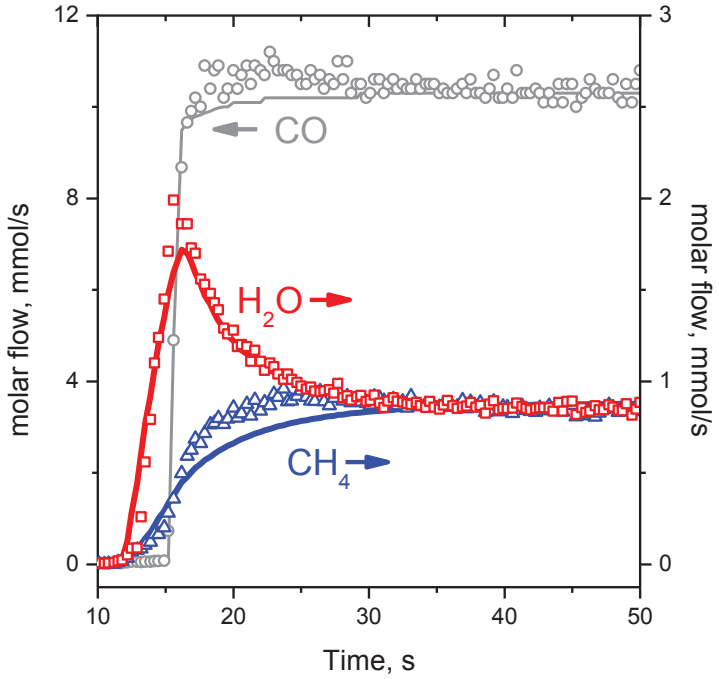

Figure 88: Regression results of step-transient experiments over 10%Ni/SiC (open symbols) and model fits (solid lines) at 225 °C.

Table 48: Campbell's degree of rate control at 225°C for step-transient experiment over 10%Ni/SiC

Step #	Reaction	Degree of rate control	
		CH_4	H_2O
1	CO+*⇄CO*	0.00	0.00
2	H_2+2*⇄2H*	0.00	0.00
3	CO*+*⇄C*+O*	0.07	0.07
4	**C*+ 4H*⇄CH_4+ 5***	**0.52**	**0.52**
5	**O*+2H*⇄H_2O + 3***	**0.38**	**0.38**
6	H_2O*⇄H_2O + *	0.00	0.00

The final model used to describe the 10%Ni/SiC reactivity consists of 6 steps, which kinetic parameters were optimized by means of regression analysis (Table 49).

Table 49: Parameter estimates and their 95% confidence interval for the 10%Ni/SiC *Estimated from H_2 chemisorption measurements

Step #	Reaction	A^0_f(s^{-1})	A^0_b(s^{-1})	E_f (kJ mol^{-1})	E_b (kJ mol^{-1})
1	CO(g)+*⇄CO*	**$1.7 \pm 0.2\ 10^4$**	10^{15}	0	112
2	H_2+2*⇄2H*	2 10^4, fixed*	10^{10}	0	74, fixed*
3	CO*+*⇄C*+O*	**$9.4 \pm 4.4\ 10^9$**	10^7	90	45
4	C*+4 H*⇄CH_4(g)+5*	**$1.9 \pm 0.5\ 10^{10}$**	10^8	110	98
5	O*+2H*⇄H_2O+3*	**$2.0 \pm 1.4\ 10^{12}$**	10^5	109	49
6	H_2O*⇄H_2O(g)+*	**$4.7 \pm 1.3\ 10^7$**	10^3	70	40

Comparing the coverages of surface species at steady-state (Table 50), it is possible to notice that the model gives values close the ones found with the assumption of low amount of oxygenates species on surface (OH_y) and atomic C* as the most abundant reacting intermediate.

Table 50: Experimental and model results for surface coverages at the steady-state for 10%Ni/SiC at 225°C

θ, Surface Coverage	Experimental CH_x, x=0	Model CH_x, x=0
H	0.65	0.6
CO	0.20	0.25
C	0.1	0.07
OH_y	<0.05	<0.01

5.2.8 Conclusions

In this chapter, the microkinetic modeling of SSITKA and step-transient experiments over 20%Ni/γ-Al_2O_3 and 10%Ni/SiC have been presented.

The surface heterogeneity of methane formation, shown by SSITKA experiment over 20%Ni/γ-Al_2O_3, have been successfully modeled using a two C-intermediates based microkinetic model. The two reacting paths leading to methane are assigned respectively to the direct CO dissociation and the H-assisted CO dissociation.

Performing a contribution analysis for the CO molecule, it is possible to quantify the amount of methane originating from the CO direct dissociation and the H-assisted path, which is temperature dependent.

By means of regression analysis 21 parameter for 12 elementary steps are optimized and then the value compared to recent literature study based on computational chemistry and microkinetic modeling, showing that, over 20%Ni/γ-Al_2O_3, the CO direct dissociation has a lower activation barrier than H-assisted CO activation.

Modeling the step-transient experiments on both alumina and silicon carbide supported Ni catalyst, has shown the relevance of water interaction with support.

The Campbell's degree of rate control analysis has shown different steps, as rate-limiting step, depending on the experiment modeled and on the support nature. However the conclusion of this analysis suggest that for the methane production a hydrogenation step is rate-limiting while for the water it is the hydrogenation of the O* on the surface.

Chapter 6

Conclusions and perspectives

Fischer-Tropsch synthesis is expected to play an increasing role to compensate the decreasing petroleum reserves. Methane is an undesired product of this synthesis. Understanding how methane is formed over FT catalyst is a first step in designing better catalyst, but also it helps in understanding the chain growth mechanism as the both are linked via the surface monomer species. The literature review indicates that there is an ongoing debate on the reaction mechanisms for syngas conversion over both nickel as cobalt.

Although the product distribution over these two catalyst is very different the key steady-state kinetic parameters are very similar: reaction orders for CO and H_2 are in the range of -1 to 0.5 and 0.5 to 2, respectively; apparent activation energies cover a range of 80-130 kJ/mol[56]. Transient kinetic experiments provide more detail on the methane reaction path, but again over Ni, Co and Fe catalysts very similar features are observed by numerous studies [47, 48, 50,77, 114]: two surface intermediates participate to the methane formation. Initial attempts to quantify the transient data allowed to predict the contribution of each pathway but did not reveal the nature of these intermediates [47,77]. Based on a kinetic isotope effect and DFT analysis, Yang proposed that these two surface intermediates correspond to CH_2O* and CH_x* [50].

Water is the main product of the FTS, but its pathway has not been studied in great detail. Transient studies over supported catalyst show slow production rates for water compared to methane, but surface science studies indicate a very fast water production[131,151].
The aim of this study is to get a better understanding of the methane pathway over nickel and cobalt catalysts. Therefore a microkinetic approach is used based on transient experimentation.

The kinetic investigation was performed over a 20%Ni/γ-Al_2O_3 catalyst, a 10%Ni/SiC catalyst and 15%Co/SiC catalyst in the range of temperature 210-250°C and P=1.2 bar. The methanation mechanism was investigated over the two Ni-based catalyst at H_2/CO ratio equal to 4 while over the Co-based sample the Fischer-Tropsch reaction was studied at a H_2/CO ratio equal to 2. However a high selectivity to methane (0.38-0.5) was found for the 15%Co/SiC.

The catalysts samples compared well in terms of activity (TOF) and steady-state performance to similar studies in literature.

To get detailed kinetic information both SSITKA and step-transient techniques have been used. The isotopic tracing was performed using ^{13}C, D_2 and ^{18}O over 20%Ni/γ-Al_2O_3 while only ^{13}C and ^{18}O over 15%Co/SiC, D_2 labeling was not performed over Co due to the complexity of Fischer-Tropsch reacting system and the presence of an inverse isotopic effect.

A qualitative interpretation of the ^{13}C-SSITKA results indicated that the catalyst surface was heterogeneous towards the formation of methane over both 20%Ni/γ-Al_2O_3 and 15%Co/SiC.

Also the D_2-labeling performed over the 20%Ni/γ-Al_2O_3 provided a similar conclusion concerning two H containing intermediates leading to methane.

^{18}O-labeling experiment showed on 20%Ni/γ-Al_2O_3 a strong interaction between water and the alumina support that prevented interpretation of the experimental data. This support effect was not observed over 15%Co/SiC, thus revealing a distribution of O-containing surface pools leading to H_2O in analogy to the C-pools leading to methane.

To investigate the support effect during methanation and Fischer-Tropsch reactions, step-transient experiment were performed over both alumina and silicon carbide supported catalysts. The experiments showed that the γ-Al_2O_3 leads to interaction with produced water causing, at 210°C, a delay of the transient response.

^{13}C SSITKA and step-transient results are investigated by means of microkinetic modeling. In the SSITKA microkinetic model over Ni/γ-Al_2O_3 the two surface C-intermediates leading to methane were associated with two reaction paths: the direct CO dissociation and the H-assisted CO dissociation. This approach resulted in a better fit of the experimental methane responses. Moreover, it was found that 2 different adsorbed CO species are present on the surface. With respect to IR studies, these species are referred to as linear and bridges carbonyls.

Regression analysis of the SSITKA data over the 20%Ni/γ-Al_2O_3 catalyst allowed estimation of the equilibrium constants for CO and H_2 adsorption and the forward rate constants of all other steps at a

statistical significant level. Including the data at 225 and 250°C allowed further estimation of the adsorption enthalpies and activation energies.

Inspection of the reaction mechanism showed that there is not a single rate-determining step, but rather several surface carbon hydrogenation steps are controlling the overall methane production. Different hydrogenation steps have been proposed in the literature[78,79,142,145,146] and no consensus has been reached.

In our study different hydrogenation steps have been identified as rate-determining step, according to the type of experiment (SSITKA vs Step-transient) or catalyst (Ni/Al_2O_3 vs. Ni/SiC).

A contribution analysis of the CO consumption for both reaction paths showed that 80% of the methane is produced via direct CO dissociation and 20% through the hydrogen assisted route. In agreement with the higher energy barrier for the H-assisted route compared to the direct CO dissociation (97 vs 139 kJ/mol), the former route contributes more at higher temperatures.

Although the microkinetic model was based on a single nickel active surface site (*), these two routes suggest the presence of two distinct surface sites. For a metal supported catalyst usual distinction between sites is either terrace vs. edge/kink site or metal site vs. metal/support interface sites. The 80/20 ratio from the contribution analysis would point in the direction of terrace vs. edge/kink sites, if one assumes similar TOF's for both sites.

Assuming a truncated octahedron particle shape, firstly proposed by Van Herdeveld et al.[147], it is possible to determine the coordination number of terrace's or edge's atoms and from this calculate the distribution of these two site on surface (Figure 89, Figure 90).

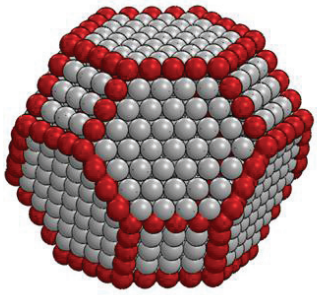

Figure 89: Truncated Octahedron particle shape, adapted from [147]

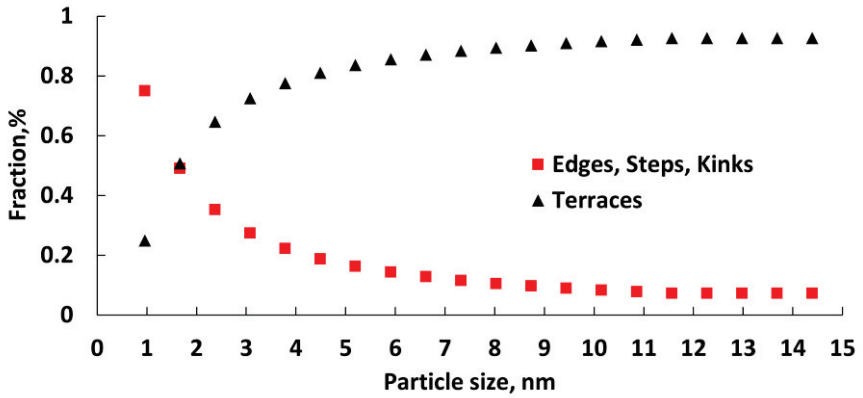

Figure 90: Statistics of surface atoms for a truncated octahedron, adapted from [147]

Figure 90 shows that for a catalysts particle with an average diameter between 5÷6 nm, as used in this study, the surface distribution of terraces and edges, steps and kinks corresponds 82/18, almost as the distribution of the two reaction routes.

These results then imply that the reactivity of CO hydrogenation to methane is related to the catalyst surface structure. Over nickel similar turnover rates have been reported for Ni(100) and Ni(111) as for supported catalysts, indicating that the reaction is not structure sensitive[131], while CO dissociation over nickel is structure sensitive[131, 152]. On the other hand the methane selectivity was found to depend on the particle size for cobalt particles below 6 nm[121]. According to the microkinetic model, the linear carbonyls species would then occupy terraces sites (80%) and undergo direct dissociation of CO into C* and O*, while the bridged carbonyl species are on the step/edge sites and need to be activated by hydrogen to dissociate in CH* and OH*. This is opposite to numerous DFT studies, both on nickel and cobalt, that indicate facile CO dissociation on step sites and hydrogen assisted CO dissociation on terrace sites [139, 152]. In the above analysis we assumed a similar TOF for both sites. However, it is likely that an edge is more reactive than a terrace site and that the TOF are very different. The *rates* obtained from the contribution analysis can then no longer be correlated to a *number* of sites. More experimental work over supported nickel catalysts with different nickel particles are necessary to better identify the two distinct sites.

This study showed that in order to study the rate of water formation, one should carefully consider the support properties. Supports that favor interaction in the form of water physisorption or hydroxyl formation should be avoided. During transient experiments these interaction will mask the important features of the water production. Thus by using a Ni/SiC and Co/Sic catalyst it was shown that for both catalysts water formation was much faster than methane formation.

Finally, several discrepancies have been found in modeling of SSITKA data or step-transient data. An adequate description of the step-transient responses was obtained using a single surface intermediate, while the SSITKA model was based on two intermediates. Preliminary regression analysis showed that introducing a second surface intermediate leads to an improved fit of the methane transient step response, but the fit of the water response became worse. More modeling effort is necessary to resolve these issues. Nevertheless, changing slightly the conditions or catalyst seems to impact at least the values of the rate parameters.

References

1. H. Pichler, H. Schulz, Chem.-Ing.-Tech. 42 (1970) 1162
2. F. Fischer, H. Tropsch, Brennstoff-Chemie 4 (1923) 276.
3. F. Fischer, H. Tropsch, Chem. Ber. 59 (1926) 830.
4. J. Schulze, Chem.-Ing.-Tech. 46 (1974) 976.
5. J.H. Gregor, Catal. Lett. 7 (1990) 317.
6. Keith, P.C., Gasoline from natural gas. Oil Gas Journal, 1946(45): p. 102-112.
7. Dry, M.E., Practical and theoretical aspects of the catalytic Fischer-Tropsch process.
8. M. E. Dry, “The fischer Tropsch Process - Commercial Aspect,” Catal. Today, vol. 9570, no. 6, pp. 183–206, 1990.
9. Guettel, R., U. Kunz, and T. Turek, Reactors for Fischer-Tropsch synthesis. Chemical Engineering & Technology, 2008. 31(5): p. 746-754.
10. Hoek, A. The Shell GTL process: Towards a World Scale Project in Qatar: the Pearl Project. in DGMK-Conference "Synthesis Gas Chemistry". 2006. Dresden.
11. Sie, S.T., Process development and scale up: IV. Case history of the development of a Fischer-Tropsch synthesis process. Reviews in Chemical Engineering, 1998. 14(2): p. 109-157
12. Pearl GtL. 2016; Available from: http://www.shell.com.qa/en_qa/projects-andsites/pearl-gtl.html..
13. Eilers, J., S.A. Posthuma, and S.T. Sie, The Shell Middle Distillate Synthesis Process (Smds). Catalysis Letters, 1991. 7(1-4): p. 253-269.
14. Oryx GtL. 2016; Available from: http://www.oryxgtl.com.qa/.
15. Ineratec Rethink GtL Process. 2016; Available from: http://www.ineratec.com/Technology/INERATEC-ReThink-GtL/.
16. T. U. Eindhoven and R. Magnificus, The Fischer-Tropsch synthesis: A mechanistic study using transient isotopic tracing, 2001.

17. Rao, V.U.S.; Stiegel, G.J.; Cinquegrane, G.J.; Srivastave, R.D., Iron-based catalysts for slurry-phase Fischer-Tropsch process: Technology review, Fuel Process. Technol. 1992, 30, 83–107.

18. Xu, L.; Bao, S.; R.J., O'Brien; Raje, A.; Davis, B.H., Don't rule out iron catalysts for Fischer-Tropsch synthesis, CHEMTECH 1998, 8, 47–53.

19. Raje, A.P.; Davis, B.H., Fischer-Tropsch synthesis: process considerations based on performance of iron-based catalysts, Fuel 1997, 76, 273–280.

20. Udovich, C.A., Ceramic membrane reactors for the conversion of natural gas to syngas, Stud. Surf. Sci. Catal. 1998, 119, 417–422.

21. Basini, L.; Piovesan, L., Reduction on synthesis gas costs by decrease of steam/carbon and oxygen/carbon ratios in the feedstock, Ind. Eng. Chem. Res. 1998, 37, 258–266.

22. F. T. Refining, F. Edition, and A. De Klerk, "Fischer – Tropsch Facilities at a Glance", 2011.

23. P.Biloen, J.N. Helle, W.M. H. Sachtler, J. Catal. 58 (1979) 95

24. R.B. Anderson, R.A. Friedel, H.H. Storch, J. Chem. Phys. 19 (1951) 313.

25. J. Couble, D. Bianchi, "Heats of adsorption of linearly adsorbed CO species on Co_{2+} and Co° sites of reduced Co/Al_2O_3 catalysts in relationship with the CO/H_2 reaction.", Applied Catalysis A: General 445– 446 (2012) 1– 13.

26. S. Derrouiche, D. Bianchi, "Heats of adsorption of the linear and bridged CO species on a Ni/Al_2O_3 catalyst by using the AEIR method", Applied Catalysis A: General 313 (2006) 208–217

27. T. Chafik, O. Dulaurent, J. L. Gass, D. Bianchi, "Heat of Adsorption of Carbon Monoxide on a $Pt/Rh/CeO_2/Al_2O_3$ Three-Way Catalyst Using in-Situ Infrared Spectroscopy at High Temperatures" , Journal of Catalysis 179, 503–514 (1998)

28. P. Van Helden, J.-A. Van den Berg, M. A. Petersen, W. J. Van Rensburg, I. M. Ciobica, J. Van de Loosdrecht, "Computational investigation of the kinetics and mechanism of the initial steps of the Fischer–Tropsch synthesis on cobalt", Faraday Discuss., 2017, 197, 117

29. E. Patanou, E. Z. Tveten, De Chen, A. Holmen, E. A. Blekkan, "Microcalorimetric studies of H_2 and CO on $Co/\gamma\text{-}Al_2O_3$ catalysts for Fischer–Tropsch synthesis", Catalysis Today 214 (2013) 19– 24

30. C.J. Weststrate, J. van de Loosdrecht, J.W. Niemantsverdriet, "Spectroscopic insights into cobalt-catalyzed Fischer-Tropsch synthesis: A review of the carbon monoxide interaction with single crystalline surfaces of cobalt", Journal of Catalysis 342 (2016) 1–16

31. Bell AT (1981) Catal Rev Sci Eng 23:203–232

32. Erdohelyi A, Solymosi F (1983) J Catal 84:446–460

33. Ponec V (1992) Catal Today 12:227–254

34. Dry ME (1996) Appl Catal A 138:319–344

35. Adesina AA (1996) Appl Catal A 138:345–367

36. Eliason SA, Bartholomew CH (1999) Appl Catal A 186:229–243

37. Davis BH (2009) Catal Today 141:25–33

38. G. P. van der Laan, A.C.M. Beenackers, "Intrinsic kinetics of the gas–solid Fischer–Tropsch and water gas shift reactions over a precipitated iron catalyst", Applied Catalysis A (2000)

39. Storsæter S, Chen D, Holmen A (2006), "Microkinetic modelling of the formation of C_1 and C_2 products in the Fischer–Tropsch synthesis over cobalt catalysts", Surf Sci 600:2051–2063

40. M. Ojeda, R. Nabar, A. U. Nilekar, A. Ishikawa, M. Mavrikakis, E. Iglesia," CO activation pathways and the mechanism of Fischer–Tropsch synthesis", Journal of Catalysis 272 (2010) 287–297 Journal of Catalysis 272 (2010) 287–297

41. Huo CF, Li YW, Wang J, Jiao H, "Formation of CH_x Species from CO Dissociation on Double-Stepped Co(0001): Exploring Fischer−Tropsch Mechanism", J. Phys. Chem. C, 2008, 112 (36), pp 14108–14116

42. Huo CF, Ren J, Li YW, Wang J, Jiao H, "CO dissociation on clean and hydrogen precovered Fe(111) surfaces", J Catal 249:174–184(2007)

43. C. G. Visconti, E. Tronconi, L. Lietti, P. Forzatti, S. Rossini, R. Zennaro, " Detailed Kinetics of the Fischer–Tropsch Synthesis on Cobalt Catalysts Based on H-Assisted CO Activation", Top Catal (2011) 54:786–800.

44. C. G. Visconti, E. Tronconi, L. Lietti, R. Zennaro, P. Forzatti, "Development of a complete kinetic model for the Fischer–Tropsch synthesis over Co/Al_2O_3 catalysts", Chemical Engineering Science 62 (2007) 5338 – 5343.

45. P. Azadi, G. Brownbridge, I. Kemp, S. Mosbach, J. S. Dennis, M. Kraft, "Microkinetic Modeling of the Fischer–Tropsch Synthesis over Cobalt Catalysts", ChemCatChem 2015, 7, 137 – 143

46. L. M. Aparicio, "Transient Isotopic Studies and Microkinetic Modeling of Methane Reforming over Nickel Catalysts", Journal of Catalysis (1997).

47. H.A.J. van Dijk, J.H.B.J. Hoebink, and J.C. Schouten," A mechanistic study of the Fischer–Tropsch synthesis using transient isotopic tracing. Part-1: Model identification and discrimination ", Topics in Catalysis Vol. 26, Nos. 1–4, December 2003

48. E. Rebmann, PhD Thesis "Mechanistic investigation on cobalt based Fischer-Tropsch catalysts", (2015).

49. G. Lozano-Blanco, K. Surla, J.W. Thybaut and G.B. Marin, "Extension of the Single-Event Methodology to Metal Catalysis: Application to Fischer-Tropsch Synthesis", Oil & Gas Science and Technology – Rev. IFP Energies nouvelles, Vol. 66 (2011), No. 3, pp. 423-435.

50. J. Yang, W. Ma, D. Chen, A. Holmen, and B. H. Davis, "Fischer-Tropsch synthesis: A review of the effect of CO conversion on methane selectivity," Appl. Catal. A Gen., vol. 470, pp. 250–260, 2014.

51. J. Yang, E. Z. Tveten, De Chen, A. Holmen, "Understanding the Effect of Cobalt Particle Size on Fischer-Tropsch Synthesis: Surface Species and Mechanistic Studies by SSITKA and Kinetic Isotope Effect", Langmuir 2010, 26(21), 16558–16567

52. M. Claeys, E van Steen, "On the effect of water during Fischer–Tropsch synthesis with a ruthenium catalyst", Catalysis Today 71 (2002) 419–427.

53. E. van Steen, H. Schulz, "Polymerisation kinetics of the Fischer–Tropsch CO hydrogenation using iron and cobalt based catalysts", Applied Catalysis A: General 186 (1999) 309–320.

54. S. Storsæter, Ø. Borg, E.A. Blekkan, A. Holmen, "Study of the effect of water on Fischer–Tropsch synthesis over supported cobalt catalysts", Journal of Catalysis 231 (2005) 405–419.

55. Li J., Zhan X., Jacobs G., Davis B. H., "Fischer−Tropsch synthesis: Effect of water on the deactivation of Pt promoted Co/Al_2O_3 catalysts.", Appl. Catal. 2002, 228, 203−212.

56. C. H. Bartholomew, R. J. Farrauto, "Fundamentals of industrial catalytic processes", 2nd Edition

57. R. Zennaro, M Tagliabue, C. H. Bartholomew, "Kinetics of Fischer–Tropsch synthesis on titania-supported cobalt", Catalysis Today 58 (2000) 309–319

58. F.H. Ribeiro, A.E.S. Von Wittenau, C.H. Bartholomew, G.A. Somorjai, Catal. Rev. Sci. Eng. 39 (1997) 49.

59. I. C. Yates, C. Satterfield, "Intrinsic Kinetics of the Fischer-Tropsch Synthesis on a Cobalt Catalyst", Energy & Fuels 1991, 5, 168-173

60. E. Iglesia, S. C. Reyes, R. J. Madon, S. L. Soled, "Selectivity Control and Catalyst Design in the Fischer-Tropsch Synthesis: Sites, Pellets, and Reactors", Advances in Catalysis 1993, Pages 221-302

61. E. Peluso, C. Galarraga, H. de Lasa, "Eggshell catalyst in Fischer-Tropsch synthesis intrinsic reaction kinetics", Chemical Engineering Science 56 (2001) 1239-1245

62. B. Sarup and B. W. Wojciechowski, "Studies of the Fischer-Tropsch Synthesis on a Cobalt Catalyst Kinetics of Carbon Monoxide Conversion to Methane and to Higher Hydrocarbons", (1989)

63. W. Ma, G. Jacobs, T. K. Das, C. M. Masuku, J. Kang, V. Ramana Rao Pendyala, B. H. Davis, "Fischer−Tropsch Synthesis: Kinetics and Water Effect on Methane Formation over $25\%Co/\gamma\text{-}Al_2O_3$ Catalyst", Ind. Eng. Chem. Res. 2014, 53, 2157−2166

64. M.A. Vannice, “The Catalytic Synthesis of Hydrocarbons from H_2/CO Mixtures over the Group VIII Metals”, Journal of Catalysis 37, 449-461 (1975)

65. Chen, H.; Adesina A. A., “Kinetic modeling of methanation reaction over a Co-Mo/SiO_2 catalyst.”, J. Chem. Technol. Biotechnol. 1994, 60, 103−113.

66. M. C. Valero and P. Raybaud, “Stability of Carbon on Cobalt Surfaces in Fischer−Tropsch Reaction Conditions: A DFT Study”, J. Phys. Chem. (2014)

67. M. Zhuo, K. F. Tan, A. Borgna, and M. Saeys, “Density Functional Theory Study of the CO Insertion Mechanism for Fischer - Tropsch Synthesis over Co Catalysts,” pp. 8357–8365, 2009.

68. O. R. Inderwildi, S. J. Jenkins, and D. A. King, “Fischer-Tropsch mechanism revisited: Alternative pathways for the production of higher hydrocarbons from synthesis gas,” J. Phys. Chem. C, vol. 112, no. 5, pp. 1305–1307, 2008.

69. C. J. Weststrate, H. J. Gericke, M. W. G. M. Verhoeven, I. M. Ciobîcă, A. M. Saib, and J. W. (Hans) Niemantsverdriet, “Ethanol Decomposition on Co(0001): C−O Bond Scission on a Close-Packed Cobalt Surface,” J. Phys. Chem. Lett., vol. 1, no. 12, pp. 1767–1770, Jun. 2010.

70. J.Cheng, Xue-Qing Gong, P.Hu, C.M. Lok, P. Ellis, S. French, “A quantitative determination of reaction mechanisms from density functional theory calculations: Fischer–Tropsch synthesis on flat and stepped cobalt surfaces”, Journal of Catalysis 254 (2008) 285–295

71. D.J. Klinke , D.J. Dooling, L.J. Broadbelt, “A theoretical study of methylidyne chemisorption on Ni(111) and Co(0001) surfaces”, Surface Science (1999)

72. E. Shustorovich, H. Sellers, “The UBI-QEP method: a practical theoretical approach to understanding chemistry on transition metal surfaces”,(1998)

73. E. Shustorovich, A. T. Bell, “Analysis of CO Hydrogenation Pathways Using the Bond-Order-Conservation Method”, Journal of Catalysis (1988)

74. S. Storsæter, De Chen, A. Holmen, “Microkinetic modelling of the formation of C_1 and C_2 products in the Fischer–Tropsch synthesis over cobalt catalysts”, Surface Science 600 (2006) 2051–2063.

75. J. Van Belleghem, C. Ledesma, J. Yang, K. Toch, D. Chen, J. W. Thybaut, G. Marin, “A Single-Event MicroKinetic model for the cobalt catalyzed Fischer-Tropsch Synthesis”, Applied Catalysis A: General 524 (2016) 149–162

76. L. Shannon and J. G. Goodwin, “Characterization of Catalytic Surfaces by isotopic-transient kinetics during steady-state reaction,” Chem. Rev., pp. 677–695, 1995.

77. J. Happel, “Transient tracing - Letter to the Editors,” Chem. Eng. Sci., vol. 33, pp. 1567–1568, 1978.

78. J. Happel, H.Y. Cheh, M. Otarod, S. Ozawa, A.J. Severdia, T. Yoshida, V. Fthenakis, "Multiple isotope tracing of methanation over nickel catalyst: II. Deuteromethanes tracing", Journal of Catalysis (1982)

79. J. Happel, I. Suzuki, P. Kokayeff, V. Fthenakis, "Multiple isotope tracing of methanation over nickel catalyst", Journal of Catalysis (1980)

80. P. Biloen, "Transient Kinetic Methods," J. Mol. cata, vol. 21, pp. 17–24, 1983.

81. C. O. Bennett, "Understanding Heterogeneous Catalysis through the Transient Method," in In Catalysis Under Transient Conditions, no. 14, 1982, p. 1.

82. E. Walter, Y. Lecourtier, J. Happel, and J. Kao, "ldentifiability and Distinguishability of Fundamental Parameters in Catalytic Methanation," vol. 32, no. 8, 1986

83. Y. Soong, K. Krishna, and P. Biloen, "Catalyst Aging Studied with Isotopic Transients : Raney Nickel Methanation over," J. Catal., vol. 343, pp. 330–343, 1986

84. L. G. Pinaeva, E. M. Sadovskaya, a. P. Suknev, V. B. Goncharov, and B. S. Bal'zhinimaev, "Mass Spectrometry in the SSITKA Studies," Mass Spectrom. Handb., no. July 2015, pp. 1229–1256, 2012.

85. B. S. Bal'zhinimaev, E. M. Sadovskaya, and a. P. Suknev, "Transient isotopic kinetics study to investigate reaction mechanisms," Chem. Eng. J., vol. 154, no. 1–3, pp. 2–8, 2009.

86. H. A. J. van Dijk, "The Fischer-Tropsch synthesis: A mechanistic study using transient isotopic tracing," 2001

87. H. A. J. Van Dijk, J. H. B. J. Hoebink, and J. C. Schouten, "A mechanistic study of the Fischer – Tropsch synthesis using transient isotopic tracing. Part 2: Model quantification," Top. Catal., vol. 26, no. 1–4, pp. 163–171, 2003.

88. A. Bundhoo, J. Schweicher, A. Frennet, and N. Kruse, "Chemical Transient Kinetics Applied to CO Hydrogenation over a Pure Nickel Catalyst", J. Phys. Chem. C 2009, 113, 10731–10739

89. W. Schiesser , The Numerical Method of Lines,1st Edition

90. Hindmarsh, A. C. ODEPACK, A systematized collection of ODE solvers; Elsevier, 1983

91. Marquardt DW. An algorithm for least squares estimation of non-linear parameters. J. Soc. Ind. Appl. Math. 1963; 11:431-441.

92. E. N. Fuller, P. D. Schettler, and J. C. Giddings, Ind. Eng. Chem. 58(5), 19 (1966)

93. R.C. Reid, J.M. Prausnitz, B. E. Polling., "The properties of gases & liquids"

94. Marquardt DW. An algorithm for least squares estimation of non-linear parameters. J. Soc. Ind. Appl. Math. 1963; 11:431-441.

95. Froment GF, Bischoff K., Chemical Reactor Analysis and Design, 2nd ed., John Wiley and Sons, New York, 1990.

96. Levenberg K. A method for the solution of certain non-linear problems in least squares. Q. Appl. Math. 1944; 11:164-168.

97. Froment GF, Hosten LH. Catalytic Kinetics: Modelling. Catalysis Science and Technology (Anderson JR, Boudart M. Eds.) Springer Verlag 1981 Berlin

98. E. Rebmann, P. Fongarland, V. Lecocq, F. Diehl, Y. Schuurman," Kinetic modeling of transient Fischer–Tropsch experiments over Co/Al_2O_3 catalysts with different microstructures", Catalysis Today 275 (2016) 20–26

99. A. Dinse, M. Aigner, M. Ulbrich, G. R. Johnson, and A. T. Bell, "Effects of Mn promotion on the activity and selectivity of Co/SiO_2 for Fischer–Tropsch Synthesis," J. Catal., vol. 288, pp. 104–114, 2012

100. L. Braconnier, E. Landrivon, I. Clémenc¸ on, C. Legens, F. Diehl, Y. Schuurman, "How does activation affect the cobalt crystallographic structure? An in situXRD and magnetic study", Catal. Today (2013).

101. G. Ertl, H. Knozinger, F. Schuth and J. Weitkam--Handbook of Heterogeneous Catalysis, Second Edition, WILEY-VCH

102. J. Couble and D. Bianchi, "Experimental Microkinetic Approach of the Surface Reconstruction of Cobalt Particles in Relationship with the CO/H_2 Reaction on a Reduced 10% Co/Al_2O_3 Catalyst," J. Phys. Chem. C, vol. 117, pp. 14544–14557, 2013.

103. P. Kaushal, R. Tyagi, Steam assisted biomass gasification, an overview, Can. J.Chem. Eng. 90 (4) (2012) 1043–1058

104. C. Mirodatos, H. Praliaud, M. Primet, Deactivation of Ni-based catalysts during CO methanation and disproportionation, J. Catal. 107 (1987) 275–287.

105. M. Agnelli, M. Kolb, C. Mirodatos, CO hydrogenation on a nickel catalyst I. Kinetics and modeling of a low temperature sintering process, J. Catal. 148 (1994) 9–21.

106. M. A. Vannice, Journal of Catalysis 44, 152-162 (1976)

107. V.M.Vlasenko, G.E.Yuzefovich, "Mechanism of the Catalytic Hydrogenation of Oxides of Carbon to Methane", Russian Chemical Reviews, 38 (9), 1969

108. P. Schoubye, "Methanation of CO on Some Ni Catalysts", Journal of Catalysis 14, 238-246 (1969)

109. P. Schoubye, J. Catal. 18, 118 (1970).

110. T. Van Herwijnen, H. Van Doesburg, W. A. De Jong, "Kinetics of the Methanation of CO and CO_2 on a Nickel Catalyst", Journal of Catalysis 28, 391-402 (1973)

111. J. Sehested, S. Dahl, J. Jacobsen, J. R. Rostrup-Nielsen, "Methanation of CO over Nickel: Mechanism and Kinetics at High H_2/CO Ratios", J. Phys. Chem. B 2005, 109, 2432-2438

112. B. Legras, V. V. Ordomsky, C. Dujardin, M. Virginie, A. Y. Khodakov, "Impact and Detailed Action of Sulfur in Syngas on Methane Synthesis on Ni/γ-Al_2O_3 Catalyst", ACS Catal. 2014, 4, 2785−2791.

113. B.S. Bal'zhinimaev, E.M. Sadovskaya, A.P. Suknev, "Transient isotopic kinetics study to investigate reaction mechanisms", Chemical Engineering Journal (2009)

114. N.S.Govender, M.H.J.M.de Croon, J.C.Schouten, "Reactivity of surface carbonaceous intermediates on an iron-based Fischer–Tropsch catalyst", Applied Catalysis A: General 373 (2010) 81–8

115. T. Mori, H. Masuda, H. Imai, "Kinetics, Isotope Effects, and Mechanism for the Hydrogenation of Carbon Monoxide on Supported Nickel Catalysts", J. Php. Chem. 1982, 86, 2753-2760.

116. M. Ojeda, A. Li, R. Nabar, A. U. Nilekar, M. Mavrikakis, E. Iglesia, "Kinetically Relevant Steps and H_2/D_2 Isotope Effects in Fischer-Tropsch Synthesis on Fe and Co Catalysts", J. Phys. Chem. C 2010, 114, 19761–19770.

117. T. Osawa, Y. Hamano, S. Saga, O. Takayasu, "Hydrogen–deuterium exchange of methane on nickel surface prepared by the reduction of nickel oxide", Journal of Molecular Catalysis A: Chemical 298 (2009) 111–114

118. C. Marquez-Alvarez, G.A. Martin, and C. Mirodatos, "Mechanistic insights in the CO hydrogenation reaction over Ni/SiO_2", 1998

119. H. A. J. van Dijk, PhD. Thesis "The Fischer-Tropsch synthesis: A mechanistic study using transient isotopic tracing", Eindhoven: Technische Universiteit Eindhoven, 2001

120. A. Carvalho, V. V. Ordomsky, Y. Luo, M. Marinova, A. R. Muniz, N. Romeu Marcilio, A. Y. Khodakov, "Elucidation of deactivation phenomena in cobalt catalyst for Fischer-Tropsch synthesis using SSITKA", Journal of Catalysis 344 (2016) 669–6

121. J. P. den Breejen, P. B. Radstake, G. L. Bezemer, J. H. Bitter, V. Frøseth, A. Holmen, K. P. de Jong, "On the Origin of the Cobalt Particle Size Effects in Fischer-Tropsch Catalysis", J. Am. Chem. SOC. 2009, 131, 7197–7203

122. Z. Yan, Z. Wang, D. B. Bukur, D. W. Goodman, "Fischer–Tropsch synthesis on a model Co/SiO_2 catalyst", Journal of Catalysis 268 (2009) 196–200

123. F.H. Ribeiro, A.E.S. Von Wittenau, C.H. Bartholomew, G.A. Somorjai, Catal. Rev. Sci. Eng. 39 (1997) 49.

124. H.Atashi, F.Siami, A.A.Mirzaei, M.Sarkaria, "Kinetic study of Fischer–Tropsch process on titania-supported cobalt–manganese catalyst", Journal of Industrial and Engineering Chemistry 16 (2010) 952–961

125. M. Mansouri, H, Atashi, A. A. Mirzaei, R. Jangi, “Kinetics of the Fischer-Tropsch synthesis on silica-supported cobalt-cerium catalyst”, International Journal of Industrial Chemistry 2013

126. K. R. Krishna, A. T. Bell, “The role of C_2 intermediates in Fischer-Tropsch synthesis over ruthenium”, Catalysis Letters 14 (1992) 305-313

127. J. Gaube, H.-F. Klein, “Studies on the reaction mechanism of the Fischer–Tropsch synthesis on iron and cobalt”, Journal of Molecular Catalysis A: Chemical 283 (2008) 60–68

128. J. Patzlaff, Y. Liu, C. Graffmann, J. Gaube, ” Interpretation and kinetic modeling of product distributions of cobalt catalyzed Fischer–Tropsch synthesis”, Catalysis Today 71 (2002) 381–394

129. L. T. Percy, R. I. Walter, “An NMR Study of the Mode of Incorporation of Ethene into Propene in the Fischer-Tropsch Reaction over Cobalt”, Journal of Catalysis 121, 228--235 (1990)

130. M. L. Turner, N. Marsih, B. E. Mann, R. Quyoum, H. C. Long, P. M. Maitlis, “Investigations by ^{13}C NMR Spectroscopy of Ethene-Initiated Catalytic CO Hydrogenation”, J. Am. Chem. Soc. 2002, 124, 10456-10472

131. I Alstrup, “ On the Kinetics of CO Methanation on Nickel Surface”, Journal of Catalysis 151, 216-225, 1995

132. E. Walter, L. Pronzato, Y. Soong, M. Otarod, J. Happel, “Modeling Transient Tracing in Plug-Flow Reactors: A Case Study”, Ind. Eng. Chem. Res. 1996,34, 483-487

133. F. Abild-Pedersen, J. Greeley, F. Studt, J. Rossmeisl, T. R. Munter, P.G. Moses, E. Sku´lason, T. Bligaard, and J. K. Nørskov, “Scaling Properties of Adsorption Energies for Hydrogen-Containing Molecules on Transition-Metal Surfaces”, 2007 The American Physical Society

134. NIST Chemistry WebBook - NIST Standard Reference Database Number 69. Available from: http://webbook.nist.gov/chemistry.

135. A. Stuck , C.E. Wartnaby, Y.Y. Yeo, J.T. Stuckless, N. Al-Sarraf, D.A. King, “An improved single crystal adsorption calorimeter”, Surf. Sci. 349 (1996) 229-240

136. M. A. De Angelis, A. M. Glines, A. B. Anton, “Precursor and overlayer structural effects in the interaction of CO with Ni(110) “,The Journal of Chemical Physics 96, 8582 (1992)

137. J. T. Stuckless, N. Al-Sarraf, C. Wartnaby, D. A. King, “Calorimetric heats of adsorption for CO on nickel single crystal surfaces”, The Journal of Chemical Physics 99, 2202 (1993)

138. C. H. Bartholomew, “Hydrogen adsorption on supported cobalt, iron, and nickel”, Catalysis Letters 7 (1990) 27-52

139. Q. Ge, M. Neurock, "Adsorption and Activation of CO over Flat and Stepped Co Surfaces: A First Principles Analysis", J. Phys. Chem. B 2006, 110, 15368-15380

140. P. van Helden, J-A. van der Berg, I. M. Ciobica, "Hydrogen assisted CO dissociation on the Co(211) stepped surface", Catal. Sci. technol., 2012, 2, 491-494.

141. C.J. Weststrate, P. van Helden, J. van de Loosdrecht, J.W. Niemantsverdriet, "Elementary steps in Fischer–Tropsch synthesis: CO bond scission, CO oxidation and surface carbiding on Co(0001)", Surface Science 648 (2016) 60–66

142. D.J. Klinke, D.J. Dooling, L.J. Broadbelt, "A theoretical study of methylidyne chemisorption on Ni(111) and Co(0001) surfaces", Surface Science 425 (1999) 334–342.

143. X. Gong, R. Raval, P. Hu, "CHx hydrogenation on Co(0001): A density functional theory study", The Journal of Chemical Physics 122, 024711 (2005)

144. N. Balakrishnan, B. Joseph, V. R. Bhethanabotla, "Effect of platinum promoters on the removal of O from the surface of cobalt catalysts: A DFT study", Surface Science 606 (2012) 634–643

145. M. Agnelli, H. M. Swaan, C. Marquez-Alvarez, G. A. Martin, and C. Mirodatos, "CO Hydrogenation on a Nickel Catalyst. II. A Mechanistic Study by Transient Kinetics and Infrared Spectroscopy", Journal of Catalysis (1998)

146. A.T. Bell, E. Shustorovich, "A comment on the Analysis of CO Hydrogenation Using the BOC-MP Approach", Journal of Catalysis (1990)

147. R. Van Hardeveld and F. Hartog, "The statistics of surface atoms and surface sites on metal crystals", Surface Science 15 (1969) 189-230

148. Campbell, C. T. ,"Finding the Rate-Determining Step in a Mechanism", Journal of Catalysis 204, 520–524 (2001).

149. C. Stegelmann, A. Andreasen, C. T. Campbell, "Degree of Rate Control: How Much the Energies of Intermediates and Transition States Control Rates", J. Am. Chem. Soc. 9 VOL. 131, NO. 23, 2009.

150. R.P. Underwood, C.O. Bennett, "The CO/H_2 reaction over Nickel-Alumina studied by the Transient Method", Journal of Catalysis 86, 245-253 (1984)

151. F. Labohm, O.L.J. Gijzeman, J.W. Geus, "The interaction of oxygen with Ni(111) and the reduction of the surface oxide by carbon monoxide and by hydrogen", Surface Science 135 (1983) 409-427

152. M.P. Andersson, F. Abild-Pedersen, I. N. Remediakis, T. Bligaard, G.Jones, J. Engbæk, O. Lytken, S.Horch, J.H.Nielsen, J. Sehested, J.R. Rostrup-Nielsen, J.K.Nørskov, I. Chorkendorff, "Structure sensitivity of the methanation reaction: H_2-induced CO dissociation on nickel surfaces", Journal of Catalysis 255 (2008) 6–19

Appendix 1

H_2 adsorption

Figure A1 shows a dynamic hydrogen adsorption experiment at 200°C. As expected, the nitrogen response appears first followed by the hydrogen response delayed by approximately 8 seconds. As the nitrogen does not adsorb on the catalyst and the partial pressure of nitrogen is the same as the partial pressure of hydrogen, the difference between the nitrogen and hydrogen response corresponds to the amount of adsorbed hydrogen as a function of time, as shown in Figure 38 for the data at three temperatures. Integration of this curve gives the total amount of hydrogen adsorbed. Table 16 list the amounts of hydrogen adsorbed, as atomic hydrogen, on the catalyst at three different temperatures.

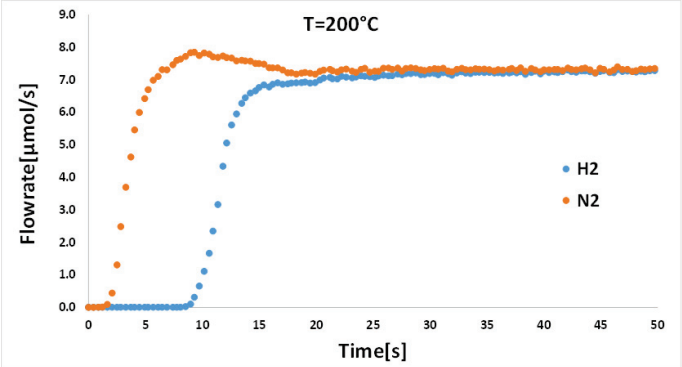

Figure A1: H_2 (blue) adsorption step response experiments at 200°C.The nitrogen step response is given by the orange curve

Assuming a Langmuir adsorption isotherm and dissociative hydrogen adsorption on nickel, the data in Table 16 were fitted:

$$H_2 + 2 * \rightleftarrows 2H^*$$

So at steady state:

$$k_{ads}\, P_{H_2}(1-\theta_H)^2 = k_{des}{\theta_H}^2$$

$$\frac{{\theta_H}^2}{(1-\theta_H)^2} = \frac{k_{ads}}{k_{des}}\, P_{H_2}$$

We can express the surface hydrogen coverage θ_H as:

$$\theta_H = \frac{\sqrt{K_{H_2} P_{H_2}}}{1 + \sqrt{K_{H_2} P_{H_2}}}$$

Where $K_{H_2} = \frac{k_{ads}}{k_{des}}$, the θ_H is the ratio between the amount of adsorbed hydrogen, $N_{H_{ads}}$, and the total number of surface site, N_S :

$$N_{H_{ads}} = \frac{N_S \sqrt{K_{H_2} P_{H_2}}}{1 + \sqrt{K_{H_2} P_{H_2}}}$$

The K_{H_2} could be expressed as function of hydrogen heat of adsorption:

$$K_{H_2} = K^o_{H_2}\, exp^{\left(\frac{\Delta H_{ads}}{RT}\right)}$$

The data fit, as shown in Figure 38, was obtained with the following equilibrium adsorption constant:

$$K_{H_2} = exp\left(\frac{-114.9}{R}\right) exp\left(\frac{73934}{RT}\right) \qquad atm^{-0.5}$$

Assuming a hydrogen atom/nickel surface atom stoichiometry of 1:1 the number of nickel adsorption sites was calculated as N_s=0.68 mol kg_{cat}^{-1}.

The values of N_S, K_{eq}, ΔH_{ads} were used for the regression analysis of the step-response and SSITKA data.

Appendix 2

Mass and heat transfer limitations

For an experimental microkinetic approach is important that the intrinsic kinetics are measured, i.e. reaction rates free from heat and mass transfer limitations. In order to determine under which conditions intrinsic rates can be measured during SSITKA and step transient experiments, a sensitivity analysis with respect to mass and heat transfer criteria was carried out. These criteria evaluate a ±5% deviation of the intrinsic rate, which is still tolerated with respect to the experimental error (section 3.2).

Typical reaction conditions for SSITKA fixed-bed experiments have been chosen as shown in Table A1.

Table A1: Operating conditions and reactor and catalyst properties

Description	Value	Description	Value
Temperature	498 K	Catalyst conductivity	0.5 W/m/K
Pressure	1.2 bar	Apparent activation energy	78 kJ/mol
Gas Composition	60% H_2, 15% CO, 25% Ar	Reaction enthalpy	206 kJ/mol
Volumetric flowrate	100 Nml/min	Internal tube diameter	2-14 mm
Catalyst amount	0.2 g	Effective CO diffusivity	1.8e-7 m^2/s
Dilution degree (with SiC)	0.3	Heat capacity of gas mixture	1420 J/kg/K
Bed porosity	0.5	gas viscosity	2.3e-5 kg/m/s
Catalyst bulk density	800 kg/m^3	Bed effective thermal conductivity	0.6 W/m/K
Sh	6	Nu	2.5

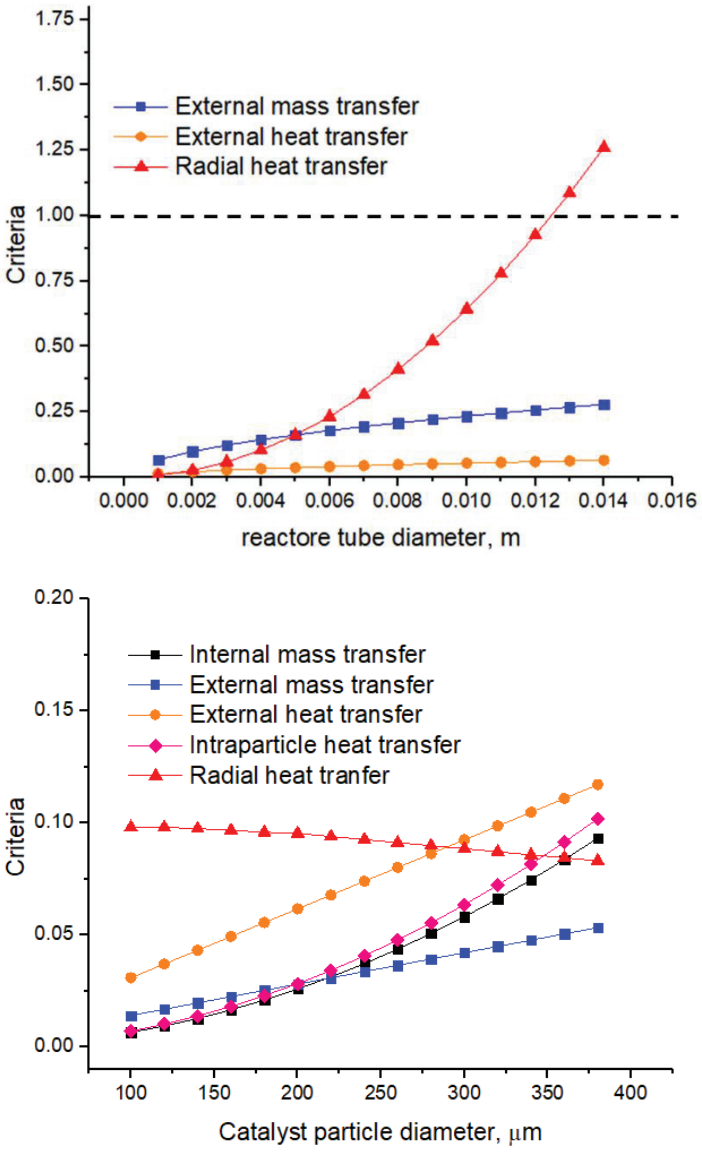

Figure A2: Variation of the different criteria for heat and mass transport as a function of the reactor internal diameter (left) and the catalyst particle size (right). The dotted lines indicate the limit of the criteria. No limitations are expected for the criteria below these lines.

In Figure A2 these criteria are plotted as a function of the tube diameter and the catalysts particle diameter. In these calculations 0.2 g of catalyst diluted with 0.4 gram of SiC was used, leading to a CO conversion of

0.05 at 225°C. A value of a criterion below 1 indicates that the rate will deviate less than 5%.

For the selected reactor tube diameter of 7 mm and catalyst particle size between 100-200 μm, all the criteria to avoid mass and heat transfer limitations are satisfied.

Appendix 3

Unity Bond Idex – Quadratic Exponential Potential (UBI-QEP)

The method relates the chemisorption enthalpy of a gas phase species to a limited set of parameters, i.e., gas phase molecular bond energies, D_{AB}, and atomic chemisorption enthalpies, Q_A. The first set of parameters can be readily obtained from open databases [134] while the second set is estimates from specific formula (see Appendix 3) that take in to count the strength of the molecule-metal bond[49,72,74]. Moreover in this formula are required the atomic chemisorption enthalpy of reactants that in our case were H, C and O.

The UBI-QEP (Unity Bond Idex – Quadratic Exponential Potential) method is a phenomenological method that relates the chemisorption enthalpy of a gas phase species to a limited set of parameters.

These parameters are the gas phase molecular bond energies, D_{AB}, and atomic chemisorption enthalpies, Q_A.

The UBI-QEP method can also be used to calculate activation energies for an initial estimates.

Estimation of activation energies by means of the UBI-QEP method is based on specific formulas that are related to the molecule coordination. In the UBI-QEP method the atomic chemisorption enthalpy on an n fold coordination site is related to the atomic chemisorption enthalpy on the top site as follows:

$$Q_{0A} = \frac{Q_A}{(2 - \frac{1}{n})}$$

Where

Q_A is the atomic chemisorption enthalpy on a n fold coordination site in kJ mol^{-1}

Q_{0A} is the atomic chemisorption enthalpy on the top site in kJ mol^{-1} and n the coordination number.

With the UBI-QEP method is also possible to calculate the chemisorption enthalpies of molecules taking in to count the strength of molecule-metal bonding.

The UBI-QEP equation are summarized in Table A2 :

Table A2: UBI-QEP equations for calculating the heat of chemisorption

Eq. #	Equation	Heat of adsorption for
1	$Q_{0A} = \frac{Q_A}{(2 - \frac{1}{n})}$	Metal-atom bonding
2	$Q_{AB,n} = \frac{Q_{0A}^2}{(\frac{Q_{0A}}{n'} + D_{AB})}$	A weak bounded molecule AB, with on-top coordination. n' is the number of atoms involved in the bonding
3	$Q_{AB} = \frac{Q_A^2}{(Q_A + D_{AB})}$	A strong bounded molecule, with the A end down
4	$Q_{AB} = \frac{1}{2}\left[\frac{Q_{0A}^2}{(\frac{Q_{0A}}{n'} + D_{AB})} + \frac{Q_A^2}{(Q_A + D_{AB})}\right]$	Medium bounded molecule, with A end down
5	$Q_{AB} = \frac{1}{2}\left[\frac{a\ b\ (a+b)+D_{AB}\ (a-b)^2}{a\ b\ +D_{AB}(a+b)}\right]$ $a = Q_{0A}^2 \frac{(Q_{0A}+2\ Q_{0B})}{(Q_{0A}+\ Q_{0B})^2}$ $\quad b = Q_{0B}^2 \frac{(Q_{0B}+2\ Q_{0A})}{(Q_{0A}+\ Q_{0B})^2}$	Medium bounded molecule, where AB is coordinated via both A and B
6	$Q_{AB} = \frac{\frac{9}{2} Q_{0A}^2}{3\ Q_{0A} + 8\ D_{AB}}$	Symmetric species (H_2, CO_2)

By means of the equation in Table A2 is possible to calculate the activation energies with the equation reported in Table A3.

Table A3: Equation for calculation of activation energies from the heat of adsorption

Eq. #	Equation	Description
1	$\Delta E^*_{AB,g} = \frac{1}{2}\left(D_{AB} + \frac{Q_A Q_B}{Q_A + Q_B} - Q_{AB} - Q_A - Q_B\right)$	Activation energy for the dissociation of gas-phase species. $AB_g \rightarrow A^* + B^*$
2	$\Delta E^*_{AB,S} = \Delta E^*_{AB,g} + Q_{AB}$	Activation energy for the dissociation of an adsorbed species. $AB^* \rightarrow A^* + B^*$

Moreover is possible to calculate the enthalpy of surface reaction for a generic reaction $AB^* \rightarrow A^* + B^*$ from the UBI-QEP values of heat of adsorption:

$$\Delta H_{r,AB} = D_{AB} + Q_{AB} - Q_A - Q_B$$

Publications

1. *"CO hydrogenation on cobalt-based catalysts: tin poisoning unravels hollow-CO as a main surface intermediate"*, F.C. Meunier, A. Paredes-Nunez, **D. Lorito,** L. Burel, Y. Schuurman, Angewandte Chemie(2017)

2. "*Understanding deactivation processes during bio-syngas methanation: DRIFTS and SSITKA experiments and kinetic modeling over Ni/Al_2O_3 catalysts",* **D. Lorito**, H. Li, A. Travert, F. Maugé, F. C. Meunier, Y. Schuurman, C. Mirodatos, Catalysis Today(2017)

3. *"Reconstruction of ceria-supported Pt-Co particles under H_2 and CO at 220°C",* **D. Lorito**, C. Ruocco, V. Palma, A. Giroir-Fendler, F.C. Meunier, Applied Catalysis B: Environmental(2016)

4. *"Determination of formate decomposition rates and relation to product formation during CO hydrogenation over supported cobalt.",* **D. Lorito**, A. Paredes-Nunez, C. Mirodatos, Y. Schuurman, F. C. Meunier, Catalysis Today(2015)

5. *"Nature and reactivity of the surface species observed over a supported cobalt catalyst under CO /H_2 mixtures "*, A. Paredes-Nunez, **D. Lorito**, N. Guilhaume, C. Mirodatos, Y. Schuurman, F.C. Meunier, Catalysis Today(2015)

6. *"Origins of the poisoning effect of chlorine on the CO hydrogenation activity of alumina-supported cobalt monitored by operando FT-Irspectroscopy "*, A. Paredes-Nunez, **D. Lorito**, Y. Schuurman, N. Guilhaume, F.C. Meunier, Journal of Catalysis(2015)

Conferences

1. EUROPACAT17, Florence (Italy)2017, Oral Communication: "Understanding deactivation processes during bio-syngas methanation: DRIFTS and SSITKA experiments and modeling over Ni/Al_2O_3catalysts" , **D. Lorito**, H.Li, A.Travert, F.Maugé, C.Mirodatos, Y.Schuurman

2. EUROPACAT17, Florence (Italy)2017, Oral Communication: "Transient kinetics for methane pathways identification over Fischer-Tropsch catalysts", **D. Lorito**, Y. Schuurman, P. Fongarland, D. Decottignies

3. NAM25, Denver (Colorado,USA) 4-9 June 2017, Oral Communication: "Transient kinetics for methane pathways identification over Fischer-Tropsch catalysts", **D. Lorito**, Y. Schuurman, P. Fongarland, D. Decottignies

4. NGCS11, Tromsø (Norway) 6-9 June 2016, Oral Communication: "Understanding aging processes during bio-syngas methanation for synthetic natural gas production", **D. Lorito**, H. Li, A.Travert, F. Maugé, F.C. Meunier, Y. Schuurman, C. Mirodatos

5. NGCS11, Tromsø (Norway) 6-9 June 2016, Poster Prize, "Determination of the most active sites for CO hydrogenation over supported cobalt by selective poisoning with tin", A. Paredes-Nunez, **D. Lorito**, L. Burel, N. Guilhaume, Y. Schuurman, F. C. Meunier

6. FCCAT1, Frejus (France) May 2016, Poster Prize, "Determination of formate decomposition rates and relation to product formation during CO hydrogenation over supported cobalt", **D. Lorito**, A. Paredes-Nunez,C. Mirodatos, Y. Schuurman and F.C. Meunier